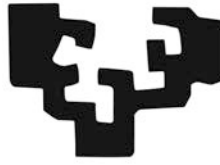


eman ta zabal zazu



Universidad
del País Vasco

Euskal Herriko
Unibertsitatea

DEPARTAMENTO DE FISICA DE MATERIALES - MATERIALEN FISIKA SAILA

PhD Thesis

Vapor Phase Infiltration (VPI) and Doping of Conducting Polymers

By Weike Wang

Academic Dissertation

Supervisor: Mato Knez

2017, September

This PhD thesis has been performed at:



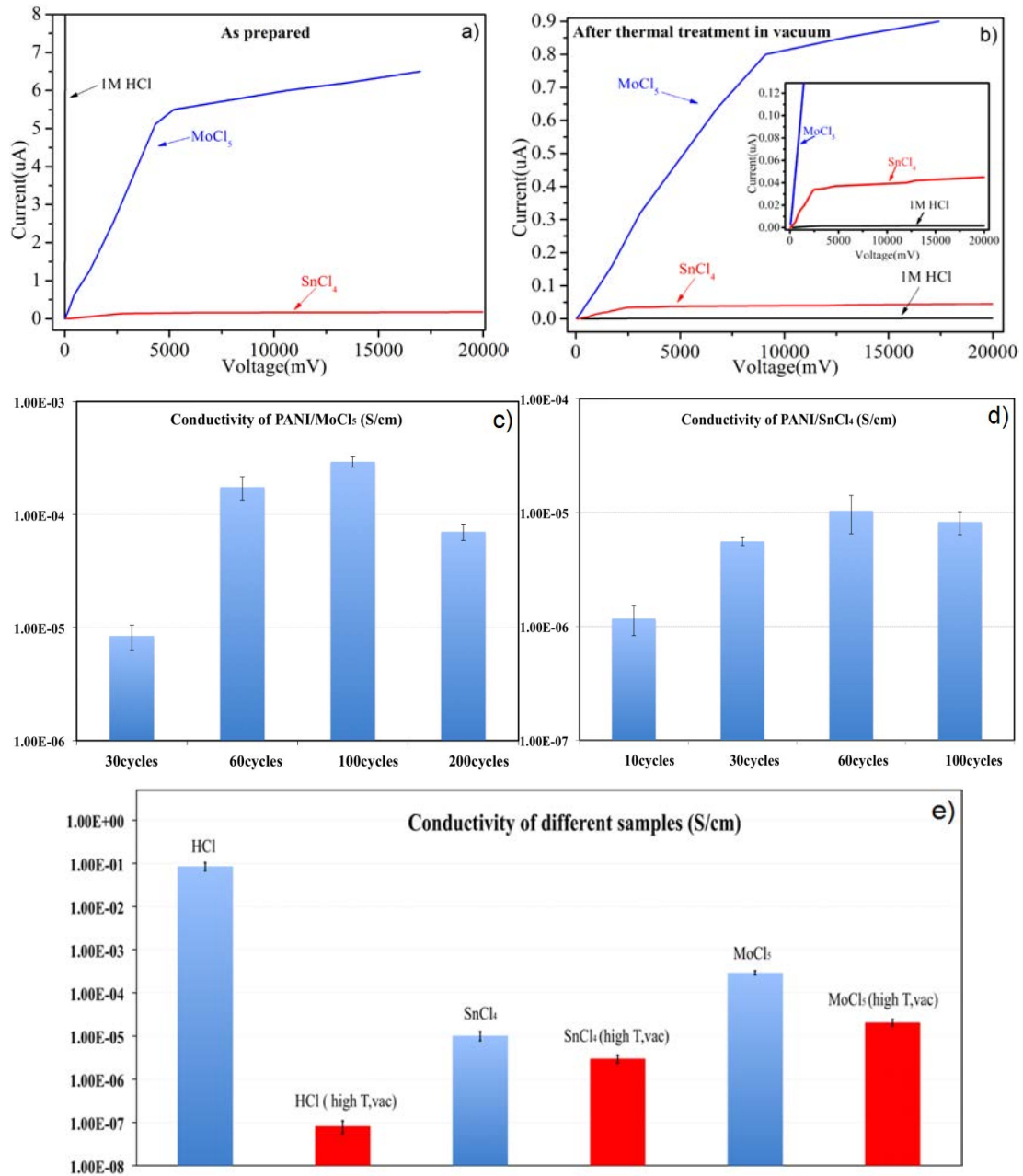
CIC nanoGUNE
Nanomaterials group
Donostia-San Sebastián, SPAIN

Resumen

En los últimos años, los polímeros conductores han sido ampliamente investigados debido a su enorme importancia como parte integral de una amplia gama de dispositivos eléctricos. Por ejemplo, se han reportado estudios sobre el aumento de la movilidad de los portadores de carga en transistores de efecto de campo (siglas en inglés, FET) obtenido mediante el llenado de huecos, la mejora de la inyección de carga en diodos emisores de luz (LED) y, más recientemente, el aumento de la eficiencia de conversión de potencia en células fotovoltaicas orgánicas. Durante la fabricación de los dispositivos eléctricos, para la mejora de su eficiencia y tiempo de vida, es esencial la realización de películas poliméricas finas, estables y transparentes, con un dopaje controlado. Hoy en día, las estrategias típicas de dopaje se basan en reacciones redox de transferencia de carga (procesos químicos o electroquímicos de n-/p-dopaje) y reacciones ácido-base no-redox (prolongación de polianilina), que resultan en conductividad eléctrica permanente. Sin embargo, estos procesos de dopaje se llevan a cabo en estado líquido (con disolventes o en soluciones), lo que puede introducir varias especies químicas, tales como disolventes o subproductos derivados de reacciones químicas en la matriz polimérica. En consecuencia, la conductividad y estabilidad del polímero pueden verse negativamente afectadas. Además, los procesos de dopaje en estado líquido también pueden influenciar la morfología, estructura y pureza del polímero conductor, los cuales son muy importantes en multitud de aplicaciones.

En esta tesis, se presenta una ruta alternativa que evita los efectos negativos y propicia un mayor control del proceso de dopaje. La infiltración en fase vapor (Vapor Phase Infiltration, VPI), un proceso de arriba-abajo (top-down process) basado en el vacío y derivado de la deposición de capa atómica (Atomic Layer Deposition, ALD) es usada para la infiltración y el dopaje de polímeros conductores.

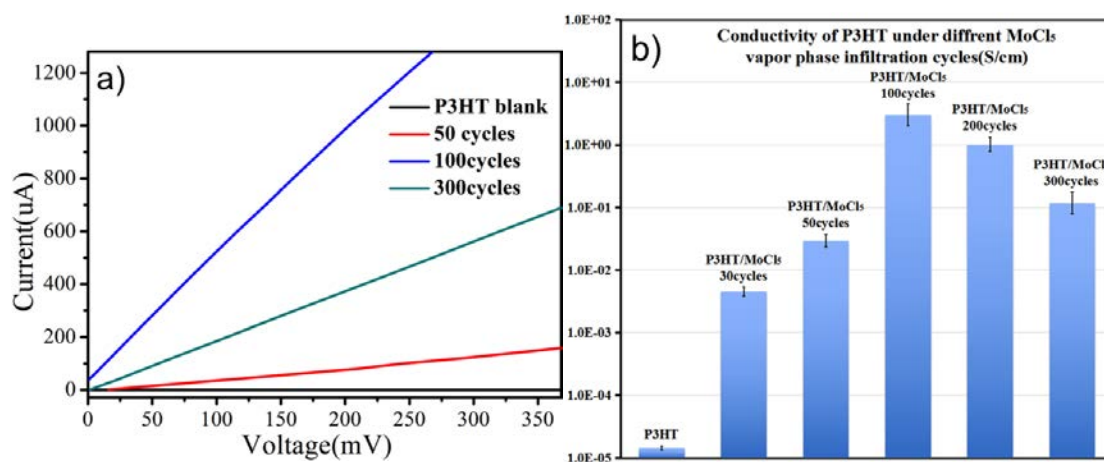
En la primera parte de esta tesis, se presenta el dopaje de polianilina (PANI) mediante la infiltración en fase vapor de un solo precursor (VPI). Como dopantes, se han utilizado los ácidos de Lewis SnCl_4 y MoCl_5 vaporizados a $150\text{ }^\circ\text{C}$. Las conductividades se han extraído de las medidas de corriente-voltaje a cuatro puntas. De las curvas I-V a temperatura ambiente, se ha visto que la conductividad del PANI infiltrado varía en función del número de ciclos de infiltración. Después de 100 ciclos, el PANI infiltrado con MoCl_5 muestra la mayor conductividad, $2.93 \times 10^{-4}\text{ S/cm}$, aumentando en 6 órdenes de magnitud en comparación con el PANI no dopado. El PANI dopado con SnCl_4 muestra la mayor conductividad después de



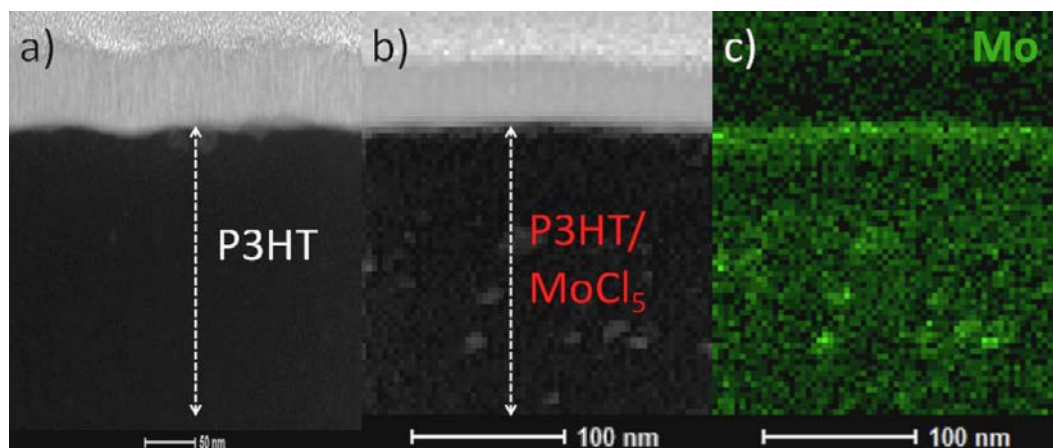
Curvas I-V de (a) PANI/1M HCl, PANI/MoCl₅ (100 ciclos) and PANI/SnCl₄ (60 ciclos) recién preparados y (b) PANI/1M HCl, PANI/MoCl₅ (100 ciclos) y PANI/SnCl₄ (60 ciclos) después de ser almacenados en vacío a 150 °C durante 100 minutos. El recuadro muestra el área a baja corriente de la Figura 1b. Las conductividades de (c) MoCl₅ y (d) SnCl₄ en función de el numero de ciclos de infiltración (medidos a temperatura ambiente). (e) Comparación de conductividades de PANI/1M HCl, PANI/SnCl₄ (60 ciclos) y PANI/MoCl₅ (100 ciclos) recién preparado, y después de ser almacenados en vacío a 150 °C durante 100 minutos.

60 ciclos de infiltración, con un valor de 1.03×10^{-5} S/cm, lo que supone un aumento de 5 ordenes de magnitud. Después de calentar las muestras dopadas a 150 °C durante 100 minutos en vacío, se observó que la conductividad del PANI dopado mediante el método tradicional (1M HCl) se redujo en alrededor de 7 ordenes de magnitud, lo que podría deberse a la deprotonación del PANI dopado y la evaporación del HCl.

La conductividad del PANI infiltrado con cloruros metálicos disminuyó mucho menos, lo que indica que los cloruros metálicos están atrapados en la matriz polimérica dando así mayor estabilidad al polímero dopado en condiciones severas. Las imágenes de SEM muestran que el proceso VPI no altera la morfología del PANI, por lo que este proceso de arriba-abajo puede usarse para el dopaje de PANI después de obtener la morfología deseada. De acuerdo con los resultados obtenidos mediante FTIR, Raman y espectroscopia UV-vis, los procesos de dopaje con MoCl_5 y SnCl_4 resultan en la oxidación del PANI y el presunto complejamiento de los cloruros metálicos con los átomos de nitrógeno del PANI. En consecuencia, la movilidad electrónica en las cadenas poliméricas aumenta considerablemente y la estructura es estable incluso a temperaturas elevadas en vacío.

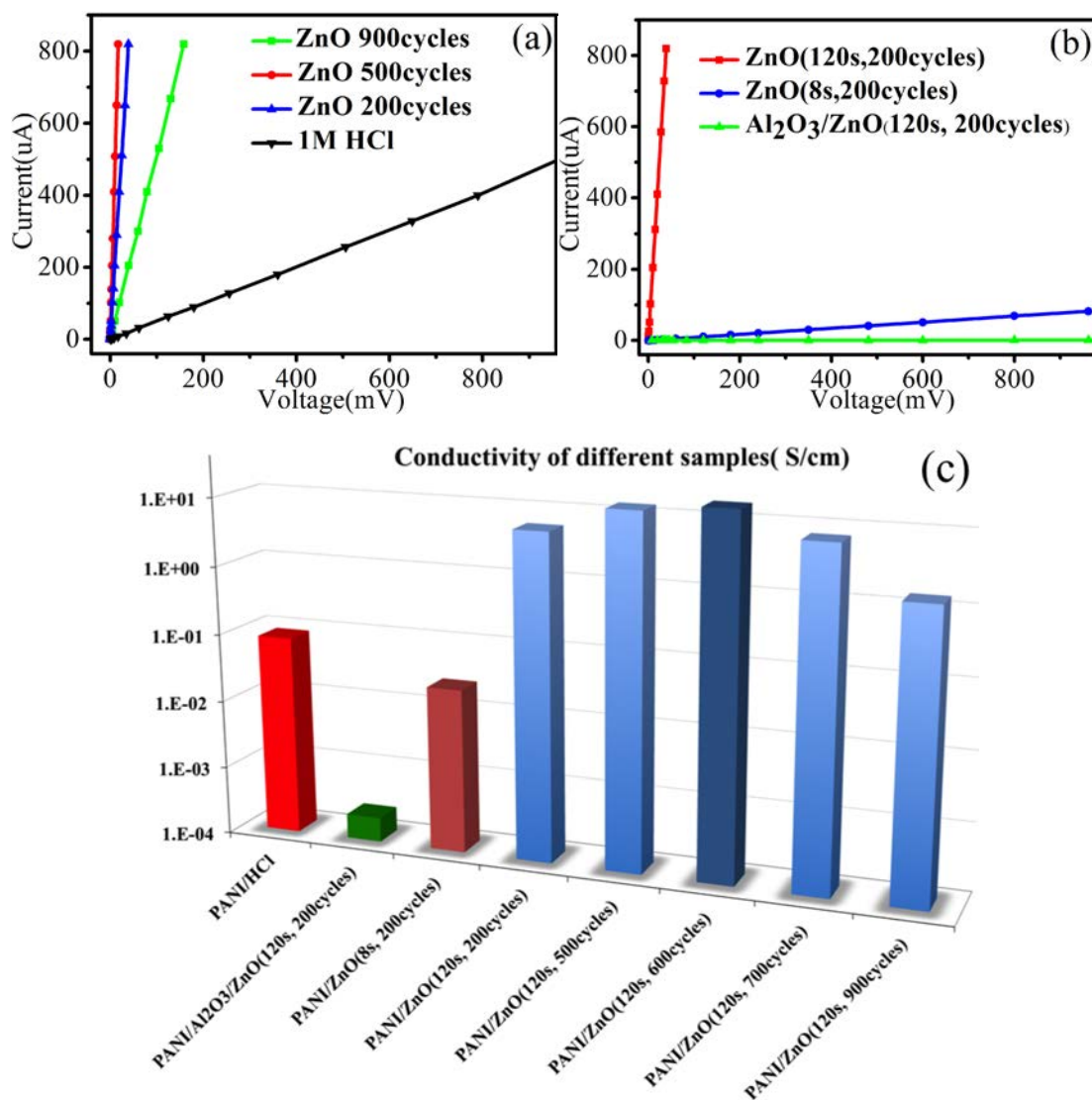


(a) Curvas I-V de P3HT sin dopar (negro) y P3HT dopado con MoCl_5 después de 50 ciclos (rojo), 100 ciclos (azul) y 300 ciclos (cian); (b) comparación de conductividades de P3HT sin dopar y P3HT dopado con MoCl_5 después de varios ciclos de infiltración (30, 50, 100, 200 y 300 ciclos) a 70 °C.

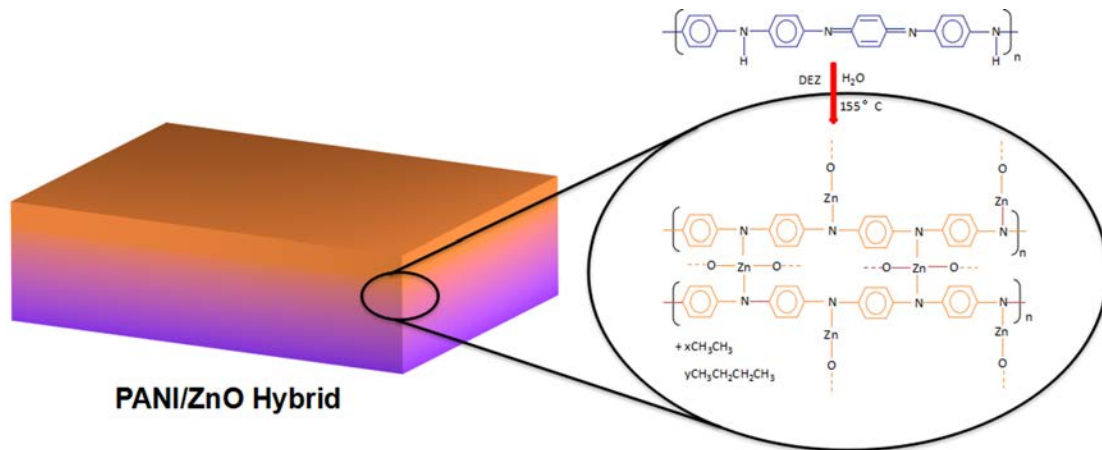


Imágenes de TEM de la sección transversal de (a) un film de P3HT sin dopar, (b) un film de P3HT dopado con MoCl_5 después de 100 ciclos y a $70\text{ }^\circ\text{C}$, y (c) mapeo elemental del Mo en la muestra de la imagen (b).

La segunda parte de esta tesis describe la infiltración en fase vapor de un solo precursor (VPI) y el dopaje del polímero conductor poli((3-hexil)tiofeno), P3HT. Para los procesos de infiltración, se usó el ácido de Lewis MoCl_5 como precursor a $70\text{ }^\circ\text{C}$. Las curvas I-V a temperatura ambiente mostraron dependencia con el número de ciclos VPI. Los valores más altos mostraron un aumento de 5 órdenes de magnitud en la conductividad, es decir, de $1.44 \times 10^{-5}\text{ S/cm}$ en el P3HT sin modificar a 3.01 S/cm después de 100 ciclos de infiltración. Las imágenes de SEM, muestran una película homogénea de P3HT en el estado prístino mientras que la película de P3HT infiltrada con MoCl_5 aparece decorada con islas manométricas. Una explicación posible a este cambio es la intercalación del MoCl_5 en la matriz polimérica, resultando en la dilatación del polímero. El análisis elemental de Mo mostró una cantidad considerable de Mo en la totalidad del polímero infiltrado. Se descubrió además que el P3HT infiltrado con MoCl_5 es muy estable. El espectro de absorción, el color observado y la conductividad medida cambiaron solo marginalmente después de la exposición de las muestras a condiciones ambientales durante 30 días. Los espectros de FTIR y XPS mostraron que el dopaje en fase vapor con MoCl_5 causa la oxidación local del P3HT, debido al carácter de base Lewis que el P3HT muestra en conjunto con el MoCl_5 . Los pares de electrones desapareados en los átomos de sulfuro de los anillos de tiofeno en P3HT pueden donar carga negativa al MoCl_5 cargándose ligeramente positivamente.



Curvas I-V de (a) PANI dopado con 1 M de HCl (referencia) y PANI dopado con ZnO con un numero variable de ciclos de infiltración como se indica en la leyenda. El tiempo de infiltración fue de 120 segundos para todas las muestras, (b) PANI con un recubrimiento compuesto por Al₂O₃ (como barrera de infiltración) y ZnO (verde) y PANI dopado con ZnO aplicando tiempos de exposición cortos (8 s, azul) y largos (120 s, rojo). El numero de ciclos para todas las muestras fue de 200. (c) Comparación de conductividades de PANI dopado con HCl, recubierto con ZnO y infiltrado con ZnO variando el tiempo de exposición y el numero de ciclos.



Vista macroscópica del material híbrido con óxido de zinc de dopaje no covalentemente unido y PANI dopado con el ácido de Lewis. Vista esquemática idealizada del enlace químico del Zn a la cadena de PANI después de la infiltración. Las cadenas poliméricas se entrecruzan mediante enlaces Zn-N. Al mismo tiempo, los grupos quinoides se convierten en grupos benzenoides.

En la última parte de esta tesis, la infiltración en fase vapor de pulsos múltiples (Multiple Pulsed Infiltration, MPI) se aplica para dopar el PANI. Para este proceso, se utilizaron dos precursores clásicos en ALD, dietilzinc (DEZ) y agua desionizada (H_2O) a $155\text{ }^\circ\text{C}$. Las curvas I-V a temperatura ambiente muestran que la conductividad de PANI infiltrado con Zn, aumenta a 18.42 S/cm , tres órdenes de magnitud mayor que la obtenida mediante el dopaje convencional con 1 M HCl ($8.23 \times 10^{-2}\text{ S/cm}$). Las imágenes de SEM no muestran ningún cambio en el polímero después de la infiltración, excepto por una ligera variación en el diámetro de las fibras de PANI, lo que se debe al depósito inevitable de ZnO en la superficie. El escaneo mediante EDX de la sección transversal de fibras individuales de PANI infiltrado con Zn, muestran una presencia significativa de Zn, en la totalidad del polímero. Con los espectros de FTIR, se descubrió que una reacción química entre el polímero y el precursor activada térmicamente, ocurre a temperaturas iguales o mayores a $155\text{ }^\circ\text{C}$. Los espectros de Raman muestran una evolución de las bandas que están relacionadas con el modo de vibración A_{1g} del enlace C-N, lo que indica la formación de un enlace entre el Zn y el N. La infiltración en fase de vapor de PANI con Zn resulta en material híbrido o compuesto que consiste en ZnO y PANI en la área subsuperficial del polímero. Estando químicamente unidos entre sí, el componente inorgánico y el orgánico, se dopan mutuamente beneficiando a la conductividad resultante.

Abstract

Over the past years, conductive polymers have been extensively investigated due to their tremendous importance as integral part of a wide range of electrical devices. For instance, studies have reported on enhanced mobilities of charge carriers in field-effect transistors (FETs) achieved by trap filling, improved charge injection in light-emitting diodes (LEDs) and, more recently, superior power conversion efficiencies in organic-photovoltaics. During the fabrication of the electrical devices, for improving their efficiency and lifetime, a crucial step is the realization of stable and controllably doped transparent highly conducting polymer thin films. Nowadays, the typical doping strategies for conducting polymers usually rely on charge-transfer redox chemistry (chemical or electrochemical *n/p*-doping processes), and non-redox acid-base chemistry (protonation of polyaniline), which result in permanent electrical conductivity. However, these doping processes are usually performed in the liquid state (solvents or solutions), which can introduce various chemical species, such as solvents or byproducts of chemical reactions, into the conducting polymer matrix, and in this way bring about negative consequences for the conductivity and stability of the polymer. In addition, doping processes in liquid state can also influence the morphology, structure and purity of the conducting polymer, which are very important for various applications. In this thesis, an alternative approach is introduced, which can avoid such negative influences and provide better control of the doping process. The “*Vapor Phase infiltration*” (VPI), a vacuum based process derived from the atomic layer deposition (ALD), is used for the top-down infiltration and doping of conducting polymers.

In the first part of this thesis, a single precursor vapor phase infiltration (VPI) process to dope polyaniline (PANI) is presented. As dopants, the vaporized Lewis acidic precursors SnCl_4 and MoCl_5 were used at a process temperature of $150\text{ }^\circ\text{C}$. The conductivities are extracted from four-point current-voltage measurements. From the room-temperature *I-V* plots, it was found that the conductivities of the infiltrated PANI are a function of the infiltration cycle number. After 100 cycles, the MoCl_5 -infiltrated PANI showed the highest conductivity, $2.93 \times 10^{-4}\text{ S/cm}$, which is a significant enhancement of up to 6 orders of magnitude in comparison to undoped PANI. SnCl_4 -infiltrated PANI showed highest conductivity after 60 cycles with a value of $1.03 \times 10^{-5}\text{ S/cm}$. The enhancement amounted to 5 orders of magnitude. After heating the infiltrated samples at $150\text{ }^\circ\text{C}$ in a vacuum environment for 100 min, it was found that the conductivity of traditionally doped PANI (1M HCl) decreased by nearly 7 orders of magnitude, which is likely to be due to the deprotonation of the doped PANI and evaporation of HCl. The conductivities of the VPI

doped PANI decreased to a much lower extent, which indicates that the infiltrated metal chlorides were trapped inside the polymer matrix, resulting in a higher stability of the doped polymer even in a harsh environment. SEM images showed that the VPI process did not alter the PANI morphology, thus the process can indeed be used for top-down doping after a desired morphology of PANI has been obtained. According to the FTIR, Raman and UV-vis spectra, the doping process with MoCl_5 and SnCl_4 results in an oxidation of PANI and presumably in complexation of the metal chlorides with the nitrogen atoms of PANI. As a result, the electron mobility along the polymer chains is significantly enhanced and the structure is stabilized even at an elevated temperature in a vacuum environment.

The second part of this thesis describes the single precursor VPI and doping of poly(3-hexyl)thiophene (P3HT). For the infiltration processes, the Lewis acid MoCl_5 was used as precursor at a process temperature of 70 °C. The room-temperature *I-V* plots show a dependency on the VPI cycles numbers. The highest values show an increase of 5 orders of magnitude for the conductivity, namely from 1.44×10^{-5} S/cm in the as-prepared P3HT to 3.01 S/cm after 100 infiltration cycles. SEM images show a homogeneous film of P3HT in the pristine state, while the MoCl_5 -infiltrated P3HT thin film became decorated with nanoscale islands. A possible reason for this change is the intercalation of MoCl_5 into the polymer matrix, resulting in a swelling of the polymer. Elemental mapping of Mo showed a considerable amount of the metal inside the bulk of the infiltrated polymer. It was further found that the MoCl_5 -infiltrated P3HT is temporally very stable. The absorption spectra, the perceived color, and the measured conductivities only marginally changed upon exposure of the samples to air in ambient conditions for 30 days. The FTIR and XPS spectra show that the doping with MoCl_5 from the vapor phase results in a local oxidation of P3HT, owing to the Lewis basic character that P3HT shows in conjunction with MoCl_5 . The lone electron pairs at the sulfur atoms of the thiophene rings in P3HT can donate negative charge to the MoCl_5 with themselves becoming rather positively charged.

In the last part of this thesis, the multiple pulsed vapor phase infiltration (MPI) process was applied to dope polyaniline (PANI). For the process, the two typical ALD precursors diethylzinc (DEZ) and deionized water (H_2O) were used at a process temperature of 155 °C. The room-temperature *I-V* plots showed the conductivity of Zn-infiltrated PANI increasing to 18.42 S/cm, up to three orders of magnitude higher than obtained upon conventional doping with 1 M HCl in wet-chemical ways (8.23×10^{-2} S/cm). SEM images did not show any obvious change of the polymer after infiltration, except a slight variation in the PANI fiber diameters, which is due to the unavoidable surface-deposited ZnO. The TEM and EDS scans of cross-sectioned regions of individual Zn-infiltrated PANI fibers show a significant presence of Zn in the bulk of the polymer. From FTIR spectra, it was found that a

thermally activated chemical reaction between the polymer and precursor takes place, which at temperatures equal or above 155 °C becomes pronounced. Raman spectra additionally showed an evolution of bands, which are associated with the C-N vibrational A_{1g} mode, indicating the formation of a bond between Zn and N. Infiltration of PANI with Zn from the vapor phase results in a hybrid or composite material consisting of ZnO and PANI in the subsurface area of the polymer. Being chemically bound to each other, the inorganic and organic components mutually dope each other for the benefit of the resulting conductivity.

Contents

Resumen.....	i
Abstract	vii
Contents	xi
Chapter 1 Introduction	1
1.1 Background.....	1
1.2 Atomic Layer Deposition (ALD).....	13
1.3 Vapor Phase Infiltration Process (VPI).....	16
1.4 Objective and Structure of the Thesis.....	27
Chapter 2 Experimental Techniques and Methods	29
2.1 X-ray Diffractometer.....	29
2.2 Fourier Transform Infrared (FTIR) Spectroscopy.....	31
2.3 Raman Spectroscopy	32
2.4 Electron Microscopy (SEM and TEM).....	32
2.5 Ultraviolet -Visible Spectroscopy.....	34
2.6 Atomic Force Microscopy (AFM).....	35
2.7 X-ray Photoelectron Spectroscopy (XPS).....	35
2.8 Assessment of the Electrical Conductivity	36
Chapter 3 Tuning the Conductivity of Polyaniline (PANI) by VPI Process.....	41
3.1. Introduction.....	43
3.2. Experimental Section.....	44
3.2.1 Preparation the Polyaniline (PANI) nanofibers Thin Film.....	44
3.2.2 Vapor Phase Infiltration Process of PANI Thin Film	44
3.2.3 Characterization	45
3.3 Results and Discussion	46
3.3.1 Assessment of the electrical conductivity	46
3.3.2 FTIR Spectroscopy	48
3.3.3 Raman Spectroscopy	50
3.3.4 SEM and EDX.....	52
3.3.5 Potential Reaction Schemes.....	53
3.4 Conclusion	55
Chapter 4 Controlling the Conductivity of Poly(3-hexyl)thiophene (P3HT) by Low Temperature VPI Process.....	57
4.1 Introduction	59
4.2 Experimental Section	62
4.3 Results and Discussion	64
4.3.1 Assessment of the electrical conductivity	64
4.3.2 UV-Vis spectroscopy	65
4.3.3 Raman spectroscopy.....	66
4.3.4 Infrared spectra.....	68
4.3.5 X-ray diffraction.....	69
4.3.6 SEM, AFM and TEM.....	70
4.4 Conclusions	72
Chapter 5 Conductive Polymer-Inorganic Hybrid Materials through Synergistic Mutual Doping of the Constituents.....	75
5.1 Introduction	77

5.2 Experimental Section	79
5.3 Results and Discussion	81
5.3.1 Assessment of the electrical conductivity	81
5.3.2 Electron Microscopy	84
5.3.3 Infrared Spectra.....	87
5.3.4 Raman Spectra.....	88
5.3.5 X-ray diffraction	89
5.3.6 X-ray Photoelectron Spectra.....	90
5.4 Conclusion	93
Chapter 6.....	95
Bibliography	97
List of Publications.....	111
Acknowledgements	113

Chapter 1

Introduction

1.1 Background

Polymers exhibiting electrical, electronic, optical and magnetic properties similar to metals, are termed "intrinsically conducting polymers" (ICP), or "synthetic metals"¹. Besides the aforementioned properties, they usually also retain the mechanical properties, processibility, etc., that are common for conventional polymers. In general, conducting polymers can be classified into ionically and electronically conducting polymers². Herein, ionically conducting polymers are commonly called polymer electrolytes, as the conductivity is given by the mobility of ions within the polymer. Electronically conducting polymers are composed of conjugated π -electron systems, which enable the mobility of electrons. A third class of "conducting polymers" is derived from physical mixtures of insulating polymers with a conducting material such as a metal or carbon powder distributed throughout the material. In this thesis, the term "conducting polymers" will be limited to conjugated conducting polymers only.

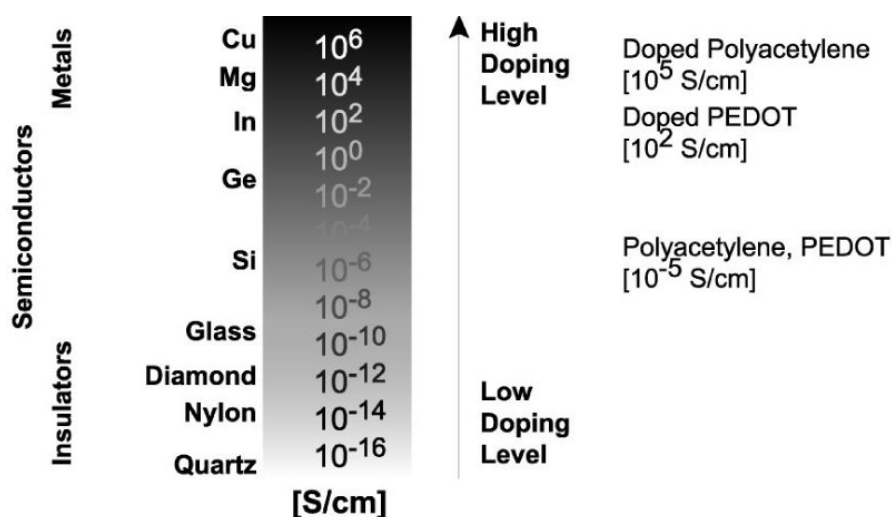


Figure 1.1 Conductivities of polyacetylene and PEDOT in comparison with common conductors and insulators. The conductivity typically increases with the doping level.

Traditionally, polymers were considered to be insulators. However, copper-like electrical conductivities were reported in polyacetylene films by Alan G. MacDiarmid et al., which changed the paradigm^{3,4}(Figure 1.1). The conductivity was induced by doping polyacetylene with AsF₅, which resulted in a conductivity increase by 9 orders of magnitude³. This pioneering work initiated the research on other conducting polymers and various stable conducting polymers such as polyaniline (PANI), polypyrrole (PPy), and polythiophene (PTh) were reported since the late 1970s.

Conjugated organic polymers are usually either electrical insulators or semiconductors. Those polymers, which after doping show conductivities increasing by several orders of magnitude from the semiconductor regime, are generally referred to as "electronic polymers". Such polymers attracted considerable attention since 1990 in line with the development of light-emitting diodes (LEDs)⁵, solar cells⁶⁻⁹, and organic photovoltaics¹⁰⁻¹³ as well suitable components for device fabrication. Because of the great importance of the conducting polymers for emerging technologies, Heeger, MacDiarmid, and Shirakawa were awarded the Nobel Prize in chemistry in 2000, in recognition of their great contributions to the discovery and development of conducting polymers.

Molecular structure of conducting polymers

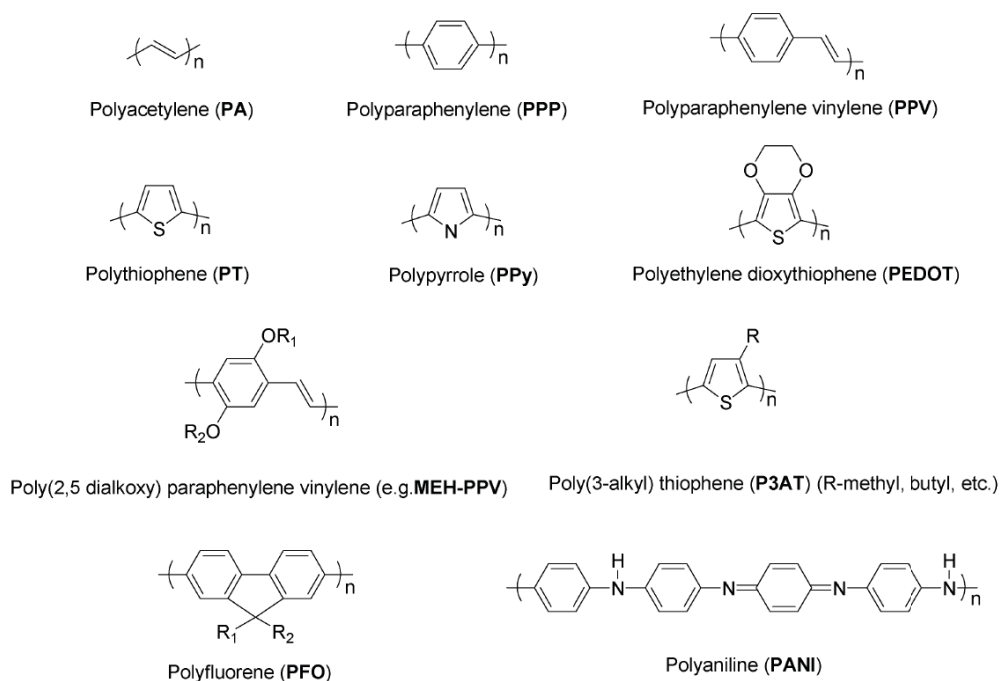


Figure 1.2 Molecular structures of building blocks of various conducting polymers. The alternating double bonds constitute a conjugated π -electron system.

The unique characteristic of a conducting polymer is the conjugated π -electron system along the polymer backbone. In such conjugated polymers, the electron orbitals of carbon are in the sp^2p_z configuration and contain one unpaired electron (π -electron) per carbon atom. The orbitals of successive carbon atoms along the polymer backbone overlap, allowing the delocalization of the electrons along the polymer chain. Such delocalization acts as a "highway" for the charge carriers. Figure 1.2 shows the chemical building blocks of some important conjugated polymers, such as polyacetylene (PA), poly(*p*-phenylene) (PPP), poly(*p*-phenylene vinylene) (PPV), polythiophene (PT), polypyrrole (PPy), polyethylene dioxythiophene (PEDOT), poly(2,5-dialkoxy)(*p*-phenylene) vinylene (e.g. MEH-PPV), poly(3-alkyl)thiophene (P3AT), polyfluorene (PFO), and polyaniline (PANI). If suitable doping processes are applied, such polymers will become conductive.

The classical example of a conducting polymer is polyacetylene, $(-CH)_n$, showing the simplest possible chemical structure with alternating single (σ) and double (π) bonds. Two configurations are possible with respect to the locations of the hydrogen atoms: *cis*-polyacetylene (hydrogen atoms located on the same side as the double bond) and *trans*-polyacetylene (hydrogen atoms located opposite to the double bond). The energy gap between occupied (π) and empty (π^*) molecular orbitals of the undoped *trans*-polyacetylene is defined by the pattern of alternating single (long) and double (short) bonds, with an additional contribution originating from the coulomb electron-electron repulsion. The interchange of single and double bonds results in an equivalent ground state, which means *trans*-polyacetylene is a degenerated conjugated polymer. On the other hand, *cis*-polyacetylene and the further conjugated polymers do not have such an equivalent ground state.

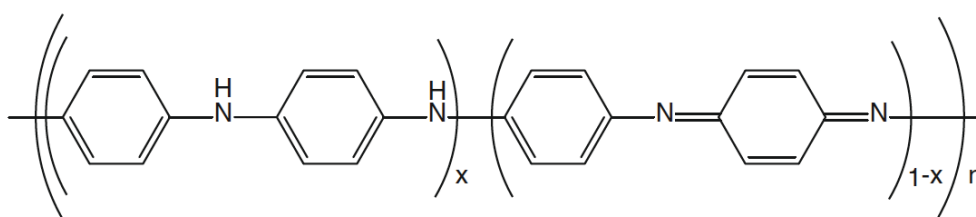


Figure 1.3 Schematic of the chemical structures of polyaniline.

Among the variety of conducting polymers, the most studied polymer is polyaniline (PANI). It found application in the fields of electrochromic devices¹⁴, drug delivery¹⁵, gas separation¹⁶, sensor applications¹⁷⁻¹⁹, rechargeable batteries^{20,21}, catalysts²² and energy storage devices²³. Chemically, PANI can switch between three idealized oxidation states²⁴, namely, leucoemeraldine (white/colorless), emeraldine (green for the emeraldine salt, blue for the emeraldine base), and pernigraniline (blue/violet). Figure 1.3 depicts the chemical structures

of leucoemeraldine with $x = 1$ (fully reduced state) and the pernigraniline with $x = 0$ (fully oxidized state). In the latter case the links between C_6 rings consist of imine groups instead of amine groups. The most important form of polyaniline is the emeraldine form with $x = 0.5$, often referred to as emeraldine base (EB). If doped (protonated) it is called emeraldine salt (ES). The EB shows great stability at room temperature. Upon doping with acids²⁵, the resulting ES shows high electrical conductivity. The other two mentioned forms of polyaniline, leucoemeraldine and pernigraniline, are poor conductors, even if doped with acids.

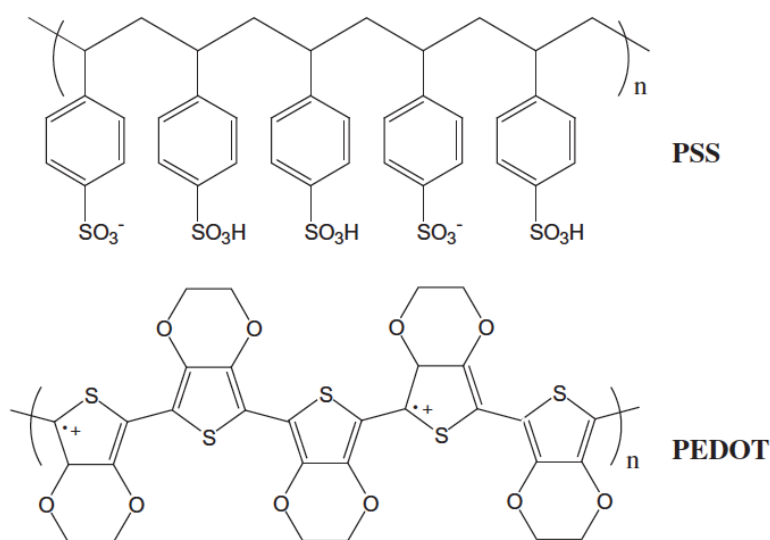
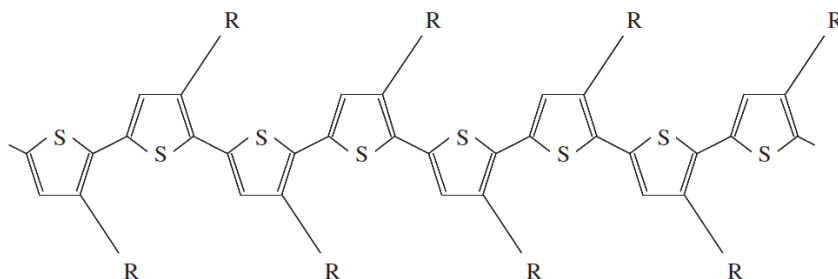


Figure 1.4 Chemical structure of PEDOT:PSS.

Plenty important applications were foreseen for conducting polymers, mainly because of their combination of properties of metals and polymers. However, many of the applications cannot be realized easily, which is mainly due to the poor processability of many of the conducting polymers. Most of the conducting polymers are in the conductive state insoluble and intractable. However, poly(3,4-ethylenedioxythiophene):poly(styrenesulfonate) (PEDOT:PSS, chemical structure shown in Figure 1.4) can be dispersed in water and some polar organic solvents, thus high-quality PEDOT:PSS films can be readily prepared by processing from solutions^{26,27}. The reason for this processability lies in the PSS, which stabilizes the PEDOT chains in various solvents. The PEDOT chains with a molecular weight of about $1000\text{-}2500\text{ g mol}^{-1}$ are much shorter than the PSS chains with approximately $400,000\text{ g mol}^{-1}$ ²⁸, thus the short PEDOT chains align with the long PSS chains due to coulombic attraction. In consequence, PEDOT:PSS becomes a polyelectrolyte consisting of hydrophobic PEDOT and hydrophilic PSS. For applications, PEDOT:PSS films are very attractive, since

they show high transparency in the visible range, high mechanical flexibility, and excellent thermal stability. A PEDOT:PSS film, as prepared from an aqueous solution, shows conductivities below 1 S cm^{-1} , which is significantly lower than the conductivity of the inorganic transparent conductive oxide indium tin oxide (ITO). For an application as transparent electrode in optoelectronic devices, this value is too low and needs to be increased. In 2002, Kim *et al.* reported an enhancement of the conductivity of PEDOT:PSS after adding dimethyl sulfoxide (DMSO) or dimethylformamide (DMF) to the aqueous PEDOT:PSS solution²⁹. Since then, many further methods have been reported³⁰⁻³⁷. The conductivity of PEDOT:PSS from its aqueous solution can be enhanced by adding polar organic solvents with a high-boiling point, ionic liquids and surfactants or through post-treatment of PEDOT:PSS films with various compounds, such as high-boiling point polar solvents, salts, cosolvents, zwitterions, or organic and inorganic acids. More recently, conductivities of more than 3000 S cm^{-1} were measured after treatment of PEDOT:PSS films with sulfuric acid. Such values are comparable to those of ITO³⁸. The resulting conductive PEDOT:PSS films are stretchable, which adds value if compared to the brittle ITO, making PEDOT:PSS a very promising material as the next-generation transparent electrode material.

(a) RR-P3HT ($R = \text{C}_6\text{H}_{13}$)



(b) RRa-P3HT ($R = \text{C}_6\text{H}_{13}$)

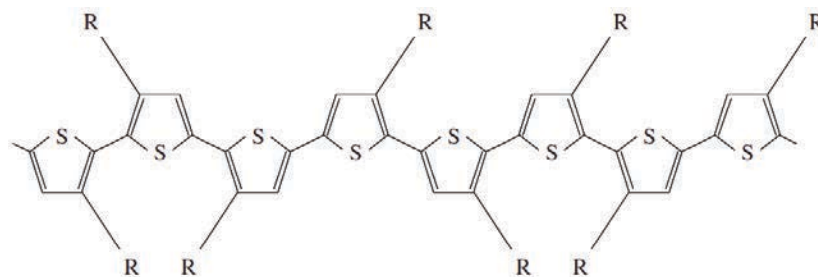


Figure 1.5 Chemical structures of (a) RR-P3HT (regioregular P3HT) and (b) RRa-P3HT (regiorandom P3HT).

Poly(3-hexyl)thiophene (P3HT) is a further highly promising conjugated polymer with good solubility, environmental stability and high field-effect mobility ($0.2 \text{ cm}^2 \text{ V}^{-1} \text{ s}^{-1}$)³⁹.

The transport mechanism of the charge carriers in P3HT has attracted great attention from the viewpoint of physics. P3HT has a non-degenerate electronic structure and polarons or bipolarons are considered to be the dominant charge carriers⁴⁰. The most important characteristic of P3HT is its regioregularity, i.e., the percentage of stereoregular head-to-tail attachments of the hexyl side-chains to the thiophene rings. At room temperature, the difference in the charge-carrier mobilities of the regioregular and regionrandom isomers, the structure of which are shown in Figure 1.5 (a) and (b), may be at least two orders of magnitude. In regioregular P3HT (RR-P3HT), the hexyl side chains on adjacent thiophene rings are ordered in an alternating head-to-tail conformation, while in regiorandom P3HT (RRa-P3HT), the hexyl side chains are arranged randomly with 50% being a head-to-tail conformation. In the case of RR-P3HT, owing to the self-packing of the hexyl side chains driven by hydrophobic interactions, the self-stacking of thiophene rings between adjacent polymer chains facilitates the formation of ordered microcrystalline regions with a lamellar structure that improves the carrier mobility^{41,42}.

Charge carriers in the conducting polymers

For π -conjugated conducting polymers, solitons, polarons and bipolarons are proposed to interpret the enhancement of conductivity after doping. In the case of the conjugated *trans*-polyacetylene with a degenerate basic state, the charge carriers are solitons and polarons, while in the nondegenerate *cis*-polyacetylene, polyaniline, polypyrrole, and polythiophene, etc., in their basic state polarons and bipolarons act as charge carriers. The soliton is formed by an unpaired π -electron resulting from the formation of radicals⁴⁴. It can be delocalized along the conjugated *trans*-polyacetylene chain^{45,46}. The neutral soliton can be either oxidized to lose an electron and form a positive soliton, or reduced to gain an electron and form a negative soliton. Due to the unpaired electron, the soliton possesses a spin of 1/2, whereas the positive and negative solitons have no spin. The electronic energy level of the soliton is located in the middle of the bandgap of *trans*-polyacetylene.

Polarons are the main charge-carriers in conducting polymers, such as the degenerate basic state *trans*-polyacetylene and other non-degenerate basic state conjugated polymers. The positive polaron is a radical cation with positive charge, and the negative polaron is a radical anion with negative charge. The positive polaron is formed after oxidation of the conjugated polymer chain, and the negative polaron is formed after its reduction. The appearance of the polarons produces two new polaron energy levels in the bandgap of the conjugated polymers. Both the positive polaron and negative polaron possess a spin of 1/2. Bipolarons are charge carriers with double charges, resulting from coupling of two positive or

negative polarons within a conjugated polymer chain. The bipolaron has no spin. Generally, positive and negative bipolarons correspond to the model of holes and electron pairs.

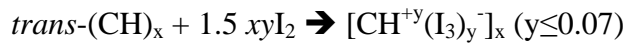
Doping Characteristics

The charge injection into conjugated, semiconducting macromolecular chains, termed "doping", is typically dissimilar to the doping process of the traditional inorganic semiconductors silicon and germanium. The polymer doping process results in various interesting and important phenomena that define this research field⁴⁷. Controlled introduction of impurities into the semiconductor matrix is the common method to dope inorganic semiconductors. Such procedure allows for deliberately tuning the band alignment at interfaces and markedly increasing the conductivity already at ultralow doping ratios. The reason is that each covalently bound dopant atom donates one mobile charge to the highly crystalline and ultra-pure semiconductor matrix^{48,49}. In contrast, the doping process of conjugated polymers involves either charge-transfer redox chemistry, that is, the chemical reduction (*n*-type doping) or oxidation (*p*-type doping) donates or retrieves electrons to or from the π electron system of the polymer backbone^{50,51}, or acid-base chemistry, which is usually applied upon doping of polyaniline⁴⁷. In the *n*-doped state, the main chain of the polymer is reduced and a cation is electrostatically bound for keeping the overall charge of the whole molecule neutral. Excess electrons within the main chain make the polymer *n*-type conductive. In the *p*-doped state, the polymer is oxidized and the opposite case occurs. The resulting empty electron orbitals correspond to holes in semiconductors and make the polymer a *p*-type conductor. Upon doping, an initially insulating or semiconducting polymer with conductivities in the range of 10^{-10} to 10^{-5} S/cm becomes metallically conducting with conductivities between 1 and 10^4 S/cm¹. A controlled addition of small non-stoichiometric quantities of dopants usually results in significant changes in the electronic, electrical, magnetic, optical, and structural properties of the conjugated polymer. Importantly, the doping process is reversible. Appropriate chemical treatment will restore the original conjugated polymer with little or no effect on the polymer structure. Both, the doping and the dedoping process, may be carried out chemically or electrochemically. Besides, also some doping processes that do not introduce dopant ions are known⁵². Such processes include "photo-doping" and "charge-injection doping". In those processes, transitory "doped" species are produced, which have similar spectroscopic signatures to polymers that contain dopant ions.

(1) Chemical doping

Polyacetylene can be made conductive by chemical doping. Depending on the selected chemical process the polymer may become either *p*- or *n*-type conducting.

p-doping, also called partial oxidation doping, is achieved with a partial oxidation process of the conjugated π -electron system of the polymer backbone in order to create polarons. Among the possible *p*-dopants, I_2 , Br_2 , AsF_5 , or $(NO)PF_6$ are the most common ones. After a *p*-doping process with I_2 , the conductivity of *trans*-polyacetylene or *trans*-(CH)_x typically increases from ca. 10^{-5} S/cm to ca. 10^3 S/cm^{3,4}. The following reaction illustrates the underlying chemical process^{53,54}.



In contrast, *n*-doping is a partial reduction process of the π -electron system of a conjugated polymer in order to create negative charge carriers. Some strong reducing agents, such as alkali metals, alkaline earth metals, liquid sodium amalgam or sodium naphthalene $(Na(Nphth))^3$, etc., can be used as *n*-type dopants. After treating *trans*-(CH)_x with $Na(Nphth)$, its antibonding π -electron system is partially populated with electrons, resulting in the conductivity of the polymer increasing up to 10^3 S/cm. The following reaction illustrates the underlying chemical process^{53,54}.



(2) Electrochemical doping

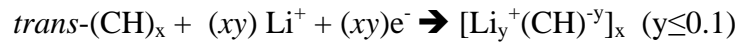
Although chemical doping is an efficient process, it is often difficult to control. Quantitative doping to the highest charge carrier concentrations results in reasonably high quality materials. However, attempting to obtain intermediate doping levels often makes the doping inhomogeneous. Therefore, electrochemical doping was introduced to solve this problem⁵⁵. Such doping is performed by electrochemical oxidation or reduction of a conjugated polymer placed onto an electrode. During the electrochemical doping process, the electrode supplies charge to the conjugated polymer and a redox reaction is induced, while ions from the electrolyte diffuse into the polymer to compensate the overall electronic charge. The doping level is determined by the potential applied between the conjugated polymer and the counter electrode; in equilibrium, the doping level is precisely defined by that voltage. Thus, doping at any level can be obtained by setting the electrochemical cell to a defined

potential and allowing the system to reach an electrochemical equilibrium, where no current flows.

Electrochemical *p*-doping can be accomplished by anodic oxidation. The conjugated polymer chain becomes oxidized and loses an electron, while gaining a hole. The charges are balanced with counteranions (ClO_4^-) from the electrolyte solution. The following reaction illustrates the process on the example of *trans*-(CH)_x being immersed into a solution of LiClO_4 in propylene carbonate⁵⁵.



Likewise, electrochemical *n*-doping can be carried out by cathodic reduction. The conjugated polymer main chain becomes reduced and gains an electron. The charges are balanced with countercations (Li^+) from the electrolyte solution. The following reaction illustrates the process on the example of *trans*-(CH)_x being immersed into a solution of LiClO_4 dissolved in tetrahydrofuran⁵⁶.



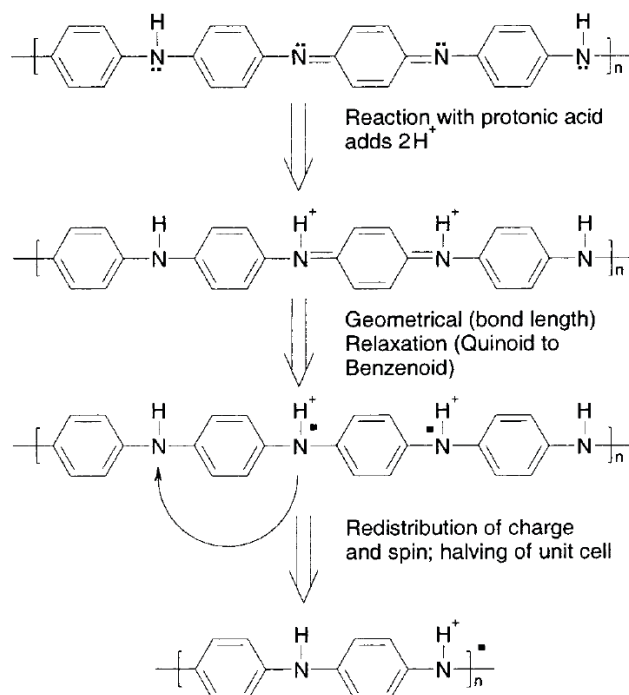
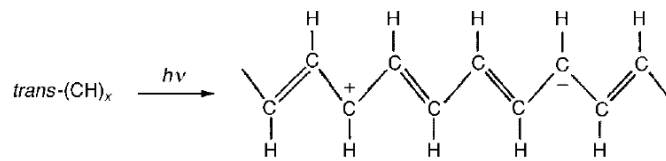
(3) Doping of polyaniline by acid-base chemistry

Figure 1.6 Protonation-induced spin unpairing in polyaniline and the conversion from insulating to metallic behavior with no change in the total number of electrons. Reproduced with permission from the American Chemical Society⁴⁷.

Polyaniline provides the prototypical example of a chemically distinct doping mechanism than previously described⁵⁷. The protonation by applying acid-base chemistry leads to an internal redox reaction and a resulting transition from the emeraldine base to the metallically conducting emeraldine salt. The electrical conductivity is significantly enhanced by up to nine or ten orders of magnitude (around 3 S/cm)⁵⁸⁻⁶⁰. This type of doping is different from redox doping described above in that the total number of electrons in the polymer backbone does not change during the doping process. Only the energy levels are rearranged upon doping. The doping mechanism is shown in Figure 1.6⁴⁷. The chemical structure of the emeraldine base is a copolymer composed of benzenoid rings and quinoid rings. Upon protonation to the emeraldine salt, the proton-induced spin unpairing mechanism leads to a structural change with one unpaired spin per repeating unit, but with no change in the number of electrons^{61,62}. The result is a half-filled band and, potentially, a metallic state with a positive charge in each repeating unit. The associated counterion (e.g. Cl^- , HSO_4^- , DBSA^- , etc.) is not shown in Figure 1.6.

(4) Photodoping

During the photoexcitation process of a semiconducting polymer, the electrons are transferred from the filled π -orbital to the empty π^* -orbital. That is, the polymer is locally oxidized and reduced in spatial proximity by photoabsorption and charge separation in the same polymer main chain (electron-hole pair creation and separation into "free" carriers). When *trans*-(CH)_x, for example, is exposed to radiation of energy greater than its band gap, electrons are promoted across the gap and the polymer undergoes "photo-doping". Under appropriate experimental conditions, spectroscopic signatures characteristic of solitons can be formed (Schematic 1)⁶³.



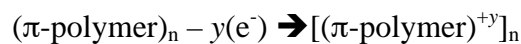
Schematic 1. Photodoping of *trans*-(CH)_x.

For simplicity, the positive and negative solitons are illustrated as charges residing on one of the CH units. However, they are actually delocalized over ca. 15 CH units. When the irradiation is discontinued, they disappear rapidly because of the recombination of electrons and holes. If a potential is applied during irradiation, the electrons and holes will separate and photoconductivity is observed.

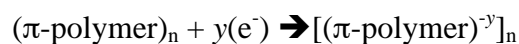
(5) Charge injection doping

Charge injection doping refers to charge injection at the interface of a metal and a semiconducting polymer (MS). Both holes and electrons can be injected from metallic contacts into the π -orbital and π^* -orbital, respectively:

- (1) injection of holes into an otherwise filled π -orbital



- (2) injection of electrons into an empty π^* -orbital



In the case of charge injection at an MS interface, the conjugated polymer becomes reduced or oxidized, that is, electrons are added to the empty π^* -orbital or removed from the filled π -orbital. However, the polymer is not doped in the chemical or electrochemical sense, because no counterions are introduced during the charge injection doping process. With charge injection doping, even superconductivity was observed in a polythiophene derivative. The application of an appropriate potential across the MS interface can lead to a surface charge layer, the "accumulation" layer, that has been extensively investigated for conducting polymers^{52,64,65}. In some conjugated polymer, such as P3HT or polyacetylene $(\text{CH})_x$, the resulting charges evolve without the presence of a dopant ion. Spectroscopic studies of $(\text{CH})_x$ show signatures characteristic of solitons and a mid-gap absorption band observed in chemically and electrochemically doped polymers.

Each of the mentioned charge-injection doping methods can result in unique and important phenomena. Electrical conductivity induced by chemical and/or electrochemical doping methods is permanent, but only as long as the carriers are chemically compensated or until the carriers are removed on purpose by a "dedoping" process. Upon photoexcitation, the photoconductivity is transient, and lasts only until the excited species are either trapped or decay back to the ground state. In the case of charge injection at the metal-semiconductor (MS) interface, only a biasing voltage is applied, the electrons can enter the π^* -orbital and/or the holes enter the π -orbital.

In consequence, for obtaining permanent electrical conductivity, the best doping strategies are the chemical and/or electrochemical processes. However, such doping processes are usually performed in liquid state, which can introduce various chemical species, solvents or byproducts into the polymer matrix. This may have various negative consequences for the conductivity or stability of the polymer. The morphology, structure and purity, which are very important for many applications, such as, field-effect transistors (FETs)⁶⁶⁻⁶⁸, light emitting diodes (LEDs)⁶⁹⁻⁷¹, and organic photovoltaics⁷²⁻⁷⁴, etc. will be influenced. For avoiding these negative influences and avoiding liquid state doping processes, a vacuum based process, the *Vapor Phase Infiltration*⁷⁵, which is derived from atomic layer deposition (ALD)^{76,77}, can be exploited for the top-down infiltration and doping of conducting polymers. This new approach is described in this thesis.

1.2 Atomic Layer Deposition (ALD)

Atomic layer deposition: general concepts

Atomic layer deposition (ALD), originally called atomic layer epitaxy (ALE), was developed in the 1970s by Suntola *et al.* to meet the needs of fabricating high-quality and large-area ZnS films for a use in thin-film electro-luminescent flat panel displays⁷⁸. The first application of such a display was the display board at the Helsinki Airport installed in 1982. Since then, more than 2 million electro-luminescent displays have been fabricated with this new process⁷⁹. Since it was found that most of the films grown in this way do not show epitaxial type of growth, the new deposition method was renamed to Atomic Layer Deposition (ALD). In the middle of 1990s, ALD was identified as method-of-choice for manufacturing microelectronic devices^{80,81}. Its enormous take off occurred in the 2000s, motivated by the need of miniaturizing the dimensions of devices and increasing aspect ratios in integrated circuits. Molecular layer deposition (MLD), an organic modification of ALD, evolved after Yoshimura *et al.* deposited polyimide films applying the same operating principle as in ALD, but with organic molecules. It was first referred to as either alternating vapor deposition, vapor deposition polymerization, or layer-by-layer growth⁸²⁻⁸⁴. Recently, molecular layer deposition (MLD), as well as combinations of it with ALD, have brought about various hybrid organic/inorganic materials with new and/or altered properties in comparison to the individual or parent materials.

Atomic layer deposition is a unique technique for the deposition of conformal, pinhole free and homogeneous thin films. It can be considered as a similar, although chemically distinct, case of the chemical vapor deposition (CVD). The difference among them refers to the chemical reaction being separated into two self-limiting and individual surface reactions⁸⁵. The separation of the reactions is achieved by keeping the precursors separate during the process. Such a separation brings about a self-limiting growth mechanism and thus leads to the control of the film growth on the atomic/molecular level. While the CVD process deposits materials as a function of time, ALD films grow as a function of the cycle number. Figure 1.7 schematically illustrates a growth cycle of a metal oxide (MO_2) by ALD, in which M stands for any metal, such as Ti, Zr, or Hf. For such deposition, a metal-containing precursor ML_4 (L: ligand) is used as metal source and H_2O as oxygen source. One such MO_2 ALD deposition cycle consists of following steps: 1) pulse of the first precursor, ML_4 , 2) its chemisorption and surface saturation during exposure, 3) purge to remove excess precursor, and 4) pulse of the second precursor, H_2O , followed by 5) its reaction with the adsorbed ML_4 during exposure, and 6) purge to remove excess H_2O and reaction byproducts (Figure 1.7 (a)). In step 1, the

surface is exposed to the ML_4 vapor pulse. The precursor can react with the functional surface sites to form a stable and saturative chemisorbed layer. After purging the excess ML_4 vapor and byproducts, the same procedure is repeated with H_2O vapor to complete a full ALD growth cycle. These steps are repeated and each cycle will add a sub-monolayer quantity of the deposit to the surface until a thin MO_2 film is formed. The growth per cycle (GPC) is defined as the average added to the growing film per full cycle. The self-limitation of the surface reactions in ALD allows a thickness control simply by controlling the number of cycles⁸⁶.

In both, the ALD and CVD processes, all surfaces exposed to the precursor vapor are being coated. This indicates that highly uniform thin films can be formed on various substrates. However, in contrast to ALD, where the two precursors are temporally separated (Figure 1.7 (b)), in CVD the vaporized precursors are simultaneously fed into the reactor with a carrier gas (Figure 1.7 (c)). With this procedure, the precursor lifetime in a CVD process is not long enough to diffuse into deep cavities of complicated 3D substrates prior to the reaction with the counter precursor. Thus, the CVD process will produce less conformal thin-films than the ALD process, especially with structurally complicated substrates.

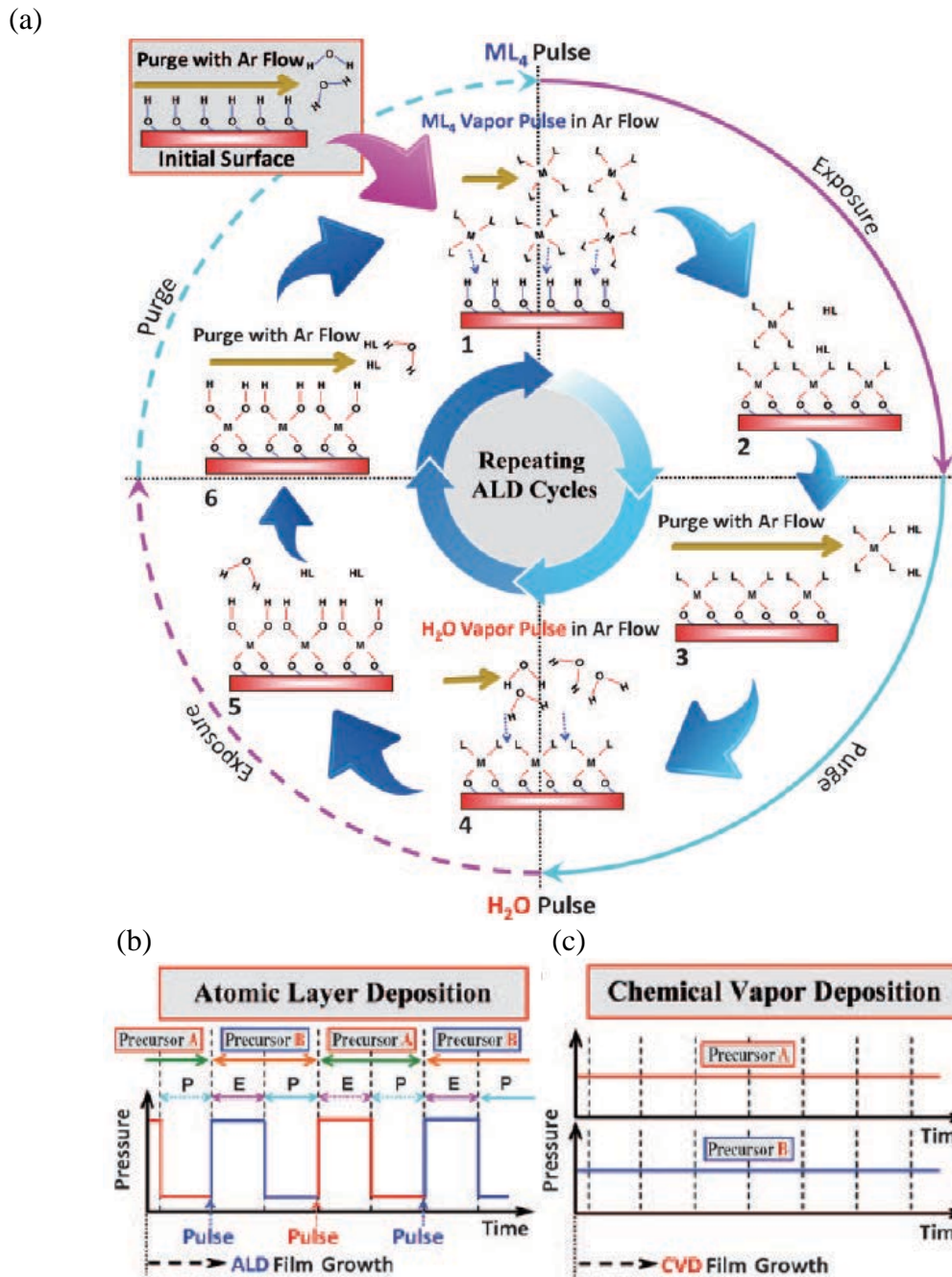


Figure 1.7 Schematic of an ALD/MLD process with a comparison to a CVD process. (a) ALD is a cyclic and self-limiting process, where a substrate is exposed to the precursor ML_4 (1), the precursor saturates and is purged (2,3), the second precursor is pulsed, in this case H_2O (4), and finally the second precursor and byproducts purged (5,6). In a typical process, the surface chemistry is restored at the end of each cycle. (b) E and P denote exposure and purge, respectively. The alternating E and P steps create an alternating pressure profile as a function of time, while a CVD process (c) has a nearly constant pressure profile, where the precursors are introduced into the reactor simultaneously. Reproduced with permission, Wiley-VCH⁸⁵.

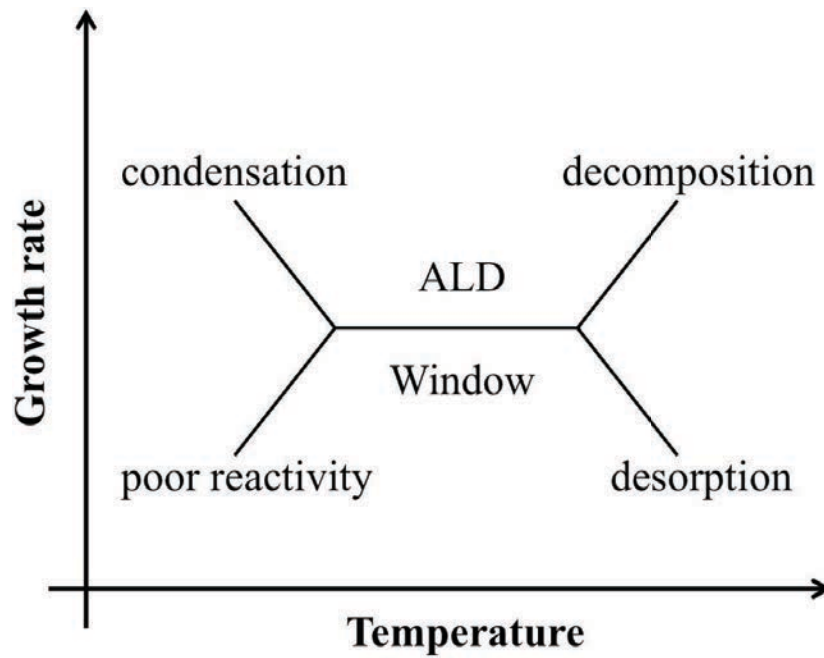


Figure 1.8 Schematic of the ALD process window. Influence of the deposition temperature on the growth rate.

During the ALD process, a determining parameter for the growth rate is the deposition temperature. Figure 1.8 shows the so-called idealized “ALD-window”, which defines the temperature range in which the thin film formation occurs under self-limiting conditions. Outside this temperature range, the growth is limited by various factors. At lower temperatures, the precursors may condense on the substrate, which can lead to CVD like growth, or the surface reaction may not happen because of insufficient activation energy. At too high temperatures, precursor decomposition may bring about an enhanced ALD growth rate, or the thermal energy may be too high, resulting in desorption of the precursor from substrate⁸⁶⁻⁸⁸.

1.3 Vapor Phase Infiltration (VPI)

1.3.1 Bio-inspired background of VPI

Most living organisms rely on hard tissues for support, protection, nutrition, and defense. Biomineralization is the dominant strategy in nature for hardening of soft tissue and manifests an astonishing diversity of bioceramic structures with exquisite microarchitectures that show specific physical properties as a result of environmental adaptation⁸⁹⁻⁹¹. Although the variety of architectures appears virtually infinite, Ca-, Si-, and Fe-based minerals are the

most commonly encountered⁹². As a basic principle, the hardness of these composites is largely governed by the type of mineral incorporated⁹³ and the degree of mineralization⁹⁴.

In 1980, Gibbs and Bryan reported first on the copper level in the jaws of the marine polychaete worm *Glycera* sp being up to 13% w/w, and they concluded that the presence of copper might play an important role in mechanically hardening the proteinaceous material⁹⁵. In 2002, Lichtenegger *et al.* showed that in *Glycera* jaws, a dominant fraction of copper is deposited as a biomineral⁹⁶. They found that, in spite of the low degree of mineralization, *Glycera* jaws show an extraordinary resistance to abrasion. Figure 1.9 (a) shows an optical micrograph of a *Glycera* jaw. *Glycera* is armed with a set of four such jaws, each of which is about 1.5 mm long and jet black, with a very sharp and mechanically stable tip that is used by the worm to penetrate the integument of its prey and inject the venom. Electron microprobe experiments on a ground and polished *Glycera* jaw showed the presence of copper in high concentration in the tip region. In agreement with the findings of Gibbs and Bryan, the copper concentration decreased significantly along the line from the tip to the base⁹⁵. The local copper distribution in an oblique cross section of the tip is depicted in Figure 1.9 (b) (the dark hole in the middle is the venom canal). Figure 1.9 (c) shows the local chlorine distribution. The occurrence of chlorine in the sample was strongly correlated with the local concentrations of copper. Except for the tip, the rest of the sample did not contain detectable levels of chlorine. Backscattered electron imaging (BEI) was used as a complementary technique to visualize the copper distribution. The contrast is due to differences in the atomic number *Z*, and therefore in the atomic mass, with bright regions indicating heavier elements. The BEI image (Figure 1.9 (d)) is in perfect agreement with the copper distribution obtained from the electron microprobe element map.

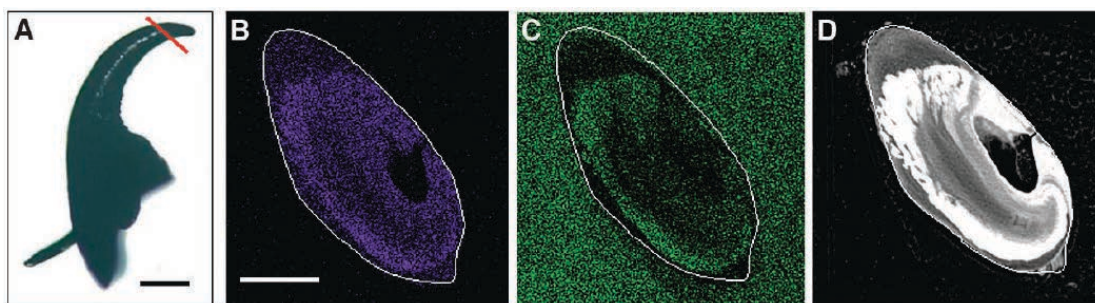


Figure 1.9 (a) Optical macrograph of a *Glycera* jaw. The scale bar corresponds to 0.2 mm. The red line denotes the plane of the cross section used for the element analysis. (b) Electron micrograph with a copper (Cu) EDS map. The white line denotes the outline of the sample. Scale bar, 50 μm . Regions with higher copper concentration appear bright. (c) Electron micrograph with a chlorine EDS map. The distribution of chlorine in the sample is strongly correlated with the distribution of copper as seen from the copper EDS map. (d) Backscattered electron image. Regions containing high concentrations of elements with higher Z number appear bright. The image shows that the inner part of the jaw tip is highly mineralized in accordance with the element map of copper. Reproduced with permission from the American Association for the Advancement of Science⁹⁶.

In 2003, Lichtenegger *et al.* found that considerable quantities of zinc occur in the jaws of the marine polychaete worm *Nereis* sp⁹⁷. They showed that the local hardness and stiffness of the jaws correlate with the local zinc concentration, pointing towards an involvement of the zinc in the mechanistics. Zinc was always detected in spatial correlation with chlorine, suggesting the presence of a zinc-chlorine compound. Based on the correlation of the local histidine levels in the protein matrix and the zinc concentration, they hypothesized a direct coordination of zinc and chlorine to the protein. Figure 1.10 (a) shows an optical micrograph of a *Nereis* jaw. The jaw is 5 mm long, hollow at the base and solid at the tip. The tip is visually darker than the base. In Figure 1.10 (b), an x-ray absorption image of the same jaw is shown. Darker regions denote strong absorption. It is obvious that the tip region absorbs more radiation than the base, indicating higher local electron density. Figure 1.10 (c) shows a Zn fluorescence map, with bright colors denoting high fluorescence intensity and thus a higher amount of Zn. All Zn is concentrated in the tip region of the jaw, with no or very low levels of Zn at the base.

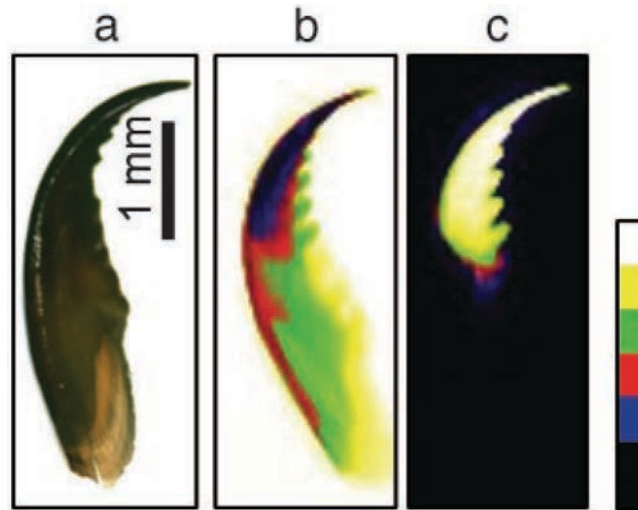


Figure 1.10 Zn distribution in a *Nereis* jaw. (a) Optical micrograph of a jaw. The tip is considerably darker than the base. (b) X-ray absorption image of the same jaw. The tip region appears darker than the rest of the jaw, indicating stronger X-ray absorption. (c) The Zn K α fluorescence image shows Zn being dominantly concentrated in the tip of the jaw. Reproduced with permission from the National Academy of Sciences⁹⁷.

1.3.2 The VPI process

A desire to produce bioinspired new functional materials has stimulated materials scientists to adapt principles similar to the natural ones, and diverse approaches towards this goal have been attempted. However, research to improve the mechanical properties of biomaterials themselves by direct metal incorporation into the inner protein structures has rarely been tried because of the lack of methods that can efficiently infiltrate metals into biomaterials. Our group has demonstrated that metals can be intentionally infiltrated into inner protein structures of biomaterials through multiple pulsed vapor phase infiltration, which is performed with equipment that is conventionally used for atomic layer deposition (ALD)⁹⁸. Considering the ALD concept, an infiltration of metal into polymers cannot be considered as a real ALD process. The reason is that the self-limitation, which is a characteristic of an ALD process, does not apply, but rather a diffusion of the vaporized precursors into the subsurface area and their reaction with buried functionalities. Nevertheless, such an infiltration process, which is called hereafter “*vapor phase infiltration (VPI)*”^{75,88}, still relies on the same technical principles being, the temporal separation of the vaporized precursors and solvent-free operation, qualifying this new approach as an ALD-derived methodology.

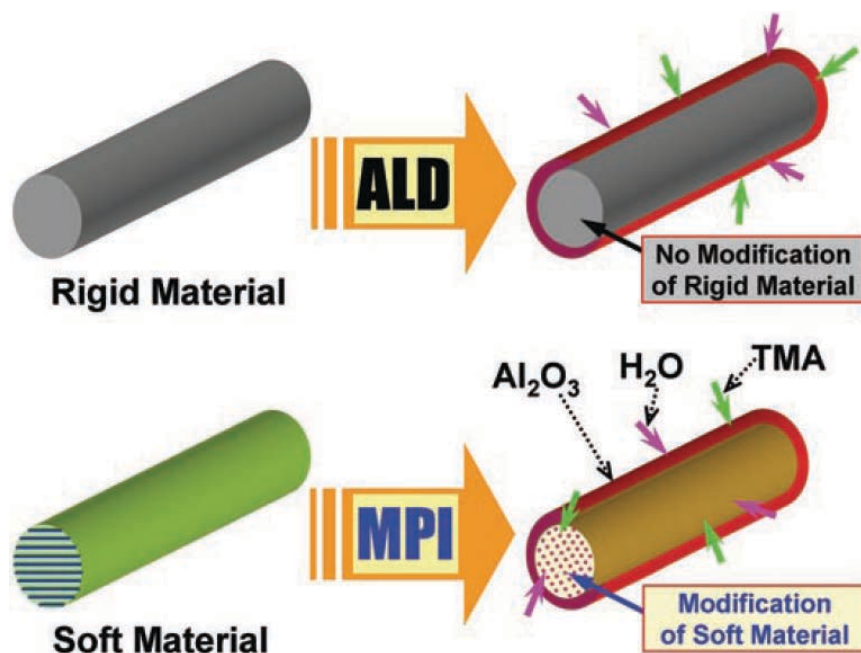


Figure 1.11 A schematic describing the difference between conventional ALD resulting in thin-film deposition (top) and the original infiltration technique named multiple pulsed vapor phase infiltration (MPI). When a dense and solid substrate is exposed to ALD precursors, a thin conformal coating develops at the surface of the material. However, when a soft material is used as substrate, the precursors will diffuse into the sub-surface regions and react with available functional groups. Reproduced with permission from the American Association for the Advancement of Science⁹⁸.

The first intentional use of the vapor phase infiltration process was performed on spider silk with standard precursors and process setup as used in an ALD process. The only difference while processing was the extension of exposure times. The process was named multiple pulsed vapor-phase infiltration (MPI) for distinguishing the typical ALD coating process from this new infiltration process, (Figure 1.11)⁹⁸. Subsequently, several variations of vapor phase infiltration were reported with slight variations in the precursor pulsing strategies, each with a slightly different name, such as, sequential vapor infiltration (SVI)⁹⁹, or sequential infiltration synthesis (SIS)^{100,101}. All of these infiltration processes are inherently the same, using the vapor-phase precursors to penetrate into and modify the subsurface regions of soft materials, but vary mainly in the dosing manner.

1.3.2.1 Nature polymers

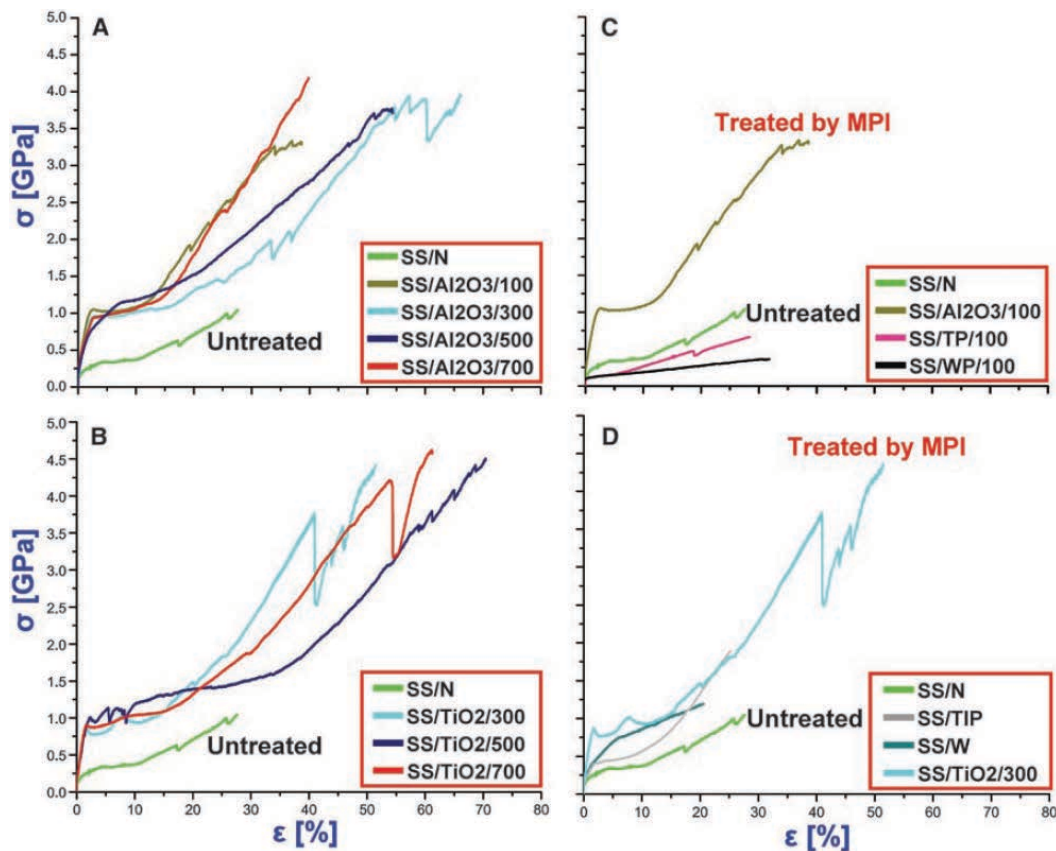


Figure 1.12 Tensile test curves of spider silk infiltrated with TMA/H₂O and TIP/H₂O precursor pairs as compared to untreated control samples and samples treated with individual precursors. (A) and (B) show stress (σ) and strain (ϵ) curves of spider silk infiltrated with TMA/H₂O and TIP/H₂O with various numbers of cycles ranging from 100 to 700. (C) σ - ϵ curves of spider silk infiltrated with the individual precursors, i.e. only TMA (TP), or H₂O (WP), and with both precursors. (D) σ - ϵ curves for spider silk immersed into liquid TIP or H₂O for 10 h, followed by room temperature drying. (TMA-trimethylaluminum, TIP-titanium isopropoxide, and SS/N-native spider silk without any treatment). Reproduced with permission from the American Association for the Advancement of Science⁹⁸.

The initial work illustrating the infiltration mechanism showed significant increase in the mechanical properties of the spider silk, as can be seen in Figure 1.12. Once extended exposure times were used, the vaporized precursors (TMA or TIP) diffused into the bulk of the spider silk. The MPI process was performed with standard precursor pairs, an organometallic or metal-organic precursor and an oxygen source. After the infiltration process, the presence of the infiltrated metals such as titanium (Ti), or aluminum (Al) inside the silk was verified by energy-dispersive x-ray spectroscopy (EDS). The greatly enhanced toughness of the infiltrated silks is, however, not a result of the presence of around 3 wt.% metal (ions) in the

bulk of the protein, but of the chemical interaction between precursors and the substrate. The X-ray diffraction (XRD) characterization and the analysis of the full width at the half maximum (FWHM) of the peaks in the XRD spectra of the spider silk have shown that the reactive metal-containing precursors can decrease the size of the beta-sheets in the protein fibers during the infiltration process. The redistribution of the ratio of amorphous and crystalline protein fractions and the size change of the beta-sheets finally changed the mechanical properties significantly. Solid state nuclear magnetic resonance (NMR) spectra indicated an interaction between aluminum and the protein backbone, crosslinking the strands⁹⁸. It was found that during the infiltration process, hydrogen bonds within the protein were replaced with new covalent bonds between the metals and the protein matrix.

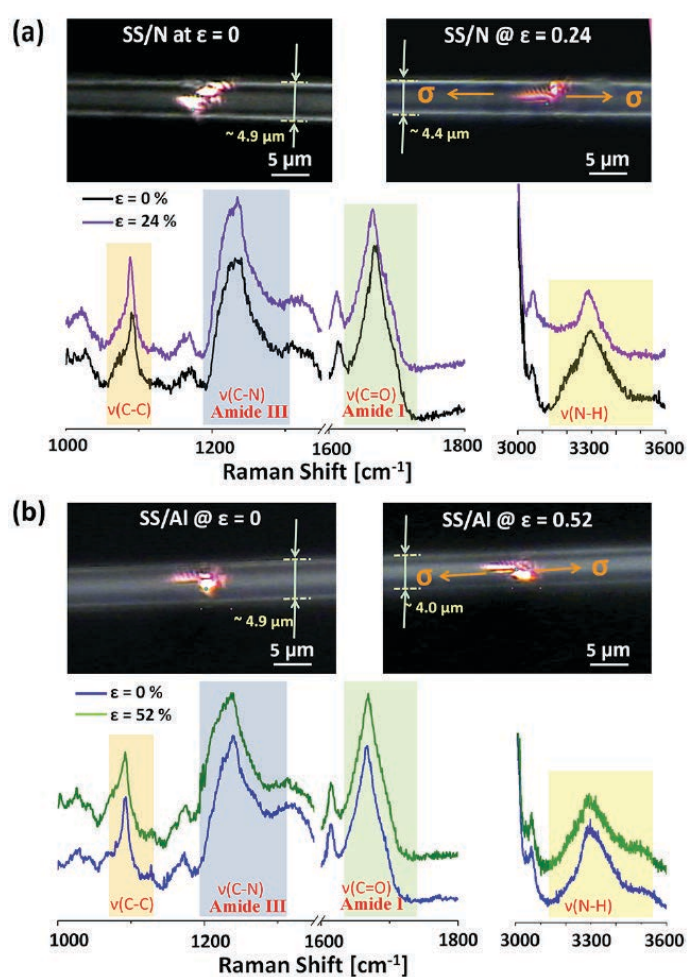


Figure 1.13 Comparison of representative Raman band shifts of (a) the native (SS/N) and (b) Al-infiltrated (SS/Al) spider dragline silk upon mechanical deformation. (Insets) Optical microscope images showing the focused laser beam (633 nm). Reproduced with permission from the American Chemical Society¹⁰².

The influence of the organometallic precursor on the mechanical properties of the spider silk was further investigated in a recent *in situ* Raman spectroscopic study of aluminum infiltrated spider dragline silk^{102,103}, as shown in Figure 1.13. Raman spectroscopy is a well-established technique for evaluating molecular structures of materials and appears most useful for examining molecular deformation mechanisms of the silks during mechanical loading^{104,105}. Upon mechanical deformation of the silk fiber, the covalent bonds within the protein structures are stressed. This leads to an alignment of the molecules along the direction of tension. The deformation of the oriented molecules in both the crystalline and amorphous regions gives rise to a change in bond lengths and bond angles. This induces a change in the corresponding force constants, which can be monitored by measuring the related Raman shifts. Single fibers of both native and Al-infiltrated silks were deformed under controlled strain. In parallel, changes in Raman bands related to amide **I**, amide **III**, $\nu(\text{N-H})$ stretching modes¹⁰⁶, and $\nu(\text{C-C})$ skeletal stretching modes were traced to identify the differences in the molecular deformation behavior between the untreated and treated silk. Figure 1.13 shows the Raman spectra of both silks upon uniaxial deformation in tension. While the native silk showed Raman band shifts to lower wavenumbers (particularly, amide **I**, amide **III**, and $\nu(\text{C-C})$ stretching), the Al-infiltrated silk showed less significant shifts. However, the peaks of amide **III** and $\nu(\text{N-H})$ stretching modes of Al-infiltrated silk exhibited noticeable changes in the peak shapes, which implies that the infiltrated Al atoms are affecting the hydrogen bonds. Presumably the Al atoms form covalent bonds with amino acids during the infiltration of highly reactive TMA and water precursors^{107,108}.

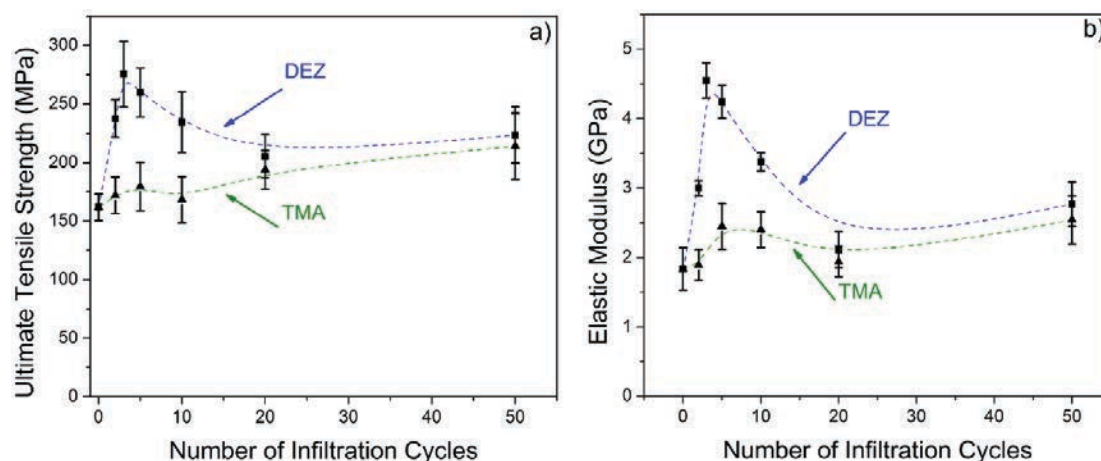


Figure 1.14 Mechanical properties of infiltrated cellulose obtained from uniaxial tensile tests. (a) The tensile strength shows a 2-3 fold increase for cellulose infiltrated with DEZ (diethylzinc) applying 4 infiltration cycles, while cellulose infiltrated with TMA (trimethylaluminum) shows only a slight increase. (b) The elastic modulus of cellulose infiltrated with DEZ applying 4 cycles shows a ~ 2.5 -fold increase, while cellulose infiltrated with TMA shows only a small change. Reproduced with permission from the American Chemical Society¹⁰⁹.

The infiltration process does not necessarily have to operate with two distinct precursors. A further study was conducted with cellulose fibers by applying single precursor (TMA or DEZ) vapor phase infiltration. The mechanical properties of cellulose were monitored as a function of the infiltration cycle number of either TMA or DEZ¹⁰⁹. As seen in Figure 1.14 (a) and (b), under uniaxial tensile testing, changes in the ultimate tensile strength and elastic modulus of the cellulose fibers were witnessed. After 4 cycles of TMA infiltration, the fibers showed a slight increase in both the tensile strength, from 160 MPa to 175 MPa, and elastic modulus, from 1.75 GPa to 2.5 GPa. However, after an analogue process with DEZ, the fibers showed a considerable increase in both the tensile strength (260 MPa) and elastic modulus (4.5 GPa). It is reasonable to assume that DEZ tends to cross-link the cellulose strands in a way that leads to improved mechanical properties.

1.3.2.2 Synthetic polymers

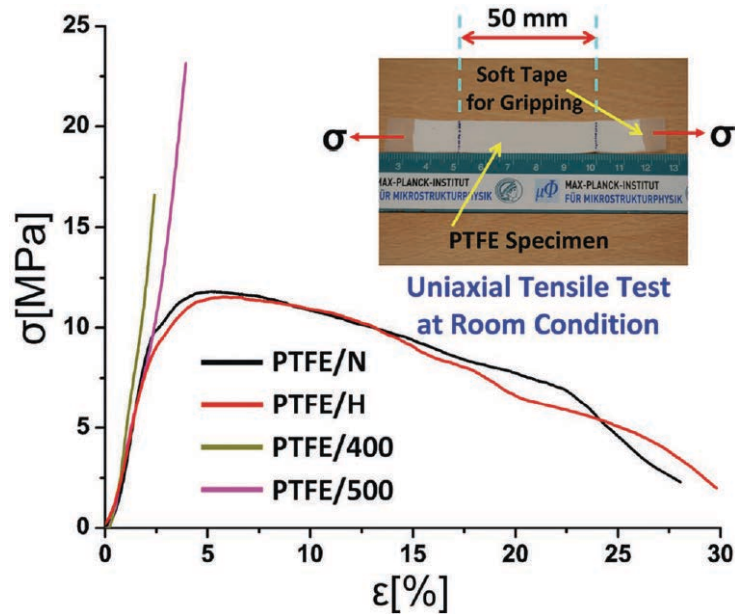


Figure 1.15 Uniaxial tensile behavior (engineering stress, σ , and strain, ε) of native (PTFE/N), heat-treated (PTFE/H), and ZnO infiltrated PTFE (PTFE/400 cycles and PTFE/500 cycles). The inset picture shows a PTFE sample used for the uniaxial tensile test. (PTFE-polytetrafluoroethylene). Reproduced with permission from Wiley-VCH¹¹⁰.

It has been already recognized for a while that incorporation of transition metals into synthetic polymers can lead to unique physical/chemical properties and application in many areas, including mechanics, optics, electronics, etc¹¹¹⁻¹¹⁵. In order to show the applicability of the vapor phase infiltration also to synthetic polymers, Lee *et al.* exposed PTFE (polytetrafluoroethylene) to the precursor pair DEZ/H₂O at a temperature of 70 °C¹¹⁰. It was found that VPI can lead to an incorporation of Zn even into PTFE and chemically react with the polymer even at such mild conditions. Under uniaxial tensile testing, the maximum stress (σ_{\max}) of PTFE has increased from 11.50 MPa (PTFE/H) to 16.64 MPa (PTFE/400) and 23.14 MPa (PTFE/500) (Figure 1.15). A comparison of experimental and theoretically modeled Raman spectra showed that the formation of -Zn-O-Zn- bridging units or -Zn-F groups at both defect sites and polymer chain terminal is likely the reason for the modified mechanical properties.

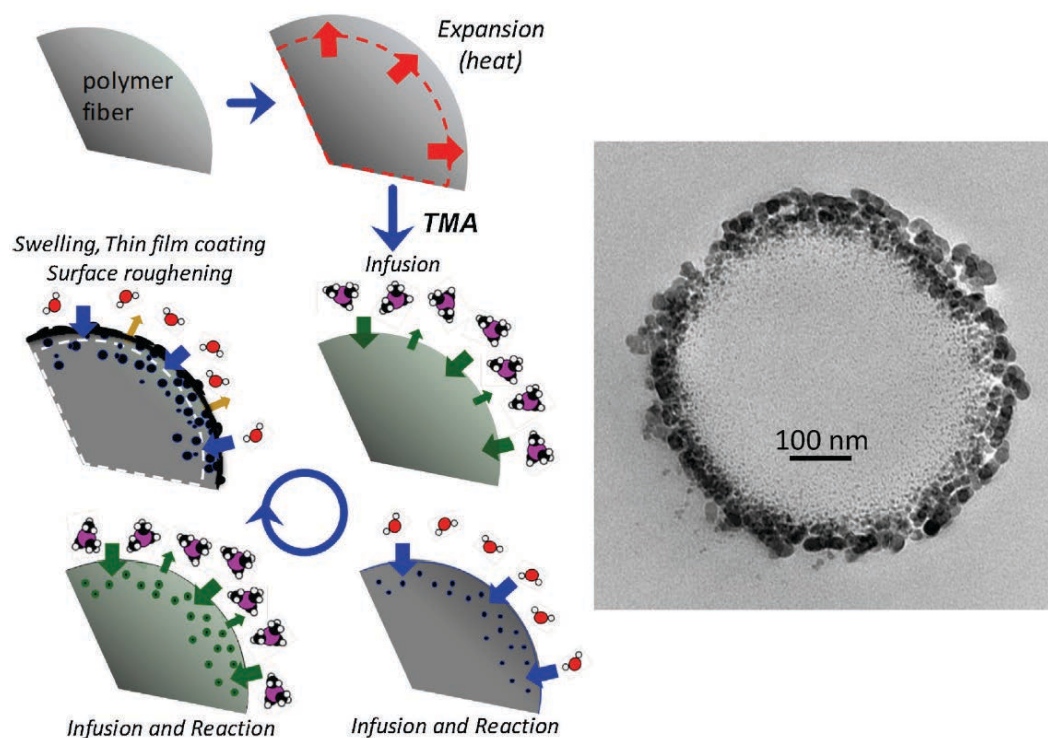


Figure 1.16. Schematic of an Al₂O₃ infiltration process with a polymer without functional groups. The precursors (TMA and H₂O) can be absorbed by the polymer and react in the subsurface area. The TEM image shows a graded polymer/inorganic interface and a rough surface texture in a polypropylene fiber after coating using TMA/H₂O. Reproduced with permission from Elsevier¹¹⁶.

Another example showing that ALD precursors can penetrate synthetic polymeric substrates was shown with the vapor phase infiltration of polypropylene (PP) and the subsurface growth of alumina particles, as seen in Figure 1.16¹¹⁶. Polypropylene lacks reactive groups on its backbone for the nucleation of alumina, therefore a true hybrid material formation is unlikely to occur. At a process temperature of 90 °C, TMA does not readily react on the surface, but diffuses into the polymer instead and becomes trapped in the subsurface region until it becomes hydrolyzed by H₂O. This infiltration process eventually resulted in the formation of nanoparticles, with a size variation as a function of the number of process cycle numbers. Figure 1.16 also shows the TEM image of a PP fiber infiltrated with TMA/H₂O at 90 °C with a nonuniform film structure and rough surface texture after the process.

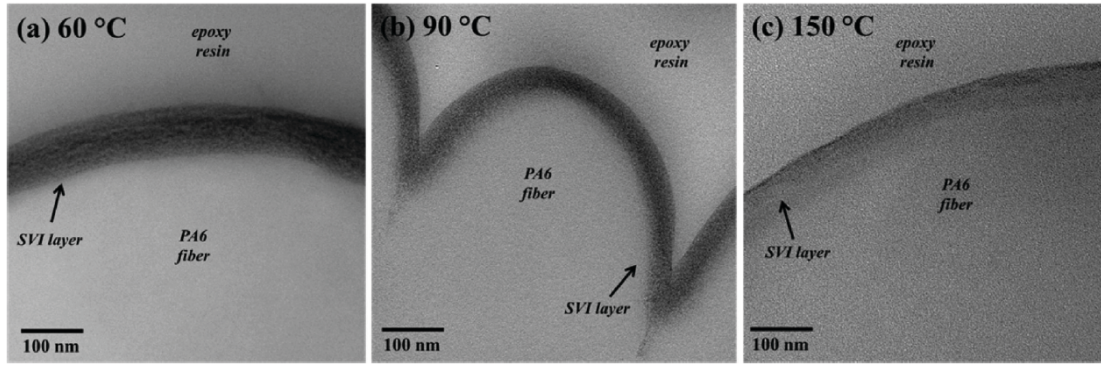


Figure 1.17 High magnification cross-sectional TEM analysis of polyamide 6 (PA6) fibers as a function of the infiltration temperature, (a) 60 °C, (b) 90 °C, and (c) 150 °C. All samples were infiltrated with 60 TMA/H₂O cycles. Reproduced with permission from the American Chemical Society¹¹⁷.

An opposite dependency of the infiltration on the processing temperature was found while applying the infiltration processes of TMA/H₂O to polyamide 6 (PA6) substrates. High magnification cross-sectional TEM images of such samples processed at various temperatures are shown in Figure 1.17¹¹⁷. A more conformal thickness of the subsurface hybrid layer growth is shown at lower process temperatures, with significant nonuniformity evolving at process temperatures of 90 °C and 150 °C. The higher density of the resulting hybrid materials in the near surface region after infiltration at elevated temperatures hinders the diffusion of TMA and H₂O into deeper regions of the substrate. PA6 contains functional groups such as carbonyls and amines, which can chemically interact with TMA, efficiently trapping the precursors near the surface. Additionally, water and further byproducts of the polymerization reaction trapped in the bulk of the polymer may contribute to the barrier formation upon chemical reaction with TMA.

1.4 Objective and Structure of the Thesis

This thesis goes beyond the modification of mechanical properties of polymers. It studies the vapor phase infiltration (VPI) as a pathway for doping conductive polymers. Two routes have been evaluated, the single precursor vapor phase infiltration (Chapter 3 and Chapter 4) process and the infiltration with precursor pairs (Chapter 5), also called “Multiple Pulsed Vapor Phase Infiltration”. As substrates, the conducting polymers, polyaniline (PANI) and poly(3-hexyl)thiophene (P3HT) were used.

Chapter 2 provides an overview of the experimental techniques used for in this research. All characterization tools and equipments involved in this thesis are briefly explained.

Chapter 3 focuses on the single precursor vapor phase infiltration and doping of the emeraldine base of polyaniline (PANI) with SnCl_4 and MoCl_5 . The conductivities of the infiltrated PANI upon application of various cycle numbers and the stability of the infiltrated polymer upon exposure to high temperatures (150 °C) and vacuum environment were studied, and a likely doping mechanism was proposed.

Chapter 4 describes the low temperature single precursor MoCl_5 vapor phase infiltration and doping of poly(3-hexyl)thiophene (95% regioregularity), P3HT. The conductivities of the infiltrated P3HT after various cycle numbers and its long-term stability under ambient conditions were investigated. An appropriate doping mechanism is proposed based on the performed characterization.

Chapter 5 describes the infiltration and doping of PANI (emeraldine base) with the precursor pair DEZ (diethylzinc) and H_2O , referred to as multiple pulsed vapor phase infiltration of PANI. The conductivities of the infiltrated PANI after various infiltration cycle numbers were explored. A doping mechanism is proposed, which is likely to result in a mutually enhancing electronic interaction between two doped species, the ZnO and PANI.

Finally, a summary of the research and future perspectives are given in Chapter 6.

Chapter 2

Experimental Techniques and Methods

This chapter gives an overview of the experimental techniques and methods used in the thesis. All the characterization tools mainly relate to structural, compositional, or electronic characterizations. Specific methods applied in individual parts of the work will be described in the relevant sections.

2.1 X-ray Diffractometer

X-ray diffractometry (XRD) is a technique, which allows to characterize the crystallinity of a sample. In the reflectivity mode it can be used for measuring the thickness of a thin film. In XRD, a monochromatic X-ray beam irradiates the sample at a grazing incident angle θ . In a crystalline arrangement of atoms, the incident beam will be scattered with the deflected waves having constructive interference at specific spots. In agreement with the Bragg's equation¹¹⁸,

$$2d\sin\theta = n\lambda,$$

diffraction will occur. At an angle 2θ with respect to the incident beam, a detector collects the deflected beam. Figure 2.1 (a) shows schematically the beam path upon interaction with the sample. Here, d is the spacing between diffracting planes, θ is the incident angle of the beam, and λ is the wavelength of the beam. The detected reflections are subsequently indexed to obtain the crystalline information in the reciprocal space.

The X-ray reflectivity (XRR) technique is used to measure the thicknesses of a thin film, based on the principle shown in Figure 2.1 (b). According to the Snell Law, the refractive index of all materials is below the unity for X-ray electromagnetic radiation. Therefore, the critical incident angle θ_c for total reflection will depend on the density of the material. If the incident angle θ is equal to θ_c , the incident X-ray will propagate along the sample surface. If the incident angle is below θ_c , total reflection will occur. With incident angles above θ_c , the X-ray will be partly refracted and a reflection will occur at both the thin film bottom and top interfaces. These two reflected waves will interfere with each other, leading to the intensity decreasing as a function of the incident angle. From Snell's Law:

$$\frac{\sin(90 - \theta)}{\sin(90 - \theta')} = \frac{\lambda}{\lambda'} = \frac{n'}{n}$$

and Bragg's law:

$$\begin{aligned} m\lambda &= 2 \frac{d}{\sin\theta'} \cdot \frac{n'}{n} - 2 \frac{d}{\sin\theta'} \cdot \cos\theta' \cdot \cos\theta \\ &= 2d \sin\theta' \cdot \frac{n'}{n} \end{aligned}$$

the thickness of the film can be obtained as follows:

$$d = \frac{m\lambda}{2\sin\theta'} \cdot \frac{n}{n'}$$

The angles θ and θ' are the incident angle and the angle of the refracted beam with respect to the sample surface, λ and λ' are the wavelengths of the incident and refracted beams, n and n' are the refraction indices of air and the thin film, d is the film thickness, and m is the interference order.

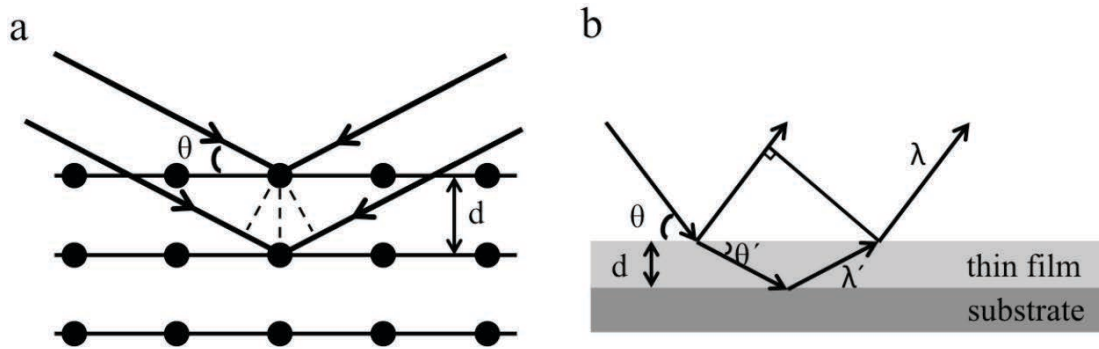


Figure 2.1 Schematics for (a) X-ray diffraction (XRD): the X-ray beam irradiates a crystal at a grazing incident angle θ and is scattered by the atoms in the crystal. When the Bragg's condition is fulfilled, characteristic peaks resulting from diffraction appear in the collected spectrum. (b) X-ray reflectivity (XRR): the X-ray beam irradiates a thin film, part of the beam reflects on the top interface of the thin film, and part of the beam is refracted, reflects at the bottom interface of the thin film and becomes refracted again at the top interface. The two reflected beams interfere with each other. After applying the Snell Law and the Bragg's equation, the thickness of the thin film can be obtained from the measured spectrum.

In this work, XRD measurements of various samples were carried out with the X-ray diffractometer (X'Pert, PANalytical) with a Cu K α ($\lambda = 0.154$ nm) radiation source. During the measurements, the working voltage and current were 45 kV and 40 mA, respectively. The

collected spectra were compared with the standard JCPDS (joint committee on powder diffraction standards) database.

2.2 Fourier Transform Infrared (FTIR) Spectroscopy

Fourier transform infrared spectroscopy (FTIR) is a technique for analyzing absorption or emission of a solid, liquid or gas. It can provide qualitative information about the chemical functional groups contained in a material in a non-destructive way. Upon irradiation of a sample with an electromagnetic wave, specific molecular vibrations in the sample are excited when the molecule absorbs a photon with an energy of $E = h\nu = hc(\nu/c)$, where h is the Planck's constant, c is the velocity of light and ν/c is the wave number. For FTIR spectroscopy, the energy of the irradiation beam is in the infrared region with wave numbers between 200 and 10000 cm^{-1} . For molecular vibrations in organic molecules, usually a smaller width between 400 and 4000 cm^{-1} is used. Once exposed to the beam, the molecule becomes excited to a high vibrational energy state as a result from direct absorption of photons. The energy-specific absorption will result in a peak at the corresponding wavenumber in the recorded spectrum. The detector usually plots the absorbance or % transmittance as a function of the wavenumber.

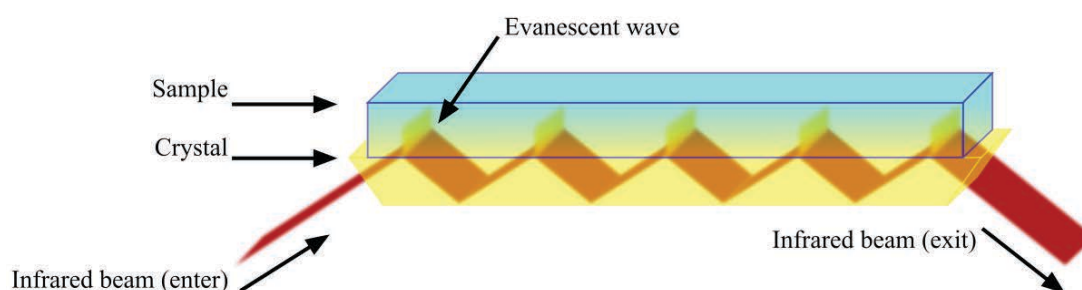


Figure 2.2 A schematic diagram of an attenuated total reflectance (ATR) principle.

The attenuated total reflectance (ATR) is a specific way of measuring FTIR spectra of the near surface region of solids or thin films rather than of their bulk (Figure 2.2)¹¹⁹. ATR typically measures regions of the sample of 1 to 2 micrometers depth. In such a setup, an infrared beam is directed into an ATR crystal (an optical material with a high refractive index) at a certain angle, which allows multiple total internal reflection of the beam inside the crystal. Such total internal reflection occurs when a wave reaches the interface from the side of a material with a high refractive index to the side of a material with a low refractive index at an incident angle above the critical angle. On the surface of an ATR crystal, those reflections

will form an evanescent wave. If at the interface the sample is positioned, the evanescent waves are attenuated or altered after penetrating into and interacting with the sample. The attenuated evanescent wave is passed back to the IR beam, exits the ATR crystal and is finally collected by the detector. The recorded signal contains information about the sample fraction in near vicinity of the ATR crystal.

In this thesis, all FTIR measurements were performed with a Fourier Transform Infrared (FTIR) spectrometer (FT-IR spectrometer Frontier, PerkinElmer) equipped with an ATR setup. All samples were prepared as thin films by drop casting their solutions onto silicon wafers or glass substrates.

2.3 Raman Spectroscopy

Raman spectroscopy is a technique that allows to identify vibrational, rotational and other low frequency modes in a material system¹²⁰. Raman spectroscopy is complementary to FTIR and is commonly used in chemistry to provide a fingerprint by which molecules can be identified. It relies on inelastic scattering (Raman scattering) of monochromatic light, usually emitted by a laser in the visible, near infrared, or near ultraviolet range. For obtaining Raman spectra, the sample is commonly illuminated with a laser beam in visible range. The molecule absorbs photons with frequency ν_1 and becomes excited to a high virtual energy state. Some of the molecules relax back to the initial energy state by emitting photons with the same frequency ν_1 , while others relax to another vibrational energy state by emitting photons with further frequencies ν_i . The photons with frequency ν_i are recorded and stand in relation to the molecular vibrational frequencies.

In this work, Raman spectroscopy was carried out in a Raman microscope (Alpha 300S, WITec), with a light source at a wavelength of 532 nm (100× objective). The Raman spectra were background corrected and obtained by averaging spectra from five different regions of each sample. The collected data were analyzed with the WIT spectra software.

2.4 Electron Microscopy (SEM and TEM)

The resolution of an optical microscope is limited to about 200 nm depending on the wavelength of the used visible light. In order to achieve higher resolutions, further sources of illumination are needed. The electron microscope uses a beam of accelerated electrons as a source of illumination, which allows for investigation of the ultrastructure of a wide range of biological and inorganic specimens including microorganisms, cells, large molecules, metals, and crystals. The electron microscope can span magnifications ranging from thousands to

millions with resolutions ranging from nanometers to Ångstroms. Figure 2.3 schematically shows the main types of interactions between the accelerated electron beam and the sample. Based on the way of collecting electrons by the detector, an electron microscope can be referred to as scanning electron microscope (SEM) or transmission electron microscope (TEM).

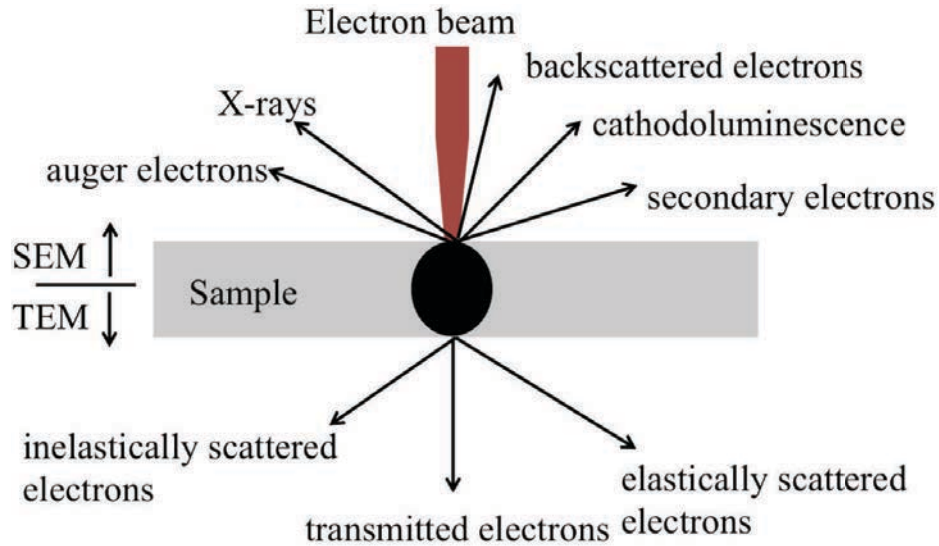


Figure 2.3 Schematic of the main types of interactions between an accelerated electron beam and a sample in an electron microscope.

Scanning electron microscopy (SEM) is one of the most common tools used in nanoscience for inspecting the microstructure of nanomaterials including shape, topography, composition and morphology. It can produce images by probing the specimen with a focused electron beam that is scanned across a rectangular area of the specimen. When the electron beam interacts with the specimen, various mechanisms induce a loss of energy. The lost energy is converted into alternative forms such as heat, emission of low energy secondary electrons, high energy backscattered electrons, light emission or X-ray emission, all of which carry information about the specimen surface. Commonly, the backscattered electrons are detected displaying the topography of the surface of the sample.

For the SEM experiments performed in this thesis, the Quanta TM 250 FEG (FEI) SEM was used. During imaging, the chamber pressure ranged from standard high vacuum conditions ($< 6 \times 10^{-4}$ Pa) to low vacuum conditions (10 - 2600 Pa), and the accelerating voltage ranged from 1kV to 30kV. All investigated samples were prepared as thin films or as powders initially dispersed in a solution and then drop-casted onto silicon wafers or insulating glass substrates. For conventional imaging in the SEM, samples must be electrically

conductive, at least at the surface, and electrically grounded to prevent the accumulation of electrostatic charge. Non-conducting materials are usually coated with an ultrathin coating of electrically conducting material, such as carbon or platinum, deposited on the sample either by low-vacuum sputter coating or by high-vacuum thermal evaporation.

Transmission electron microscopy (TEM), the original form of electron microscopy, uses a high voltage electron beam to illuminate the specimen and enables collecting information from transmitted electrons to create an image. The resolution is typically about an order of magnitude better than that in a typical SEM. From the TEM images, crystalline lattices of materials and even single atoms can be observed, provided good alignment of the instrument is done.

Energy-dispersive X-ray spectroscopy (EDS), is an analytical technique used for the elemental analysis of a sample. To stimulate the emission of characteristic X-rays from a specimen, a high-energy beam of charged particles, such as electrons or protons, is focused on the sample. The beam will excite an electron from an inner shell, ejecting it from the shell while an electron hole will be left behind. This hole will be filled with an electron from an outer shell, and the difference in energy between the outer and the inner shell will be released in form of X-ray irradiation. The number and energy of the X-rays emitted from a specimen are measured by an energy-dispersive spectrometer. As the energies of X-rays are characteristic of the difference in energy between two shells and the atomic structure of the emitting atom, EDS allows precise determination of the elemental composition of a specimen.

In all experiments performed in this thesis, a Helios NanoLab Dual Beam (FEI, NL) was used to examine samples in scanning transmission mode. TEM imaging and EDS analysis were carried out with an FEI Titan microscope operating at 300 kV acceleration voltage in STEM mode and equipped with an EDAX SDD detector.

2.5 Ultraviolet -Visible Spectroscopy

Ultraviolet-Visible Spectroscopy (UV-Vis) refers to absorption spectroscopy or reflectance spectroscopy in the ultraviolet-visible spectral region. The absorption or reflectance in the visible range directly affects the perceived color of the chemicals involved. In this region of the electromagnetic spectrum, atoms and molecules undergo electronic transitions. The absorption spectroscopy characterizes transitions of molecules from the ground state to the excited state¹²¹. The wavelengths of the absorption peaks can be correlated with the types of bonds in a given molecule and are valuable for determining the functional groups contained in a molecule.

For the Uv-vis experiments performed in this thesis, all samples were prepared as thin films initially dispersed in a solution and then drop-casted onto insulating glass substrates. Absorption spectra of the samples were recorded between 250-890 nm using a UV-Vis spectrophotometer (V-630 BIO, JASCO).

2.6 Atomic Force Microscopy (AFM)

Atomic-force microscopy (AFM) is scanning probe microscopy technique, commonly used to characterize the surface structure and morphology of materials. During AFM probing, information about the morphology of a sample is gathered by "feeling" or "touching" the surface with a mechanical probe or tip. Piezoelectric elements facilitate tiny but accurate and precise lateral movements of tip or sample. The cantilever, to which the tip is attached, is vertically deflected during the measurement due to attractive and repulsive forces between the tip and the sample surface. Focusing a laser onto the cantilever and recording the movement of the reflected laser with a photodiode while scanning the sample allows for a visual reconstruction of the sample morphology.

AFM can be used in three distinct modes: contact mode, also called static mode, tapping mode, also called intermittent contact mode, and non-contact mode. Among those the tapping mode is the most frequently used AFM mode when operating in ambient conditions. In tapping mode, the cantilever oscillates up and down near its resonance frequency at a constant amplitude¹²². When the tip comes close to the surface, interactions between the tip and the sample surface cause the oscillation amplitude of the cantilever to change. This change of the amplitude is used as feedback to readjust the distance of the cantilever to the sample with a piezo crystal. Due to the intermittent contact of the tip with the sample surface, negligible damage to the sample is induced.

In this thesis, AFM analysis was performed on P3HT polymer-coated glass slides, employing a 5500 AFM (Keysight, Santa Clara).

2.7 X-ray Photoelectron Spectroscopy (XPS)

X-ray photoelectron spectroscopy (XPS) is a surface-sensitive quantitative spectroscopic technique that is commonly used to analyze elemental compositions, chemical states and electronic states of the elements that are present in a material. In XPS, the sample is irradiated with a beam of X-rays under high vacuum ($P \sim 10^{-8}$ millibar) or ultra high vacuum (UHV; $P < 10^{-9}$ millibar) conditions. The X-ray beam can penetrate into the sample and

interact with the electrons. After absorbing energy from the X-ray beam, the near-surface electrons are excited, leading to an escape from the sample. The kinetic energy and number of the escaped electrons are analyzed by a detector. Because the energy of the used X-ray with particular wavelength is known (for Al K_{α} X-rays, $E_{\text{photon}} = 1486.7$ eV), and because the emitted electrons' kinetic energies are measured, the binding energy of each of the emitted electrons can be determined by using an equation that is based on the equation of Ernest Rutherford:

$$E_{\text{binding}} = E_{\text{photon}} - (E_{\text{kinetic}} + \phi),$$

where E_{binding} is the binding energy (BE) of the electrons, E_{photon} is the energy of the X-ray photons being used, E_{kinetic} is the kinetic energy of the electron as measured by the instrument and ϕ is the work function dependent on both the spectrometer and the material and is normally constant in practice. This equation describes essentially the conservation of energy equation. The work function term ϕ is an adjustable instrumental correction factor that accounts for the few eV of kinetic energy given up by the photoelectron as it becomes absorbed by the instrument's detector. It is a constant that rarely needs to be adjusted in practice. The binding energy of recorded electrons depends on their origin, which allows identifying the specific atoms, neighboring atoms and specific orbitals. A quantitative analysis can be obtained by analyzing the intensity of the recorded photoelectrons. Importantly, XPS is a surface sensitive spectroscopic technique, because only the electrons within an area of several nanometers close to the surface can escape from the sample and be recorded.

XPS experiments in this thesis were conducted using a Phoibos photoelectron spectrometer equipped with an Al K_{α} X-ray source (12 mA, 8.33 kV) as the incident photon radiation. All samples were drop-casted onto silicon substrates. The spectra were standardized using the C 1s peak at 284.6 eV. The base pressure of the UHV chamber was maintained at 10^{-9} - 10^{-10} mbar.

2.8 Assessment of the Electrical Conductivity

Electrical conductivity of a material is a measure of its ability to conduct electric current under certain conditions, such as temperature, pressure, applied current, and so on. From the simple Ohm's law on conductivity ($V=R \times I$; where V is the voltage, I is the current, and R is the resistance), it is obvious that a measurement of R may simply be done by applying a current (I) and measuring a potential (V). Since R depends on geometrical parameters (and therefore is sample dependent) the magnitude usually given is the resistivity (ρ), which is defined as $\rho = R \times (A/l)$, where A is the cross-sectional area of the conductor ($A=$

$a \times d$; a is the width, and d is the thickness of the sample) and l is the distance between the voltage-drop measuring points¹²³. For historical reasons the resistivity is usually measured in Ω cm instead of Ω m. Besides the resistivity, the other magnitude that is usually provided is its inverse, called the conductivity, $\sigma = (1/\rho)$, which is measured in $\Omega^{-1} \text{ cm}^{-1} = \text{S cm}^{-1}$ ($\Omega^{-1} = \text{S} = \text{Siemens}$). This conductivity σ is used in the present thesis. The simplest way to measure electrical conductivity is to send a constant current through two electrical probes, and sense the voltage between the probes. However, the two-probe method acquires the total resistance of the circuit, including the contact resistance, the probe resistance, and the spreading resistances under the probes. This analysis makes an individual assessment of the sample resistance very difficult.

The four point probe method is the most common method to determine electrical conductivity without influence of the above mentioned contributions^{124,125}. This method uses an additional pair of probes to separately sense voltage with a high impedance voltmeter, so that the parasitic resistances mentioned above are negligible since virtually no current flows between the voltage probe pairs. During the conductivity testing processes of thin films, all four probes are positioned on the surface of the film. Figure 2.4 illustrates various four-probe configurations for thin film measurements. As shown in Figure 2.4 (a), collinear four-point probes with equal spacing can be put in contact with the sample surface. If the sample size is larger than the probe spacing and the thickness of the film is less than a half of probe spacing, one can obtain the electrical conductivity σ of the film by¹²⁴

$$\sigma = \ln 2 I/\pi d V,$$

where I is the current, V is the voltage and the d is the thickness of the sample.

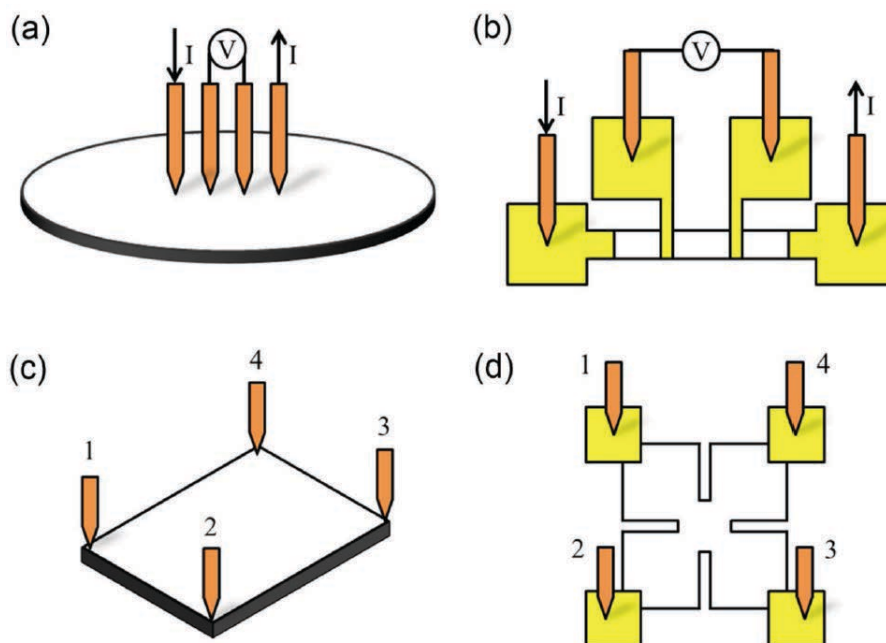


Figure 2.4 Various four point probe configurations for electrical conductivity measurements of thin films: (a) a conventional collinear four-point probe method, (b) a bar-shaped thin film electrode arrangement with four probes, (c) a conventional probing geometry for the van der Pauw (vdP) measurement method, and (d) a clover-leaf vdP geometry. Reproduced with permission from the Begell House Inc., New York¹²⁶.

The van der Pauw (vdP) method is a very useful four-probe approach to determine the electrical conductivity of thin film samples of arbitrary shape¹²⁷. In the vdP method, all probes must be placed on the sample perimeter in a way as shown in Figure 2.4 (c), but not necessarily at the corners. Commonly, a tiny amount of indium is soldered on each probing point to form a good contact between the probe tip and the sample. There is no geometry requirement for the vdP method except that the size of the contacts must be smaller than the size of the sample.

One measurement of electrical conductivity by the vdP method consists of two resistance measurements: R_{ver} (ver: vertical) and R_{hor} (hor: horizontal). For one direction of the current, for example, from contact 1 to 2 in Figure 2.4 (c) and (d), the voltage is measured between 3 and 4, which will yield the first resistance: $R_{12,34} = V_{34}/I_{12}$. To ensure measurement accuracy, the contacts are then switched in terms of applied current and measured voltage to obtain $R_{34,12} = V_{12}/I_{34}$. These two resistances must be identical according to the reciprocity theorem¹²⁷, but the finite size of contacts and different probe positions may cause a discrepancy among them. The results are averaged to reduce the variations in the determination of R_{ver} . The R_{hor} is obtained in a similar way. A current is sent from contact 1 to

the other adjacent contact 4, and the voltage between 2 and 3 is measured to gain $R_{14,23} = V_{23}/I_{14}$. Again, $R_{23,14} = V_{14}/I_{23}$ is also aquired. R_{hor} is then obtained from the average of $R_{14,23}$ and $R_{23,14}$. It is sometimes desirable to reverse the current polarity and /or measure several voltages generated from varying magnitudes of current to eliminate parasitic voltages that may be present during the measurement. Combining these two resistances in the vdP formula, one can calculate the electrical conductivity σ of the sample with the following equation,

$$\frac{1}{\sigma} = \frac{\pi d}{\ln 2} \frac{(R_{ver} + R_{hor})}{2} f\left(\frac{R_{ver}}{R_{hor}}\right)$$

where f is a function of the resistance ratio, d is the film thickness.

In this work, the conductivities of the thin films were measured applying the collinear four-point probe technique with a source measurement unit (Keithley 2611). For each VPI experiment 5 or 6 individual samples were tested for each VPI cycle number. The resulting conductivity σ was calculated according to the formula,

$$\sigma = \ln 2 I / \pi d V.$$

where I is the current, V is the voltage and the d is the thickness of the polymer film.

Chapter 3

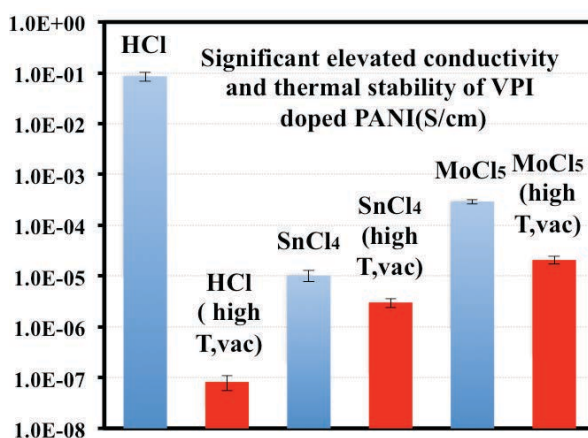
Tuning the Conductivity of Polyaniline (PANI) by VPI Process

This chapter describes a novel single precursor vapor phase infiltration (VPI) process to dope polyaniline (PANI). The infiltration is performed with the metal containing atomic layer deposition precursors MoCl_5 or SnCl_4 . The conductivities are assessed with four-point probe measurements and show significant enhancements of up to 6 orders of magnitude, confirming the efficiency of the VPI process. Furthermore, it is found that the conductivities of PANI/ MoCl_5 and PANI/ SnCl_4 outperform the conductivity of HCl-doped PANI if exposed to elevated temperatures ($150\text{ }^\circ\text{C}$) in vacuum. The chemical changes resulting from the infiltration of PANI are characterized applying FTIR, UV-Vis and Raman spectroscopy. Scanning electron microscopy images show that the morphologies of the samples do not alter after the infiltration process.

This chapter describes the part of the thesis that was published in the journal *Advanced Materials Interfaces* from Wiley-VCH. Graphs, figures and parts of the text of the publication are reused in this thesis with permission of the publisher.

Article:

Tuning the Conductivity of Polyaniline through Doping by Means of Single Precursor Vapor Phase Infiltration. **Weike Wang**, Fan Yang, Chaoqiu Chen, Lianbing Zhang, Yong Qin, and Mato Knez. *Advanced Materials Interfaces* 2017, 4, 201600806.



Comparison of the conductivities of PANI samples after various treatments

3.1. Introduction

Conductive polymers are subject of research since several decades, but their promise as functional material in flexible electronics seriously intensified the research effort on those materials during the past years. Improvement of the conductivity and chemical or thermal stability of a conductive polymer will allow beneficial substitution of inorganic materials in a broad range of electronic devices, including thin-film transistors¹²⁸, light emitting diodes¹²⁹, solar cells¹³⁰, batteries¹³¹, or supercapacitors¹³². With its highly conjugated π delocalized molecular backbone, polyaniline (PANI) belongs to the most prominent organic semiconductors and acts as model system for many further conductive polymers. With view on its application potential, very promising results have been demonstrated in a variety of application fields including sensors, actuators, antistatic coatings, corrosion protection, rechargeable batteries, microwave absorption and electro-optic and electrochromic devices^{25,133}. The level of conductivity of PANI is of crucial importance for most of the applications and depends on the switching between the different states of the polymer, namely, leucoemeraldine, emeraldine, and pernigraniline states, as a response to a chemical or electrical trigger. The conductivity of PANI can be altered by doping and inorganic protonic acids^{134,135}, organic acids^{136,137}, alkali metal salts^{138,139}, Lewis acids^{140,141}, and transition metal salts^{142,143} are the most commonly used dopants. Usually, the doping relies on wet chemistry, which not only introduces impurities into the PANI by inclusion of solvent molecules or additives, but also severely influences the morphology and structure of PANI as such additives impact the polymerization or crystallization of the material. This is very often considered to be a serious drawback for shaping the polymer for various applications. A promising approach to avoid such negative influence from the solvents and obtain better control of the doping process may lie in the vacuum-based processing. In fact, atomic layer deposition (ALD) and related vapor phase infiltration (VPI) strategies take advantage of the mobility of a vaporized chemical to diffuse into and react with polymeric substrates⁸⁸, which may be very beneficial for a solvent-free and controllable doping process.

Incorporation of inorganic materials into polymers often enhances the mechanical, optical, or electronic properties of the resulting composite or hybrid material¹¹⁰⁻¹¹⁴. For example, in our earlier works we have demonstrated that infiltration of metal oxides or metal ions into various (bio)polymers, including spider silk⁹⁸, avian egg collagen¹⁰⁷ and cellulose¹⁰⁹ by means of ALD-derived strategies often enhances their mechanical properties. In the present work, we demonstrate that a similar infiltration process can also be used for doping PANI. The strategy further allows for controlling the level of conductivity of the polymer through the number of infiltration cycles applied. After doping with metal chlorides, the

doped PANI shows exceptional conductivity values, particularly at elevated temperatures, indicating a significant difference in the physics and chemistry of the material in comparison to PANI doped in a traditional way. On the example of two different ALD precursors, MoCl₅ and SnCl₄, we demonstrate that the conductivities of the resulting PANI/MoCl₅ and PANI/SnCl₄ are superior to those of PANI doped with 1M HCl after exposure to elevated temperatures (150 °C). This method may serve as complementary route for stabilizing conductive PANI for high-temperature applications while avoiding the use of solvents and making purification steps obsolete.

3.2. Experimental Section

3.2.1 Preparation the Polyaniline (PANI) nanofibers Thin Film

The synthesis of PANI nanofibers was carried out by a rapid mixing polymerization as reported in literature¹³⁵. All chemicals were analytical grade and were used as received. Typically, an aqueous solution of aniline (3.2 mmol) in HCl (1 M, 10 mL) and a solution of ammonium peroxydisulfate (0.8 mmol) in HCl (1 M, 10 mL) were prepared. The two solutions were mixed at room temperature and rapid and immediate shaking ensured efficient mixing. After 12 h polymerization time, the resulting HCl (1 M) doped PANI was collected by filtration and washed several times with HCl (1 M) until the filtrate became colorless. At last, it was dried in vacuum at 50 °C. De-doped PANI was obtained upon treatment of the PANI/1M HCl with aqueous ammonium hydroxide (0.1 M) for 1 h and subsequent washing with deionized water until the filtrate became pH-neutral, and finally dried in vacuum at 60 °C. Glass substrates (1.3×1.3 cm²) were cleaned in sequence with acetone, deionized water (DI), and isopropanol, and subsequently dried in an oven overnight. PANI and PANI/1M HCl films were coated (200 μL) on the glass substrates and the samples were dried in an oven at 60 °C for 12 h. In advance of the infiltration experiments, the de-doped PANI films were stored overnight at 120 °C.

3.2.2 Vapor Phase Infiltration Process of PANI Thin Film

Vapor-phase infiltration was performed using a homemade atomic layer deposition tool. De-doped PANI films on glass substrates were exposed to vapors of SnCl₄ (Sigma, 98%) or MoCl₅ (Sigma, 95%) in a pulse-exposure-purge sequence with varied numbers of repetition cycles. One cycle of the process consisted of following settings: the precursors were pulsed

into the reaction chamber for 0.1 s (SnCl_4) or 5 s (MoCl_5) and exposure of the substrates to the vapors in the reaction chamber was allowed for 120 s. The exposure was followed by a 60 s purge step. The cycle was repeated with the number of cycles varying between 10 and 200. As carrier and purging gas N_2 (99.99%) was used. The reaction temperature was 150 °C, and the base pressure of the reactor was ~ 50 mTorr. Since at room temperature MoCl_5 is solid, heating of that precursor to 85 °C was required to obtain reasonable vapor pressure.

3.2.3 Characterization

Infrared spectra of the samples were recorded between 700 and 1800 cm^{-1} with a FTIR Spectrometer (Frontier; PerkinElmer).

The morphology of the samples was characterized by scanning electron microscopy (SEM, Quanta 250 FEG; FEI) and the composition analysis was done by energy-dispersive X-ray spectroscopy (EDS). Thickness measurements were carried out on a cleaved cross-section of the sample by FEG-SEM.

Raman spectra at 532 nm excitation wavelength were collected with a Raman microscope (Alpha 300S, WITec). The laser power was kept below 0.7 mW to avoid sample degradation.

Absorption spectra of the samples were recorded between 250-880 nm using a UV-vis spectrophotometer (V-630 BIO, JASCO).

The conductivities of the films were measured applying a four-point probe technique with a source measurement unit (Keithley 2611). For each experiment four or five individual samples were tested for each VPI process cycle number. The resulting conductivity, was calculated according to the formula,

$$\sigma = \ln 2(I / \pi dV)$$

where I is the current, V is the voltage and d is the film thickness.

3.3 Results and Discussion

3.3.1 Assessment of the electrical conductivity

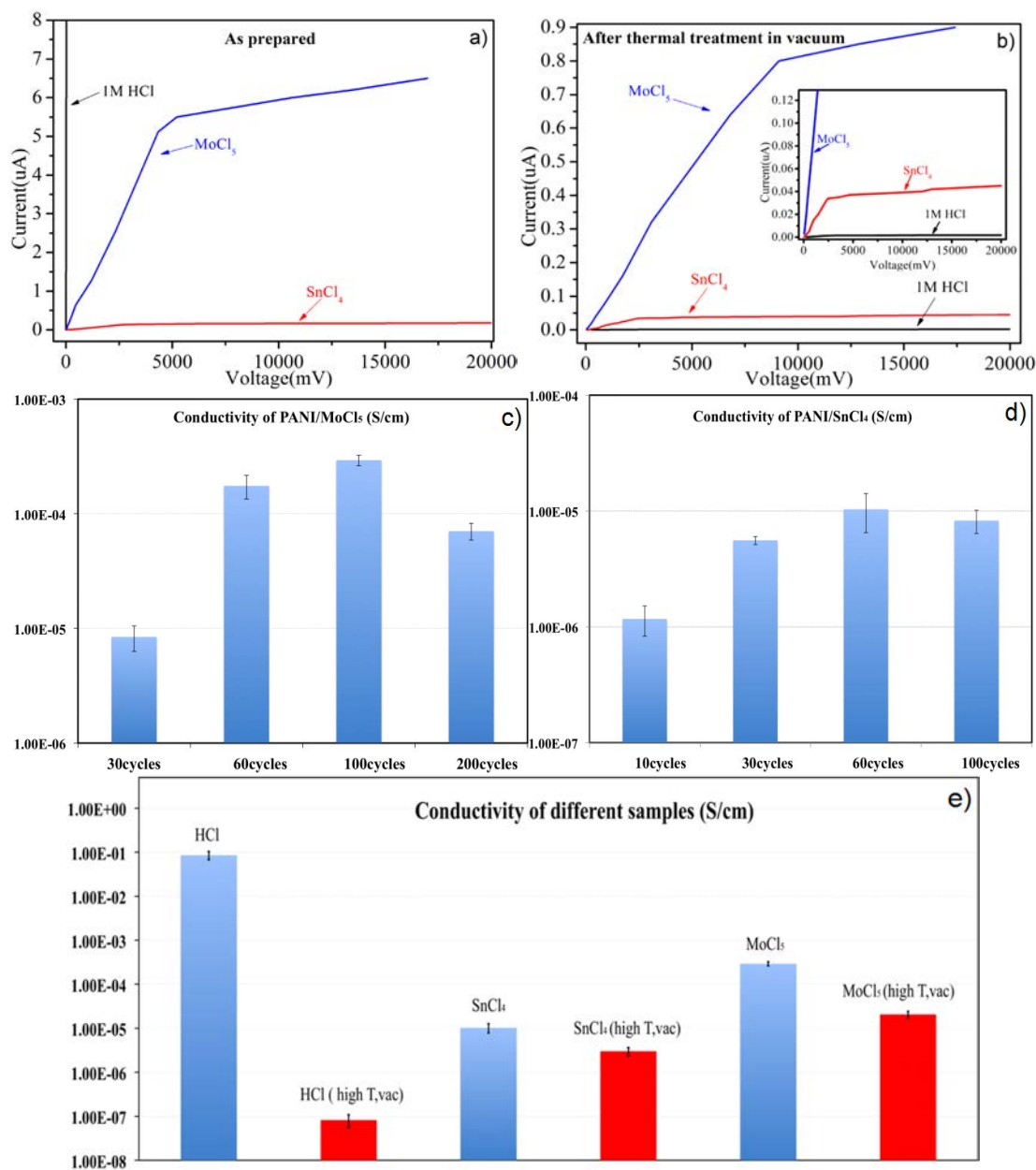


Figure 3.1 *I-V* plots of (a) PANI/1M HCl, PANI/MoCl₅ (100 cycles) and PANI/SnCl₄ (60 cycles) as prepared and (b) PANI/1M HCl, PANI/MoCl₅ (100 cycles) and PANI/SnCl₄ (60 cycles) after storage at 150°C in vacuum for 100 min. The inset shows the low current range area of Figure 1b. Conductivities of (c) MoCl₅ and (d) SnCl₄ as a function of the number of infiltration cycles (measured at room temperature). (e) Conductivity comparison of PANI/1M HCl, PANI/SnCl₄ (60 cycles) and PANI/MoCl₅ (100 cycles) as prepared, and after storage at 150 °C in vacuum for 100 min.

We infiltrated PANI with MoCl_5 and SnCl_4 applying vapor phase infiltration. The process itself is derived from the ALD process, but instead of sequentially exposing the substrate to vapors of two precursors in order to grow a thin film, here we exposed the substrate to the vapor of only one precursor and allowed sufficient time for the precursor to diffuse into subsurface areas of the substrate. After infiltration, we measured the electrical characteristics of the samples. Figure 3.1 (a), (b) show the room temperature I - V characteristics of the fabricated PANI samples. The thicknesses of the samples were comparable and in the range of 7-10 μm . The plots of PANI/1M HCl (black curves) are linear, indicating ohmic behavior over the whole measurement range. Those samples reflect the electrical characteristics of PANI doped with 1M HCl in a traditional way and serve as reference samples for our new infiltration based doping strategy.

Untreated PANI thin films were measured for reference and showed negligible conductivity ($\leq 1 \times 10^{-10}$ S/cm). The plots of the infiltrated samples PANI/ MoCl_5 (blue curve) and PANI/ SnCl_4 (red curve) show linear, ohmic behavior in the initial voltage range before changing the slope with the voltage increasing. Two important observations can be made from those two graphs; i) the possibility of using vapor infiltration strategies for doping of PANI is in the first instance an exciting result, which enables many new top-down approaches towards conductive polymers, and ii) thermal treatment of the doped polymers in vacuum has a much lower impact on the conductivity of the metal chloride-doped PANI than on the HCl-doped PANI, indicating a chemical stabilization of the doped polymer. For the forthcoming discussion, we used values for the electrical conductivities of the samples as calculated from the initial slopes of the I - V plots.

The dramatic enhancement of the conductivity of the PANI films upon infiltrating MoCl_5 or SnCl_4 stands in correlation with the number of infiltration cycles as can be seen in Figure 3.1 (c), (d). Namely, the conductivities of PANI/ MoCl_5 reach 8.43×10^{-6} , 1.75×10^{-4} , 2.93×10^{-4} and 9.8×10^{-5} S/cm after 30, 60, 100, and 200 cycles, respectively, with the highest conductivity being obtained after 100 infiltration cycles. Similarly, the PANI/ SnCl_4 films showed conductivities of 1.17×10^{-6} , 5.58×10^{-6} , 1.03×10^{-5} , and 8.26×10^{-6} S/cm after 10, 30, 60 and 100 cycles, respectively, and the highest conductivity was observed after 60 cycles. Doping with 1M HCl results in values of 8.23×10^{-2} S/cm, which is clearly better performing. However, this applies to room temperature handling only. Figure 3.1 (e) shows that after exposure of the samples to the same elevated temperature, and vacuum environment for 100 min the conductivities of PANI/ MoCl_5 (100 cycles, 2.07×10^{-5} S/cm) and PANI/ SnCl_4 (60 cycles, 3×10^{-6} S/cm) clearly outperform the conductivity of PANI/1M HCl (8.19×10^{-8} S/cm). Furthermore, after heating the prepared samples at 150 °C in N_2 at ambient pressure for 100 min, we observed that the conductivity of PANI/1M HCl decreased by nearly 3 orders of magnitude, from 8.23×10^{-2} S/cm to 1.06×10^{-4} S/cm, while the conductivities of the metal

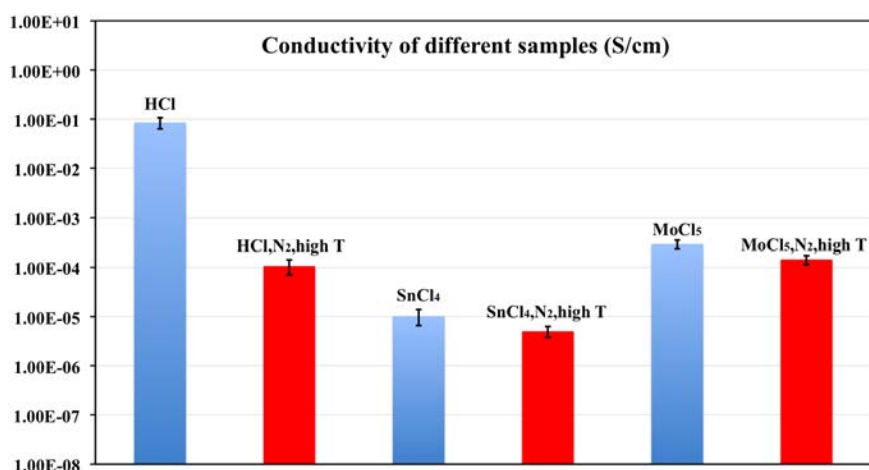


Figure 3.2. Comparison of conductivities of PANI/1M HCl, PANI/SnCl₄ (60 cycles) and PANI/MoCl₅ (100 cycles) as prepared, and after storage at 150 °C in N₂ environment at ambient pressure for 100 min.

chloride infiltrated samples decreased by a much lower extent, namely from 1.03×10^{-5} S/cm to 5.05×10^{-6} S/cm in the case of PANI/SnCl₄ and from 2.93×10^{-4} S/cm to 1.45×10^{-4} S/cm in the case of PANI/MoCl₅, as shown in Figure 3.2.

3.3.2 FTIR Spectroscopy

The analysis of the various samples by FT-IR (Figure 3.3) shows that the HCl-doped or metal chloride-infiltrated samples drastically differ in their chemistry. Doping with 1M HCl (red spectrum in Figure 3.3 (a)) is severely modifying the signature of PANI (black) before exposure to vacuum and elevated temperatures, but closely resembles the reference spectrum after the thermal and vacuum treatment (Figure 3.3 (b)). This indicates that the thermal and vacuum treatment revert the chemical changes that were induced upon doping. The emeraldine base form of PANI is initially protonated with HCl to form the emeraldine salt, which is stabilized with Cl⁻ ions. Elevated temperatures and vacuum reverse this process and deprotonate the salt to form volatile HCl and the emeraldine base. This results in a loss of conductivity. The spectra of the infiltrated samples on the other hand show a somewhat different behavior. In contrast to the HCl-doped sample, they remain similar to the control sample after doping and only very minor changes are observed upon post-treatment. From the overview in Table 3.1, one can see that the peak at 1167 cm⁻¹ in the control sample (in plane C-H bending) has significantly red-shifted to 1105 cm⁻¹ in PANI/1M HCl, while the red-shift in PANI/SnCl₄ and PANI/MoCl₅ is less significant. This peak is considered as the electronic-like band¹⁴⁴, a measure for the degree of delocalization of electrons in the PANI

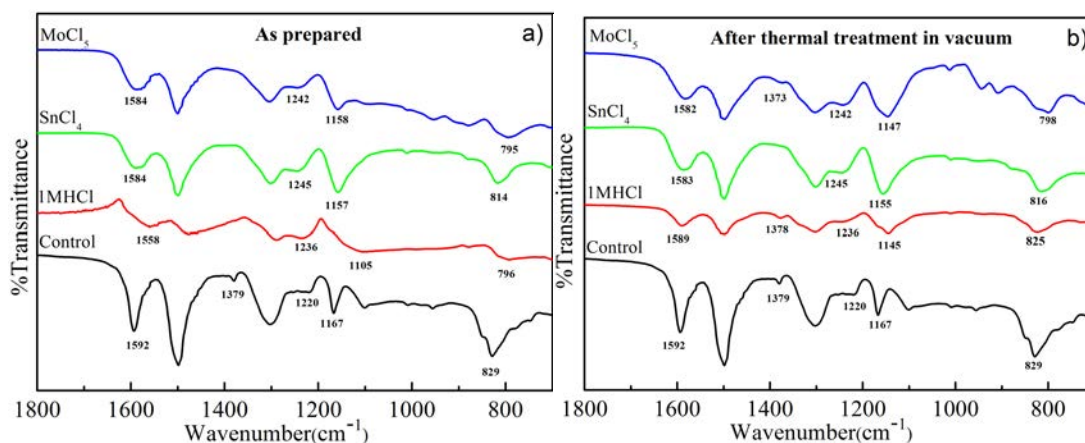


Figure 3.3 FT-IR spectra of undoped PANI (Control), PANI/1M HCl, PANI/SnCl₄ (60 cycles) and PANI/MoCl₅ (100 cycles), before (a) and after (b) treatment at 150 °C in vacuum environment for 100 min.

chains, and thus it is characteristic for its conductivity. The peak at 1592 cm⁻¹ in PANI is assigned to the quinoid C=C stretching vibration and is a signature of the conversion of quinoid rings to benzenoid rings¹⁴⁵. Similar to above, this peak red-shifted more significantly for the 1M HCl doped sample than for the metal chloride doped ones. The peak at 829 cm⁻¹, (out plane C-H deformation of 1,4-disubstituted aromatic rings) red-shifted similarly strong for the 1M HCl and the MoCl₅ sample and less for the SnCl₄ sample. The peak at 1220 cm⁻¹, associated to the benzenoid C-N stretching vibration, showed a more pronounced shift with both metal chlorides than with HCl. Those observations indicate that HCl is efficiently protonating the polymer chain and converting quinoid rings to benzenoid rings. The chemistry will be different for the metal chloride doped polymer. Given that the process occurs in vacuum and without solvents, no protons are available for protonation, but rather an oxidative doping by a complexation reaction can be assumed. The bulkier molecules will result in a lower doping efficiency due to steric hindrance, which is indicated by the lower shift of the peaks associated to the quinoid stretching modes in comparison to the HCl doped ones. The main difference between the two metal chloride doped polymer samples is seen in the shift of the out plane C-H deformation signals. While HCl and MoCl₅ doped PANI show similar shifts, SnCl₄ doped PANI is much closer to the undoped sample, which indicates a less pronounced alteration of the electronic structure of the aromatic sections of the polymer backbone and may be indicative of the measured lower conductivity of the SnCl₄ doped PANI. However, in spite of the lower conductivity than HCl doped PANI at ambient temperatures, the metal chloride doped PANI outperforms the acid counterpart in terms of stability. As can be seen in Figure 3.3 (b), after heating at 150 °C in vacuum for 100 min, most of the peaks in the PANI/1M HCl spectrum have largely recovered to closely resemble

the control sample. On the other hand, the FT-IR spectra of PANI/SnCl₄ and PANI/MoCl₅ show only negligible changes.

Table 3.1 Overview of the most characteristic peaks in the FT-IR spectra in the 1800-700cm⁻¹ region of PANI and PANI doped with 1M HCl, SnCl₄ and MoCl₅ measured before and after thermal treatment (150 °C) in vacuum for 100 min.

	PANI	PANI/1M HCl	PANI/SnCl ₄	PANI/MoCl ₅
In plane C-H bending	1167 cm ⁻¹	As prepared 1105 cm ⁻¹	1157 cm ⁻¹	1158 cm ⁻¹
C=C stretching (quinoid)	1592 cm ⁻¹	1558 cm ⁻¹	1584 cm ⁻¹	1584 cm ⁻¹
Out plane C-H bending	829 cm ⁻¹	796 cm ⁻¹	814 cm ⁻¹	795 cm ⁻¹
C-N stretching	1220 cm ⁻¹	1236 cm ⁻¹	1245 cm ⁻¹	1242 cm ⁻¹
		After thermal treatment in vacuum		
In plane C-H bending	1167 cm ⁻¹	1145 cm ⁻¹	1155 cm ⁻¹	1147 cm ⁻¹
C=C stretching (quinoid)	1592 cm ⁻¹	1589 cm ⁻¹	1583 cm ⁻¹	1582 cm ⁻¹
Out plane C-H bending	829 cm ⁻¹	825 cm ⁻¹	816 cm ⁻¹	798 cm ⁻¹
C-N stretching	1220 cm ⁻¹	1236 cm ⁻¹	1245 cm ⁻¹	1242 cm ⁻¹

3.3.3 Raman Spectroscopy

For gaining deeper insight into the material, the prepared samples were further characterized by Raman spectroscopy. Figure 3.4 shows the 532 nm laser-excited Raman spectra of PANI, PANI/1M HCl, PANI/SnCl₄ and PANI/MoCl₅ coated on glass substrates. The laser power was in all cases kept below 0.7 mW at the samples, and the integration times were controlled below 30s for each of the samples, aiming at avoiding structural change which may be caused by extended and strong photo excitation^{146,147}.

Table 3.2 shows that the band at 1592 cm⁻¹ (C=C stretching of quinoid units) in the PANI reference shifted to higher wavenumbers after doping with either of the three chlorides. The further bands observed at 1336 cm⁻¹, 1345 cm⁻¹ and 1350 cm⁻¹ are characteristic of all doped samples. Those are assigned to the radical cation (C-N⁺ stretching)^{146,147} and are a result of the protonation of PANI with HCl or the oxidation of PANI after complexation with SnCl₄ or MoCl₅. Those peaks are not observable in the spectrum of PANI and are only expected when quinoid rings become converted to benzenoid rings. The coordinative

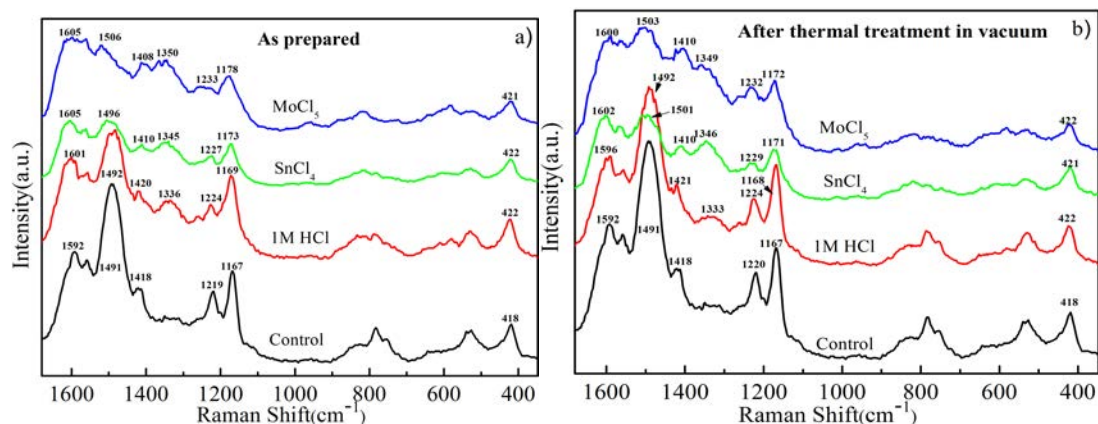


Figure 3.4 Raman spectra of PANI showing the 1680-350 cm^{-1} region (a) Control, PANI/1M HCl, PANI/SnCl₄ (60 cycles) and PANI/MoCl₅ (100 cycles), (b) Control, PANI/1M HCl, PANI/SnCl₄ (60 cycles) and PANI/MoCl₅ (100 cycles) after thermal treatment at 150 °C, in a vacuum environment for 100 min.

interaction of the polymer backbone with the SnCl₄ or MoCl₅ must lower the electron density on the N atoms, and thus a partially positive charge is imposed on the N atoms. A further obvious change relates to the 1491 cm^{-1} band in PANI, which is assigned to the C=N stretching of the quinoid units, which is significantly shifting in PANI/SnCl₄ (1496 cm^{-1}) and PANI/MoCl₅ (1506 cm^{-1}), indicative of a decrease of the amount of quinoid units in the PANI chain. The 1219 cm^{-1} band of the benzenoid C-N stretching in PANI also shifted to higher values with all three chlorides. Additionally, the 1418 cm^{-1} band of the quinoid C-C stretching in PANI shifted to a higher wavenumber in PANI/1M HCl (1420 cm^{-1}), but to a lower wavenumber in PANI/SnCl₄ (1410 cm^{-1}) and in PANI/MoCl₅ (1408 cm^{-1}). The origin of this latter mentioned change is not clear to us at the present. Additionally, a blue shift of the 1167 cm^{-1} band in PANI after all three doping approaches should be noted, which is assigned to the in plane C-H bending of quinoid units¹⁴⁸. After heating the samples at 150 °C for 100 min in vacuum, the most pronounced change in the PANI/1M HCl spectrum is the recovery of the intensity of the peak at 1492 cm^{-1} . Generally, the spectrum of the HCl-doped thermally treated PANI resembles closely the spectrum of the control sample as can be seen in Figure 3.4 (b). Again, this indicates a recovery of most of the quinoid parts of the molecule, induced by deprotonation of the imine and evaporation of HCl. On the other hand, the Raman spectra of PANI/SnCl₄ and PANI/MoCl₅ show only very minor changes upon thermal treatment in vacuum. The more pronounced shifts of Raman peaks in PANI/MoCl₅ and PANI/SnCl₄ compared to PANI/1M HCl demonstrate that instead of an acid doping possibly complexation reactions between Sn or Mo and N atoms play a more significant role in the evolution of conductive PANI upon vapor phase infiltration.

Table 3.2 Overview of the most characteristic peaks in the Raman spectra in the 1680-350 cm^{-1} region of PANI and PANI doped with 1M HCl, SnCl_4 and MoCl_5 measured before and after thermal treatment (150 °C) in vacuum for 100 min.

	PANI	PANI/1M HCl	PANI/ SnCl_4	PANI/ MoCl_5
		As prepared		
C=C stretching (quinoid)	1592 cm^{-1}	1601 cm^{-1}	1605 cm^{-1}	1605 cm^{-1}
C-N ⁺ •stretching	--	1336 cm^{-1}	1345 cm^{-1}	1350 cm^{-1}
C=N stretching (quinoid)	1491 cm^{-1}	1492 cm^{-1}	1496 cm^{-1}	1506 cm^{-1}
C-C stretching (quinoid)	1418 cm^{-1}	1420 cm^{-1}	1410 cm^{-1}	1408 cm^{-1}
C-N stretching (benzenoid)	1219 cm^{-1}	1224 cm^{-1}	1227 cm^{-1}	1233 cm^{-1}
In plane C-H bending (quinoid)	1167 cm^{-1}	1169 cm^{-1}	1173 cm^{-1}	1178 cm^{-1}
		After thermal treatment in vacuum		
C=C stretching (quinoid)	1592 cm^{-1}	1596 cm^{-1}	1602 cm^{-1}	1600 cm^{-1}
C-N ⁺ •stretching	--	1333 cm^{-1}	1346 cm^{-1}	1349 cm^{-1}
C=N stretching (quinoid)	1491 cm^{-1}	1492 cm^{-1}	1501 cm^{-1}	1503 cm^{-1}
C-C stretching (quinoid)	1418 cm^{-1}	1421 cm^{-1}	1410 cm^{-1}	1410 cm^{-1}
C-N stretching (benzenoid)	1220 cm^{-1}	1224 cm^{-1}	1229 cm^{-1}	1232 cm^{-1}
In plane C-H bending (quinoid)	1167 cm^{-1}	1168 cm^{-1}	1171 cm^{-1}	1172 cm^{-1}

3.3.4 SEM and EDS

The morphologies of the samples were examined by scanning electron microscopy (SEM) and elemental analysis was done by energy-dispersive X-ray spectroscopy (EDS). Figures 3.5 (a) to (c) show SEM images of thin films of PANI nanofibers, PANI/ MoCl_5 (100 cycles) nanofibers, and PANI/ SnCl_4 (60 cycles) nanofibers, which were deposited on the glass wafers. The vapor phase infiltration process did not alter the morphology of the PANI, thus the process can indeed be used for top-down infiltration after a desired morphology of PANI has been obtained. The infiltration process is based on the exposure sequences of the PANI substrate to the vapors of metal chlorides, which stands in contrast to the traditional coating procedure by ALD, where a counter precursor is used to fabricate a thin layer of a metal oxide. Figures 3.5 (d) to (f) show EDS spectra of PANI, PANI/ MoCl_5 , and PANI/ SnCl_4 , upon thermal treatment at 150 °C in vacuum for 100 min. Peaks stemming from N, Cl, and Mo or Sn can be clearly observed, which confirms that the infiltrated metal chlorides are trapped within the structure and remain there even upon treatment in a harsher environment. Quantitative characterization revealed that after heating in vacuum, the dopant concentration

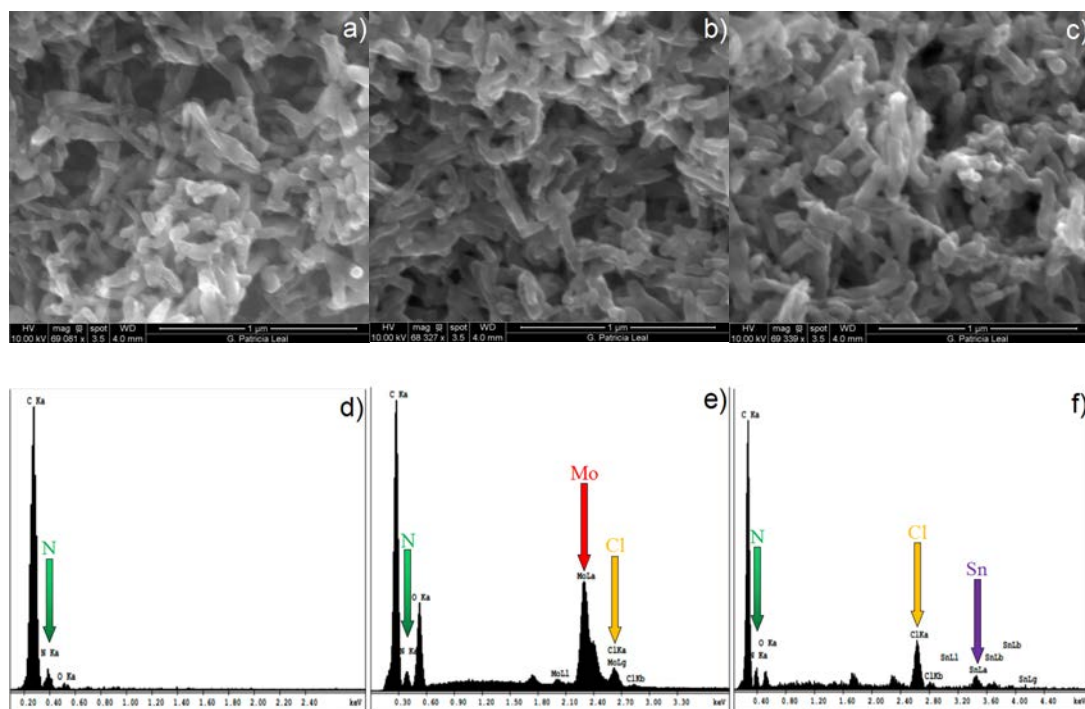


Figure 3.5 SEM images of (a) PANI nanofiber, (b) PANI/MoCl₅ (100 cycles) nanofiber thin film, and (c) PANI/SnCl₄ (60 cycles) nanofiber thin film; EDS spectra of (d) PANI, (e) PANI/MoCl₅, (f) PANI/SnCl₄, after thermal treatment at 150 °C in vacuum for 100 min.

reduced seriously from 13.39 wt% to 1.78 wt% in the case of HCl doped PANI, while the concentration decrease in the metal chloride infiltrated samples was significantly lower, namely from 22.87 wt% to 20.42 wt% in the case of SnCl₄, and from 26.37 wt% to 24.95 wt% in the case of MoCl₅. The significantly lower change in concentration as observed from the metal chlorides doped samples indicates a tight interaction of the precursors with the backbone of the polymer and stabilization of the dopant in a chemical way, presumably through complexation with the nitrogen of the polymer.

3.3.5 Potential Reaction Schemes

Considering the spectroscopic data presented above and publications that reported on various doping strategies of PANI with Lewis acids^{140,141,149} and transition metal salts^{142,143}, we propose a reaction scheme as depicted in Figure 3.6. The initial structure of the emeraldine base of PANI contains both amine (-NH) units and imine (=N) units, which act as functional groups for binding MoCl₅ or SnCl₄. From the Raman spectra we see that the C-N⁺ stretching signals are very pronounced, the benzenoid C-N stretching signals shift significantly and the peak intensity of the quinoid C=N stretching signals significantly decrease after the infiltration process. This indicates that the insertion of MoCl₅ and SnCl₄

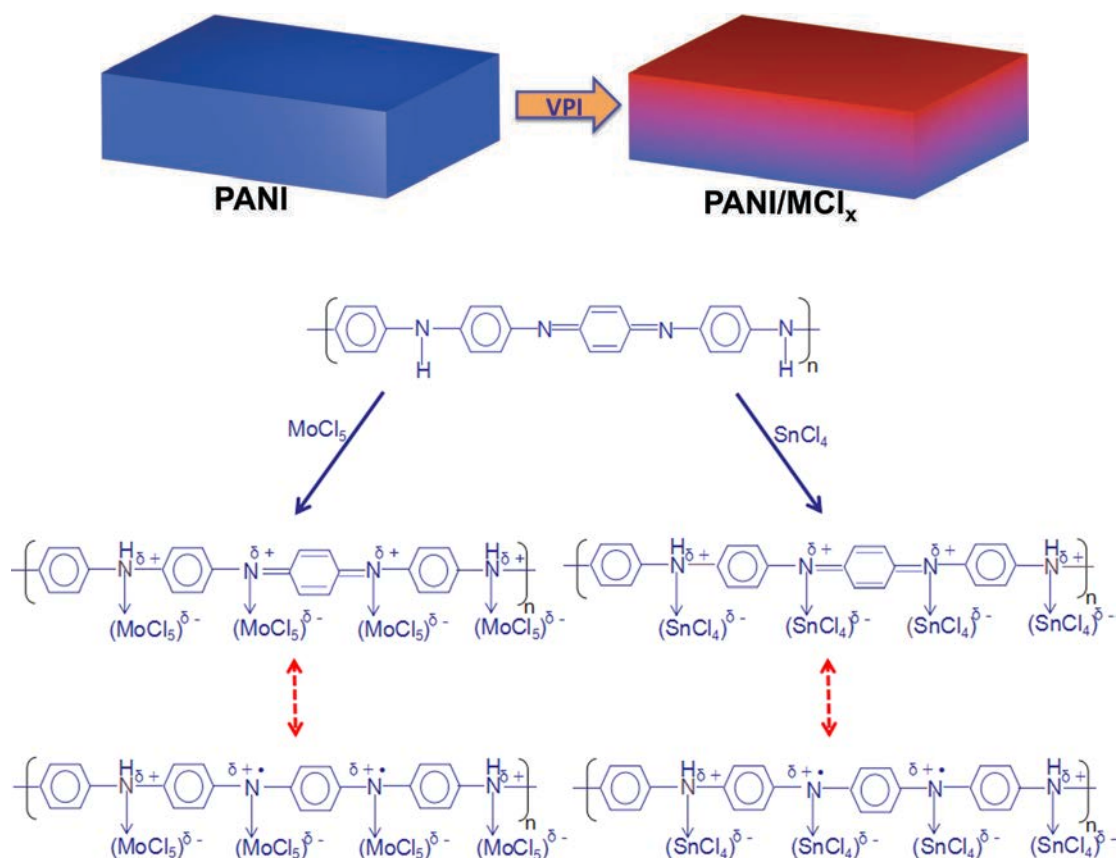


Figure 3.6 Proposed structures of PANI/MoCl₅ and PANI/SnCl₄ after vapor phase infiltration of PANI with MoCl₅ or SnCl₄.

into the PANI matrix oxidizes the nitrogen partially and binds to the polymer coordinatively. PANI is a hole transporter and upon VPI doping, which will create the positive polarons, the carrier density increases, resulting in the increased conductivity. From the UV-Vis spectra in Figure 3.7, we observe that on the one hand the band intensity at 336 nm decreases, while simultaneously the band intensity at 452 nm increases after both doping processes. Those signatures correspond to the π - π^* transitions in the benzenoid rings and indicate a stronger presence of benzenoid units. The band at 626 nm, which corresponds to the quinoid rings, nearly disappears as a result of the conversion of quinoid rings. The latter can be considered as a signature of polarons. Upon thermal treatment in vacuum, the conductivity decreases, which is a result of the deprotonation of the polymer and evaporation of HCl. The conductivity of PANI/1M HCl is consequently minimized. Only a minor decrease in conductivity is observed after thermal treatment of PANI/MoCl₅ and PANI/SnCl₄ in vacuum. The metal chloride bound to the PANI backbone will resist the thermal treatment, since the bonding of the metal to the nitrogen will stabilize the metal chloride and prevent its evaporation. The low vapor pressure of the metal chlorides compared to HCl is further supporting the chemical stabilization of the doped polymer.

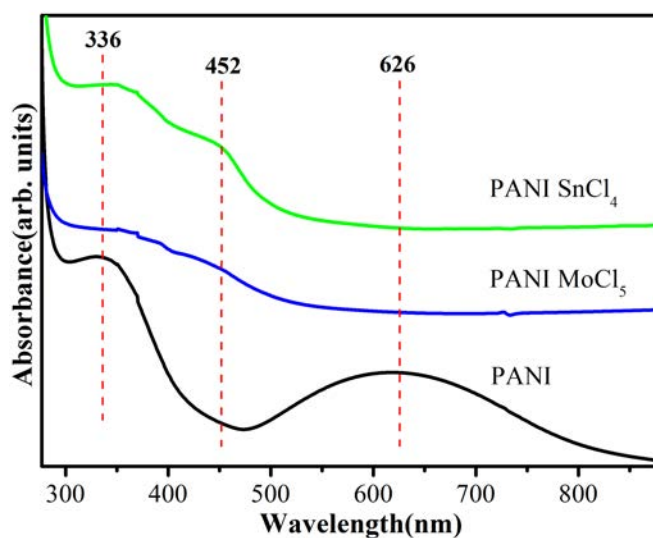


Figure 3.7 UV-Visible absorption spectra showing the 250-880 nm region of PANI, PANI/MoCl₅ (100 cycles) and PANI/SnCl₄ (60 cycles).

3.4 Conclusion

In conclusion, we successfully demonstrated a novel way of doping polyaniline by applying an ALD-derived single precursor vapor phase infiltration (VPI) and doping process. In this way, we are able to not only induce conductivity in PANI, but also to tune the conductivity through the choice and infiltrated amount of the vaporized precursors. More importantly, the conductivity of the PANI doped in our way was barely affected by a thermal treatment at 150 °C in vacuum, while the conductivity of the acid doped PANI (with 1 M HCl) was almost completely lost. This loss is likely due to a deprotonation of the doped polymer and evaporation of HCl, which results in recovery of the non-conductive emeraldine base of PANI. Doping with MoCl₅ or SnCl₄ on the other hand results in an oxidation of the PANI and presumably in complexation of the metal chlorides with the nitrogen contained in PANI. As a result, the electron mobility along the polymer chains is significantly enhanced and the structure is stabilized even at elevated temperatures. The results are not only significant for the novel process to dope PANI and obtain better thermal stability of the doped polymer, but also for the possibility to perform top-down doping of already manufactured PANI, which allows for better shaping of the material and therefore more efficient device fabrication. The results encourage future work, particularly the adaptation of similar infiltration processes to more challenging conductive polymers, including polypyrrole or polythiophene.

Chapter 4

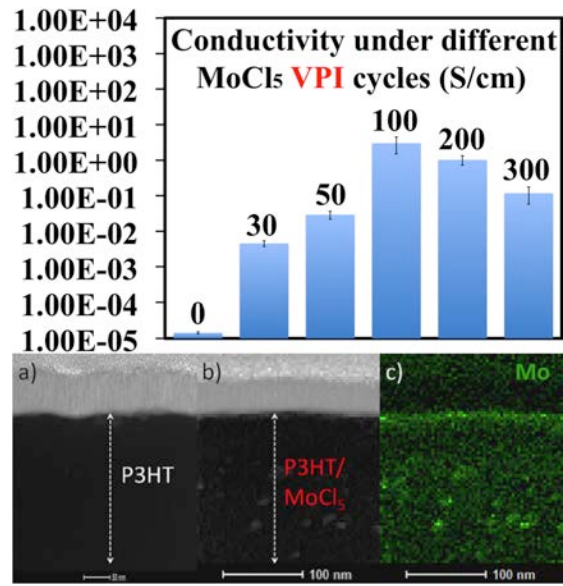
Controlling the Conductivity of Poly(3-hexyl)thiophene (P3HT) by Low Temperature VPI Process

Efficient doping of organic semiconductors is an important prerequisite for the fabrication of high performance organic electronic devices. In this chapter, a novel single precursor low-temperature (70 °C) vapor phase infiltration (VPI) process to dope poly(3-hexyl)thiophene (P3HT) is described. The infiltration is performed with the metal containing atomic layer deposition (ALD) precursor MoCl₅. The conductivities of the polymer were assessed with four-point probe measurements and showed significant enhancement of up to 5 orders of magnitude, confirming the efficiency of the VPI process. The chemical changes resulting from the infiltration of P3HT were characterized applying UV-Vis, Raman, XPS, and FTIR spectroscopy. The crystalline state of the material was analyzed by XRD. SEM micrographs and AFM images show that the morphologies of the samples before and after MoCl₅ infiltration process did not seriously change. TEM images of cross-sections of the thin film clearly show that the vapor phase infiltration process results in the incorporation of Mo into the bulk of the polymer.

This chapter describes the part of the thesis that was published in the journal *Journal of Materials Chemistry C* from the Royal Society of Chemistry (RSC). Graphs, figures and parts of the text of the publication are reused in this thesis with permission of the publisher.

Article:

Efficient and Controllable Vapor to Solid Doping of the Polythiophene P3HT by Low Temperature Vapor Phase Infiltration. **Weike Wang**, Chaoqiu Chen, Christopher Tollan, Fan Yang, Yong Qin, and Mato Knez. *Journal of Materials Chemistry C*. 2017, 5, 2686-2694.



Conductivities of P3HT after application of various numbers of VPI cycles and TEM images of cross-sections of untreated and infiltrated P3HT

4.1 Introduction

Over the past years, organic semiconductors (OSCs) have been extensively investigated due to their tremendous importance as integral part of a wide range of electrical devices¹⁵⁰⁻¹⁵³. For instance, previous studies have reported on enhanced mobilities of charge carriers in field-effect transistors (FETs) achieved by trap filling¹⁵⁴, improved charge injection in light-emitting diodes (LEDs)^{155,156} and, more recently, superior power conversion efficiencies in organic photovoltaics¹⁵⁷⁻¹⁶². The development of inorganic semiconductor devices has revealed that crucially important steps for enabling engineering of efficient electronics include controllable doping and realization of stable and controllable doped transport layers for both p - and n - type materials. The same considerations apply for the organic counterpart as well. However, doping strategies for OSCs are typically dissimilar to those for their inorganic counterparts and thus optimal schemes need to be evaluated from scratch. Even though doped OSC thin films have been shown to exhibit conductivities to 5-8 orders of magnitude higher than undoped films¹⁶³⁻¹⁶⁴, better understanding of the chemistry that occurs upon doping and evaluation of various strategies for improving their efficiency is expected to result in even more efficient OSCs, which will strongly impact the emerging field of organic electronics.

Doping of inorganic semiconductors is meanwhile well developed. Controlled introduction of atomic or ionic impurities into semiconductors became the fundamental enabler for the functionality of modern electronic devices as we experience them nowadays¹⁶⁵. The doping process allows tuning the band alignment at interfaces and markedly increases the conductivity even at ultralow doping ratios, as typically every covalently bound dopant atom donates one mobile charge carrier to the highly crystalline and ultra-pure semiconductor matrix. In contrast, doping of OSCs is achieved by adding comparatively strong electron acceptors or donors, resulting in a significant increase of the charge carrier density and therefore conductivity of such materials. Stable p-type doping is nowadays typically achieved by introducing transition metal oxides such as MoO₃¹⁶⁶ or WO₃¹⁶⁷ into the polymer or by adding molecular π -electron acceptors, for example, tetracyano-2,3,5,6-tetrafluoroquinodimethane (F4TCNQ)¹⁶⁸⁻¹⁷⁰, 2,2'-(perfluoronaphthalene-2,6-diylidene)dimalononitrile (F6TCNNQ)¹⁷¹, or 1,4,5,8,9,11-hexaazatriphenylenehexacarbonitrile(HATCN)¹⁷². The principle of doping with molecular π -electron acceptors has been proven to be applicable to a wide range of molecular semiconductors and polymers. The resulting conductivity of such F4TCNQ-doped organic materials can exceed 1 S/cm at highest dopant concentrations¹⁷³. Among the various molecular dopants, F4TCNQ gained prominence as reference dopant. The fundamental

mechanisms that determine the concentration and mobility of mobile holes in F4TCNQ-doped samples of the polymer poly(3-hexyl)thiophene, P3HT, have been identified and showed that in this particular donor-acceptor couple almost all employed F4TCNQ molecules undergo integer charge transfer (ICT), meaning that an electron is fully transferred from the π -electron system of a P3HT site to the F4TCNQ acceptor. This eventually results in positively charged P3HT (P3HT^+) and negatively charged F4TCNQ (F4TCNQ^-)¹⁷⁴. Thus, F4TCNQ-doping leads to a strong increase in the density of mobile charge carriers and consequently the electrical conductivity. However, as an alternative to the common π -electron acceptors, some recent reports introduced the possibility of doping of polymers with Lewis acids. The Bazan and Neher groups have studied the optical and charge carrier transport properties of various polymers which were doped by the strong Lewis acid tris(pentafluorophenyl)-borane (BCF)¹⁷⁴⁻¹⁷⁸. The effect has been explained with a formation of Lewis acid-base adducts. In the case of p-type doping with BFC, the electrophilic borane center binds to a moiety carrying an accessible lone pair of electrons, for example, the nitrogen atoms present in pyridine or the benzothiadiazole units of the semiconductor. The binding induces a redistribution of the electron density, that is, a charge transfer between the semiconductor and dopant occurs. This will eventually change the oxidation state of each of the partners, liberating charge carriers that become available for electrical conduction.

Given the already published results, the mentioned doping with Lewis acid appears to be a promising approach for obtaining efficient OSCs, but the doping process itself may still be further improved. Here, we apply a novel procedure for doping P3HT with the Lewis acid molybdenum (V) chloride (MoCl_5) and a detailed analysis of the resulting doped polymer. Doping of polymers is typically performed in liquid state, which introduces various chemical species such as solvents or byproducts of chemical reactions into the substrate with all the related potentially negative consequences for the conductivity and/or stability of the resulting material. Besides, the possibility of shaping the polymer after doping process is often hampered because of dopant-induced crystallization or hardening of the polymer. For avoiding such negative influences, we apply an alternative approach, vapor phase infiltration (VPI) process, for injecting the Lewis acid into the polymeric substrate. The VPI process is derived from atomic layer deposition (ALD)⁷⁶, and applies the same processing technology, that is, exposure of the substrates to vaporized chemicals in a pulsed manner with stringent control of the dosing parameters. This procedure allows taking advantage of the mobility of a vaporized chemical and its ability to diffuse into and react with polymeric substrates⁸⁸. Incorporation of inorganic materials into polymers often enhances some physical properties of the resulting composite or hybrid material¹¹⁰⁻¹¹⁴. For example, our earlier works demonstrated that infiltration of metal oxides or metal ions into various (bio)polymers,

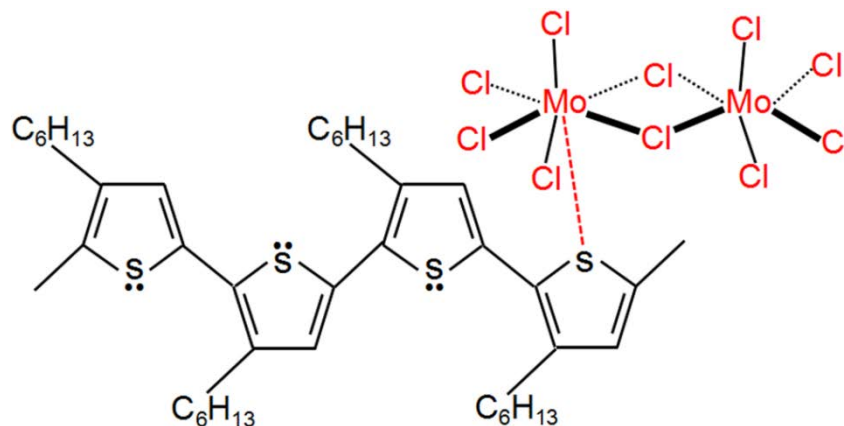


Figure 4.1 Schematic of the proposed Lewis acid-base adduct formation between poly(3-hexyl)thiophene, P3HT, and molybdenum(V)chloride, MoCl₅.

including spider silk⁹⁸, avian egg collagen¹⁰⁷ and cellulose¹⁰⁹ by means of ALD-derived strategies often results in hybrid materials with exceptional mechanical properties. The present work shows that a similar infiltration process can also be used for doping P3HT and furthermore allows for controlling the level of conductivity of the polymer through the number of infiltration cycles applied. In conjunction with MoCl₅, P3HT acts as a Lewis base for its lone electron pairs present at the sulfur atoms of the thiophene rings. A hypothesized interaction scheme between MoCl₅ and a P3HT segment is sketched in Figure 4.1. In this chapter we show that the introduction of MoCl₅ into P3HT by VPI leads to p-type doping, and the conductivity of P3HT/MoCl₅ can reach exceptional values of 3.01 S/cm which is up to 5 orders of magnitude higher than that of the native P3HT, while maintaining its stability for at least 30 days at ambient conditions.

4.2 Experimental Section

4.2.1 Preparation the Poly (3-hexyl) thiophene (P3HT) Thin Film

1,2-Dichlorobenzene (DCB) was purchased from Aldrich and used as received. Poly(3-hexylthiophene-2,5-diyl) (P3HT, $M_w = 50\,000\text{ g mol}^{-1}$, 95% regioregularity) was purchased from Reike Metals, Inc. U.S.A and used as-received. As substrates, the electrically insulating glass slides were used, which were cleaned thoroughly by sonication in acetone, methanol and isopropanol for 1 h prior to coating with P3HT. For pristine films, 37 mg P3HT was dissolved in 1 mL DCB. The thin films ($\approx 35\text{ }\mu\text{m}$) were prepared via drop casting the solution on glass substrates (1.3 cm \times 1.3 cm) at ambient conditions. All samples were soft-baked at 70 °C overnight to remove excess solvent.

4.2.2 Vapor Phase Infiltration Process of P3HT Thin Film

Vapor-phase infiltration was performed using a homemade atomic layer deposition tool. Pristine P3HT films coated on glass substrates were exposed to vapors of MoCl₅ in a pulse-exposure-purge sequence with various numbers of repetition cycles. One cycle of the process consisted of following settings: the precursor (MoCl₅, 95%, Aldrich) was pulsed into the reaction chamber for 5 s and thereafter exposure of the substrates to the vapors in the reaction chamber was allowed for 120 s. The exposure was followed by a 60 s purge step. The cycle was repeated with the number of cycles varying between 10 and 300. As carrier and purging gas N₂ (99.99%) was used. The chamber temperature was kept constant at 70 °C during the infiltration process with the base pressure of the reactor having been maintained at 50 mTorr. Since at room temperature MoCl₅ is solid, heating of the precursor to 85 °C was required to obtain a reasonable vapor pressure.

4.2.3 Characterization

Absorption spectra of the samples were recorded between 360-890 nm using a UV-Vis spectrophotometer (V-630 BIO, JASCO).

Raman spectra with a 532 nm (100 \times objective) exciting wavelength were collected with a Raman microscope (Alpha 300S, WITec). The laser power was kept at 0.02 mW and the acquisition time was limited to 10-20 s for each measurement to avoid sample degradation. The Raman spectra were background corrected and obtained by averaging spectra obtained from five different regions of each sample.

XPS experiments were conducted using a PHOIBOS photoelectron spectrometer equipped with an Al K α X-ray source (12 mA, 8.33 kV) as the incident photon radiation, and the spectra were standardized using the C1s peak at 284.6 eV.

X-ray diffraction (XRD) analysis was carried with a powder diffractometer (X'pert with 45 kV, 40 mA; PANalytical) with Ni-filtered Cu K α radiation.

Infrared spectra of the samples were recorded between 760 and 1610 cm⁻¹ with a FTIR Spectrometer (Frontier; PerkinElmer).

The morphology of the samples was characterized by scanning electron microscopy (SEM, Quanta 250 FEG; FEI) and the chemical composition was analyzed with energy-dispersive X-ray spectroscopy (EDS). Thickness measurements were carried out on a cleaved cross-section of the sample by FEG-SEM.

AFM analysis was performed on P3HT-coated glass slides, employing a 5500 AFM (Keysight, Santa Clara). The AFM probe was a HQ-NSC 14/Al BS tip with an approximate tip radius of 8 nm. The spring constant of the cantilevers was 5 N/m and a resonance frequency of 160 KHz was used in tapping mode; data processing was done using the software Gwyddion.

TEM images were recorded and EDS analysis were carried out with an FEI Titan microscope using an acceleration voltage of 300 kV in scanning transmission electron microscopy mode and an EDAX SDD detector. The focused ion beam (FIB) used for lamellae preparation was a dual beam Helios Nanolab 450S from FEI. The FIB lamellae were prepared from a glass wafer with the P3HT thin film deposited on it and after the entire wafer had undergone MoCl₅ vapor phase infiltration treatment. The block was extracted by standard methods using a Pt electron beam deposition to initially protect the sample surface before any ion beam deposition was carried out. The block was thinned to transparency on a copper "Omniprobe" grid using a 5 kV gallium ion beam at 8 pA for final surface preparation.

The conductivities of the thin films were measured applying a four-point probe technique with a source measurement unit (Keithley 2611). For each VPI experiment four or five individual samples were tested for each VPI process cycle number. The resulting conductivity, σ , was calculated according to the formula,

$$\sigma = \ln 2(I / \pi dV)$$

where I is the current, V is the voltage and d is the whole polymer film thickness.

4.3 Results and Discussion

4.3.1 Assessment of the electrical conductivity

The functionalization of P3HT thin films with MoCl_5 through the vapor phase infiltration process resulted in the introduction of mobile carriers into the conjugated polymer, and therefore in an enhanced conductivity. In contrast to a typical ALD process or previously described ALD-based infiltration strategies, where a substrate is sequentially exposed to vapors of two precursors, here we expose the substrate to the vapor of only one precursor and allow sufficient time for the precursor to diffuse into subsurface areas of the substrate. After infiltration, we measured the electrical characteristics of the samples. Figure 4.2 (a) shows the room temperature I - V plots of the various fabricated P3HT samples in comparison to the untreated polymer. The thicknesses of all samples were comparable ($\approx 35 \mu\text{m}$). The plots of P3HT/ MoCl_5 are linear, confirming ohmic behavior over the whole measurement range. Untreated P3HT thin films act as reference with conductivity values of $1.44 \times 10^{-5} \text{ S/cm}$. The increase in conductivity confirms the possibility of using the vaporized Lewis acid MoCl_5 for doping P3HT. The values for the electrical conductivities of the samples were extracted from the slopes of the I - V plots. An important observation resulting from the measurements is that the conductivity of the doped P3HT films stands in non-linear correlation with the number of infiltration cycles as can be seen in Figure 4.2 (b). The peak value of the conductivity with 3.01 S/cm is reached after 100 infiltration cycles, while lower and higher number of cycles result in lower conductivities.

At low MoCl_5 doping levels, the carrier concentration will increase linearly with the doping concentration while their mobility will decrease unproportionally, hence the conductivity will increase with doping. However, upon heavy doping, a significant fraction of the dopant remains inactive. Once the concentration of dopants exceeds the solubility limit in the polymer, the dopants will cluster resulting in the carrier concentration stagnating. These dopants will further cause enhanced scattering of the electrons and contribute to a decrease in their mobility.

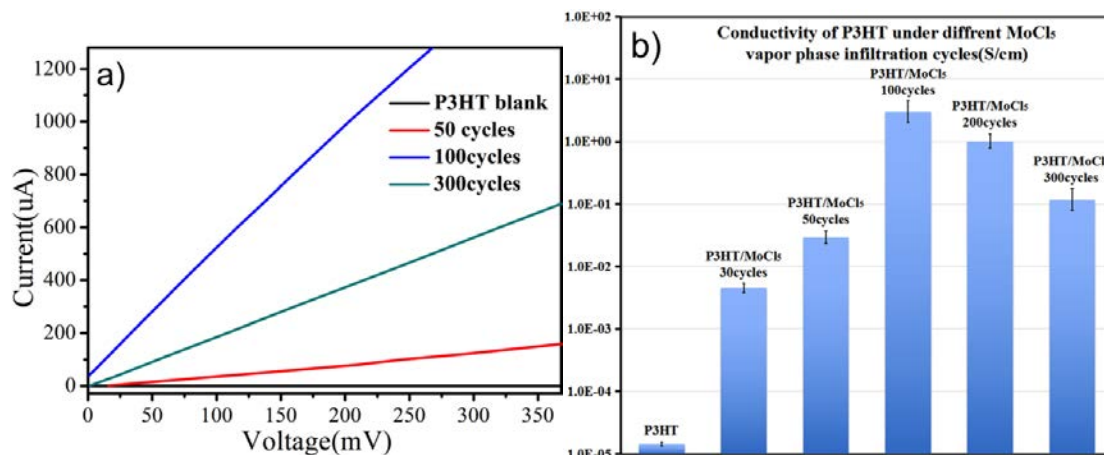


Figure 4.2 (a) *I-V* plots of undoped P3HT (black) and MoCl₅-doped P3HT after 50 (red), 100 (blue), and 300 (cyan) processing cycles; (b) comparison of the conductivities of undoped P3HT blank and P3HT doped with MoCl₅ after various cycles numbers (30, 50, 100, 200, and 300 cycles) processed at 70 °C.

4.3.2 UV-Vis spectroscopy

Successful p-doping of the conjugated polymer P3HT by the Lewis acid MoCl₅ through applying the VPI process was further confirmed by various spectroscopies. Optical (absorption and emission) as well as Raman and Fourier Transform Infrared (FTIR) spectra were taken from the infiltrated samples to confirm and identify chemical changes in the polymer.

The UV-Vis spectra of P3HT and P3HT/MoCl₅ after application of various VPI cycle numbers are shown in Figure 4.3 (a). Pristine P3HT strongly absorbs in the region between 500 and 650 nm, with three distinct maxima at 518, 552, and 605 nm. These three bands are typically attributed to the ordered lamellar phase of P3HT and correlate to electronic π - π^* transitions^{179,180}. The band at 552 nm is attributed to the absorption of extended conjugated systems and the band at 605 nm is attributed to interchain interactions. The UV-Vis absorption spectra acquired from P3HT/MoCl₅ (10 cycles) largely correspond to those of pristine P3HT, albeit with a lower intensity. Interestingly, with an increasing number of VPI cycles, and thus doping concentration, a bleaching of the main π - π^* absorption band of P3HT centered at \approx 530 nm was observed. At the same time a new absorption maximum at 478 nm developed, accompanied by a gradual increase in the sub-gap absorption in the infrared region around 826 nm (Figure 4.3 (a))^{179,180}. The reduction of the main π - π^* absorption band suggests that the presence of MoCl₅ in elevated concentration (100 VPI cycles) weakens the

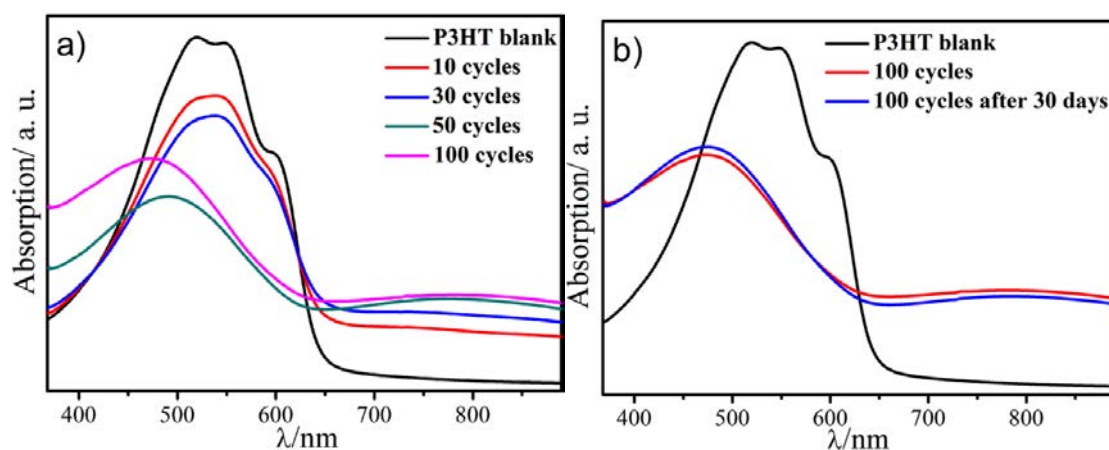


Figure 4.3 (a) UV-Visible absorption spectra showing the 350-890 nm region of untreated P3HT (black) and MoCl_5 -infiltrated P3HT after 10 (red), 30 (blue), 50 (cyan), and 100 (magenta) infiltration cycles at 70 °C; (b) absorption spectra of untreated P3HT (black), MoCl_5 -infiltrated P3HT after 100 infiltration cycles as prepared (red), and after 30 days storage at ambient conditions (blue).

interchain interactions, resulting from a disordering effect of MoCl_5 on the crystalline phase of P3HT. These observations point towards the presence of a ground-state charge transfer from P3HT to MoCl_5 , triggered by an effective transfer of electrons from the polymer (*viz.* oxidation) to the electron-poor MoCl_5 . This eventually results in the formation of positive polarons. It is worth noting that the P3HT/ MoCl_5 samples are temporally very stable. This becomes obvious if the stability of our infiltrated samples is compared to that of reported P3HT/FTS (FTS: fluoroalkyl trichlorosilane). In the latter case, upon exposure to air, the absorption spectra, the original color, and the initial high electrical resistivity recover within 4-5 days in the dark or within hours under illumination¹⁸¹, while in the present case the absorption spectra of MoCl_5 -doped P3HT (Figure 4.3 (b)), the perceived color, and the measured conductivities only marginally changed upon exposure of the samples to air in ambient conditions for 30 days.

4.3.3 Raman spectroscopy

Figure 4.4 shows a typical Raman spectrum of a P3HT thin film excited with a laser operating at 532 nm. Various Raman modes can be observed in the region 700-1545 cm^{-1} : the main in-plane ring skeleton modes at 1452 cm^{-1} (symmetric C=C stretching) and at 1384 cm^{-1} (C-C intra-ring stretching), the inter-ring C-C stretching mode at 1212 cm^{-1} , the C-H bending mode with C-C inter-ring stretching mode at 1185 cm^{-1} , and the C-S-C deformation mode at 731 cm^{-1} ¹⁸². Among the observed Raman modes, we will focus on the two main in-plane ring skeleton modes at 1452 and 1384 cm^{-1} , and the C-S-C deformation mode at 731 cm^{-1} , as those

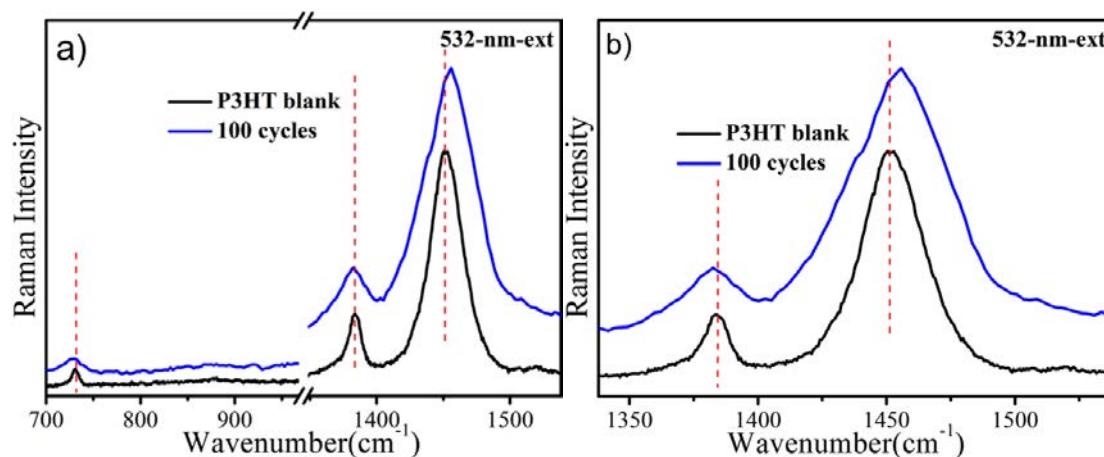


Figure 4.4 Raman spectra of untreated P3HT, and MoCl_5 -infiltrated P3HT after 100 VPI cycles at $70\text{ }^\circ\text{C}$ showing (a) the $700\text{-}1545\text{ cm}^{-1}$ region, and (b) the $1330\text{-}1575\text{ cm}^{-1}$ region.

are expected to be sensitive to electron delocalization and thus the extension of the conjugation in P3HT.

From the spectra in Figure 4.4 and the respective data in Table 1, one can observe that the Raman peak of the P3HT C=C mode shifts from 1452 cm^{-1} to 1457 cm^{-1} after infiltration. This C=C peak position and its width are indicative of the degree of molecular order in P3HT¹⁸². The position shift of ca. 5 cm^{-1} together with the increasing full width at half maximum (fwhm) from 30 cm^{-1} to 47 cm^{-1} after infiltration indicate a disturbance of the order in the P3HT upon infiltration. Further significant changes can be observed in the peak position and fwhm of the C-C mode. The peak shifts by 4 cm^{-1} with the fwhm rising from 11 cm^{-1} to 22 cm^{-1} . Similar to the case of the C=C mode described above, this change in the C-C mode also indicates a disturbance of the molecular order in P3HT after the MoCl_5 VPI process. In addition, we also note significant changes in the peak position and fwhm of the C-S-C mode, namely a slight shift from 731 cm^{-1} to 728 cm^{-1} with the fwhm rising from 9 cm^{-1} to 26 cm^{-1} . This is an obvious sign for ring deformations in the P3HT molecule, which most likely result from a strong interaction between Mo atoms and S atoms after the VPI process. Such an interaction is further confirmed by the S 2p XPS spectra shown in Figure 4.5.

Table 1. Summary of the peak positions and the full width at half maxima (fwhm) of the C=C stretching mode, the C-C stretching mode and the C-S-C deformation mode for untreated P3HT and MoCl₅-infiltrated P3HT after 100 VPI cycles.

Sample	Peak Position and (fwhm) of C=C Mode (cm ⁻¹)	Peak Position and (fwhm) of C-C Mode (cm ⁻¹)	Peak Position and (fwhm) of C-S-C Deformation Mode (cm ⁻¹)
Untreated P3HT	1452 (30)	1384 (11)	731 (9)
P3HT/MoCl ₅ (100cycles)	1457 (47)	1380 (22)	728 (26)

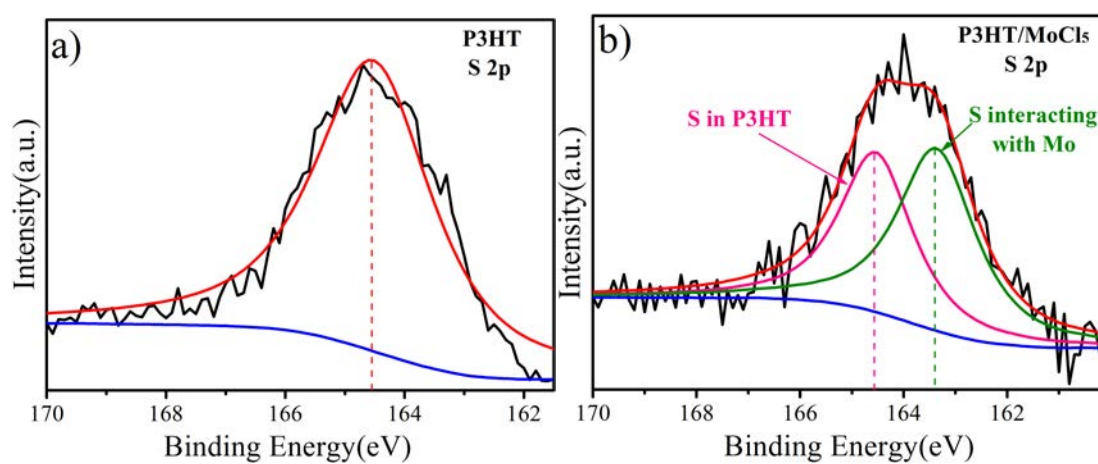


Figure 4.5. S 2p XPS spectra of pristine P3HT (a), and P3HT/MoCl₅ (5 cycles VPI, 70 °C) (b).

The peak located at 164.56 eV corresponds to the S 2p signal of pristine P3HT (Figure 4.5 (a)). After applying 5 cycles of the MoCl₅ infiltration process, the intensity of the S 2p peak of the pristine P3HT decreased, and a new peak at a binding energy of 163.39 eV developed, which indicates that S is interacting with Mo and an electronic exchange between P3HT and MoCl₅ occurs (Figure 4.5 (b)). Considering the above-mentioned, we conclude that the MoCl₅ VPI process has significantly decreased the degree of order of P3HT molecules in the resulting P3HT/MoCl₅ thin film. Furthermore, the changes in the peak position and fwhm of both the C-C mode and the C-S-C mode strongly suggest the formation of positive polarons in the polymer matrix.

4.3.4 Infrared spectra

More details about the chemical changes occurring in the polymer after infiltration can be extracted from the infrared spectra of P3HT before and after infiltration, which are shown in Figure 4.6. The black spectrum is taken from the untreated P3HT and is used as reference

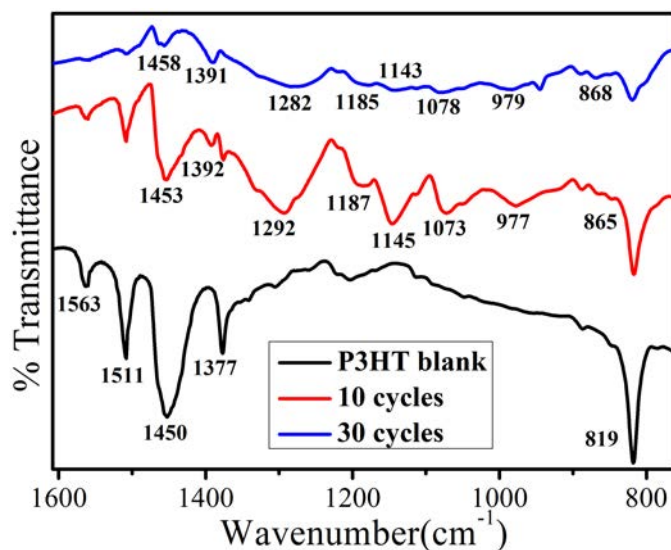


Figure 4.6 FT-IR spectra (region between 760 and 1610 cm^{-1}) of untreated P3HT (black), and MoCl_5 -infiltrated P3HT applying 10 (red) and 30 (blue) infiltration cycles at 70 $^\circ\text{C}$.

for identifying chemical changes. The red and blue spectra were measured from P3HT/ MoCl_5 samples after processing with 10 and 30 infiltration cycles, respectively. The latter spectra indicate that the main carriers that were generated were positive polarons, which can be derived from the observation of the polaron bands at 1391, 1282, 1143, 1078, 979, and 868 cm^{-1} , respectively, after the 30 cycles MoCl_5 VPI process¹⁸³. Especially the bands observed at 1391 and 1392 cm^{-1} , evolve newly after the MoCl_5 VPI process. Furthermore, the shifts of modes that were observed upon applying different VPI cycle numbers in Figure 4.6 are changes in modes that originate from effective conjugation within the molecules.

4.3.5 X-ray diffraction

In order to investigate the internal structure of the P3HT thin film, X-ray diffraction (XRD) was applied. Figure 4.7 shows XRD patterns of untreated P3HT and P3HT/ MoCl_5 after various infiltration cycle numbers (30, 50 and 100). The untreated P3HT shows a (100) reflection peak, which is due to the lamellar layered structure¹⁶⁸. The further (100), (200), and (300) diffraction peaks indicate crystallinity with edge-on chain orientation¹⁶². The out-of-plane reflection peak (010) results from π - π interchain stacking¹⁸⁴. With an increasing number of MoCl_5 VPI cycles, the (n 00) diffraction peaks shifted towards lower angles, which confirms structural perturbations in the alkyl stacking direction¹⁸⁵, a sign that the lamellar

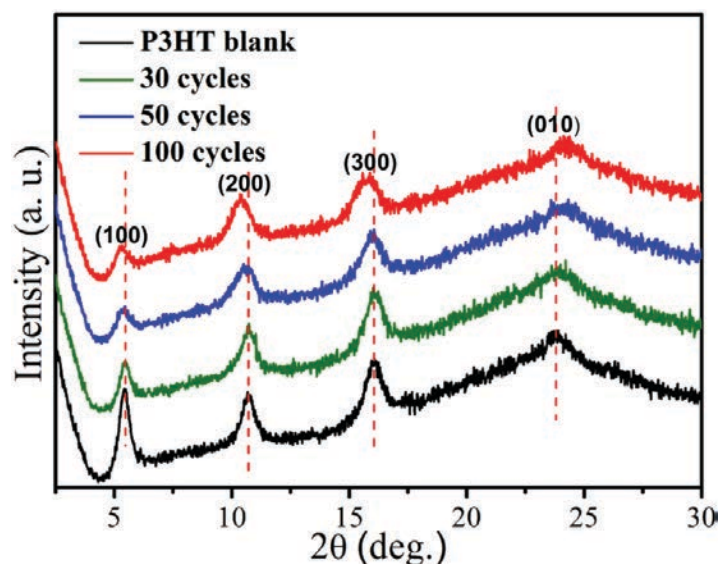


Figure 4.7 X-ray diffraction spectra of untreated P3HT (black), and MoCl_5 -infiltrated P3HT after 30 (green), 50 (blue), and 100 (red) infiltration cycles.

spacing increases. The (010) diffraction peak shifted to larger angles, which can be explained with the π -stacking spacing decreasing, thereby indicating less ordering in the doped film after the MoCl_5 VPI process. A significant increase in peak width in the ($n00$) signals further confirms that the infiltrated MoCl_5 significantly increases the disorder in the alkyl stacking direction. The MoCl_5 VPI process significantly affects the order and d-spacing in the alkyl stacking direction, which will influence the electrical properties of P3HT thin film¹⁸⁶. This is confirmed by the present study.

4.3.6 SEM, AFM and TEM

Scanning electron microscopy (SEM, Figure 4.8) and atomic force microscopy (AFM, Figure 4.9) were applied to evaluate the morphology of the samples before and after the VPI process. These images show that after infiltration with MoCl_5 , the P3HT surface becomes decorated with nanoscale islands. Based on the AFM images, the surface roughness increases from 18.4 nm to 22.1 nm. A possible reason for that may be the aforementioned intercalation of MoCl_5 into the polymeric matrix, which results in swelling of the polymer. Consequently, release of the stress may occur on a local level by expulsion of polymeric material to the surface. With an elevated Mo-precursor concentration at the surface of the polymer and strong electrostatic interactions between the negatively charged MoCl_5^- and the positively charged, P3HT^+ , we can expect some local aggregation of the crystalline P3HT to nanoscale islands.

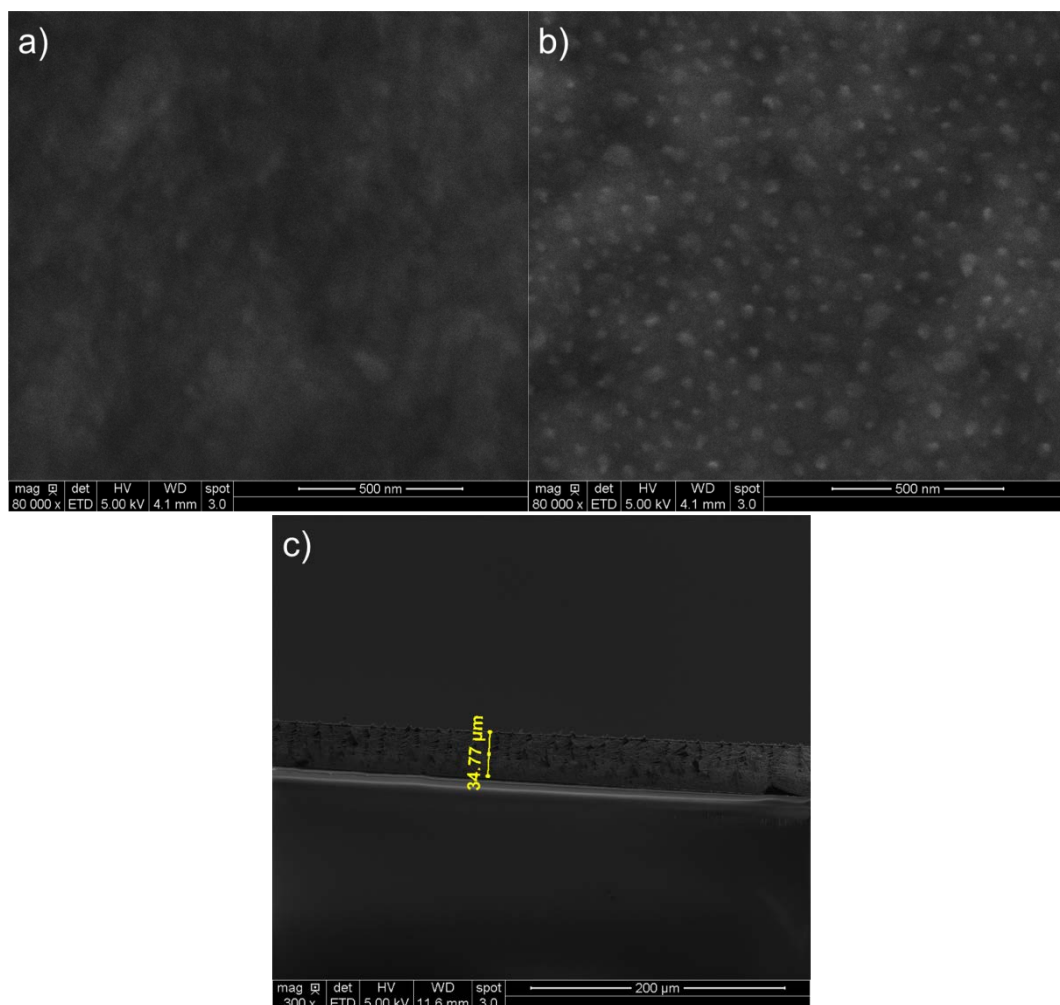


Figure 4.8 Scanning electron microscopy images of (a) untreated P3HT, (b) P3HT/MoCl₅ (100 cycles, 70 °C), and (c) a low magnification image of the cross-section of the P3HT thin film.

These islands or roughnesses would expectedly have a negative surface dipole moment and thus repel each other, which may explain the high dispersion and uniform size distribution observed in the SEM and AFM images¹⁸⁷. In Figure 4.10, such elevated concentration of Mo at the surface of the polymer can be seen. The TEM-EDS images show a cross-sectioned area of untreated P3HT and MoCl₅-infiltrated P3HT (100 cycles, 70 °C), prepared by a focused ion beam. Besides the higher concentration at the surface, a considerable amount of Mo is found in the bulk of the sample, which clearly shows that the vapor phase infiltration process results in the incorporation of Mo-precursor into the bulk of the polymer. Aggregations are found in the bulk of the samples, which indicate a similar type of crystallite formation in the bulk as observed on the surface of the polymer. Being spatially isolated, those aggregates, however, are not considered to be the main reason for the increase in conductivity, but rather the well dispersed Mo-precursor in the polymer matrix.

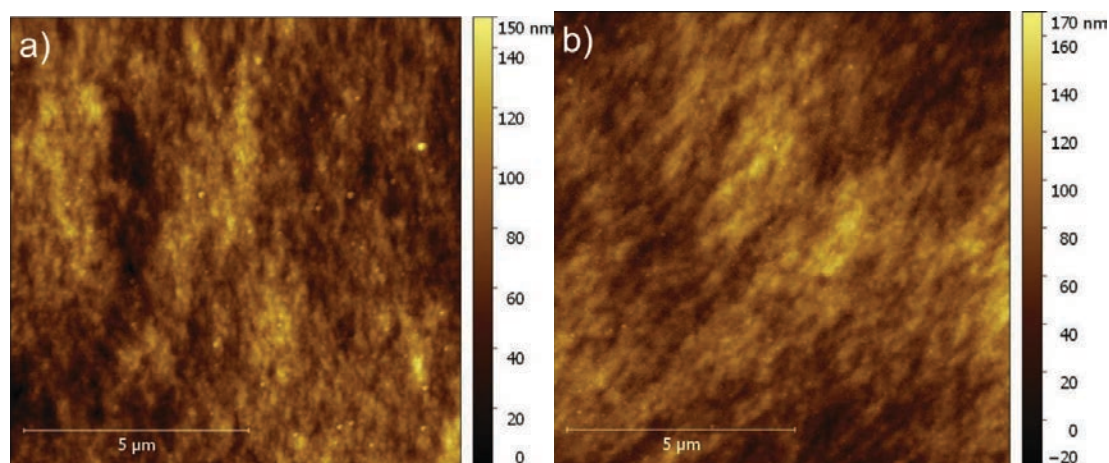


Figure 4.9 AFM images of (a) untreated P3HT, and (b) P3HT/MoCl₅ (100 cycles, 70 °C).

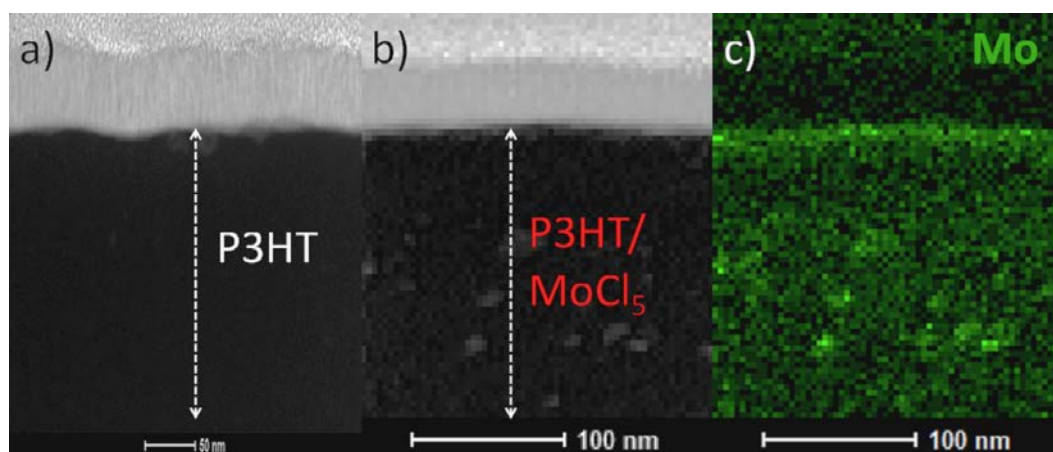


Figure 4.10 (a) TEM image of a cross-sectioned untreated P3HT thin film, (b) TEM image of a cross-sectioned MoCl₅-infiltrated P3HT thin film (100 cycles, 70 °C), and (c) Mo elemental map of the sample shown in (b).

4.4 Conclusions

To summarize, we have demonstrated a novel and efficient way of doping P3HT by applying an ALD-derived single precursor low temperature vapor phase infiltration (VPI) process. As a result, a great increase of the electrical conductivity of P3HT was observed. Upon doping by infiltration of the Lewis acid MoCl₅, the conductivity rose by up to 5 orders of magnitude, reaching 3.01 S/cm at its best. More importantly, the P3HT/MoCl₅ thin films exhibited exceptional stability in ambient conditions, largely outperforming the stability of previously reported P3HT/FTS. Doping with MoCl₅ from the vapor phase results in a local oxidation of the P3HT, owing to the Lewis basic character that P3HT shows in conjunction with MoCl₅. The lone electron pairs at the sulfur atoms of the thiophene rings in P3HT can

donate negative charge to the MoCl_5 with themselves becoming rather positively charged. The results are not only significant for the novel process to dope P3HT and obtain better stability of the doped polymer at ambient conditions, but also for the possibility to perform top-down doping of already pre-manufactured P3HT, which allows for better shaping of the material and therefore more efficient device fabrication. Furthermore, ALD processes can be adapted to the industrial level, opening the doors for the infiltration processes to be adapted and incorporated into roll-to-roll production lines for organic electronic devices. The results encourage future work, particularly the adaptation of similar infiltration processes to more challenging conductive polymers, other p-type molecular crystals, including rubrene and tereacene, or further n-type molecular crystals.

Chapter 5

Conductive Polymer-Inorganic Hybrid Materials through Synergistic Mutual Doping of the Constituents

Polymer matrix based inorganic-organic hybrid materials are at the cutting edge of current research for their great promise of merging properties of soft and hard solids in one material. Infiltration of polymers with vapors of reactive metal organics is a pathway for post-synthetic blending of the polymer with inorganic materials. This chapter shows that the MPI process is also an excellent method for fabricating conductive hybrid materials. Polyaniline (PANI) was infiltrated with the precursor pair diethylzinc (DEZ) and H₂O and the initially insulating polymer was converted to a PANI/ZnO hybrid with conductivities as high as 18.42 S/cm. The conductivity is based on a synergistic effect of the constituting materials where the inorganic and the polymeric fractions mutually act as dopants for the counterpart. The process temperature is a very important factor for a successful infiltration and the number of applied infiltration cycles allows tuning the level of conductivity of the resulting PANI/ZnO.

This chapter describes the part of the thesis that was published in the journal *ACS Applied Materials & Interfaces* from the American Chemical Society (ACS). Graphs, figures and part of the text of the publication are reused in this thesis with permission of the publisher.

Article:

Conductive Polymer-inorganic Hybrid Materials through Synergistic Mutual Doping of the Constituents. **Weike Wang**, Chaoqiu Chen, Christopher Tollan, Fan Yang, Mikel Beltrán, Yong Qin, and Mato Knez, *ACS Applied Materials & Interfaces*, 2017, 9, 27964-27971.



Schematic indicating the different resulting types of composites once a polymer is processed by atomic layer deposition (ALD) or multiple pulsed vapor phase infiltration (MPI).

5.1 Introduction

Because in the late 1970s copper-like electrical conductivities were reported in polyacetylene films³, considerable efforts have been devoted on ways to improve the conductivities of various polymers and their incorporation into practical applications, such as light emitting diodes, solar cells, thin-film transistors, batteries, and supercapacitors¹²⁸⁻¹³². Among the meanwhile great variety of available conducting polymers, polyaniline (PANI) belongs to the most prominent and best investigated intrinsically conducting polymers and enjoys great attention in research since many decades. Based on very promising scientific results, a variety of applications for PANI have already been proposed including, drug delivery, sensor applications, actuators, antistatic coatings, corrosion protection, rechargeable batteries, microwave absorbers, electro-optic and electrochromic devices, etc.^{25,133}. The interest in this material is resulting from its facile polymerization, great environmental stability, simple acid/base doping/dedoping processes and its rich redox chemistry¹⁷. PANI is an organic semiconductor by virtue of its highly conjugated π -delocalized molecular backbone. The molecular construction resembles a dynamic block copolymer consisting of oxidized quinoid rings and reduced benzenoid rings. The emeraldine base, which is used for the work presented in this manuscript, can be doped to obtain the conductive form of the polymer. A variety of strategies to dope PANI have been developed and include treatments with inorganic protonic acids^{134,135}, organic acids¹⁸⁹, alkali metal salts^{138,139}, Lewis acids^{140,141}, and transition metal salts¹⁴². Besides, some inorganic oxides such as SnO₂¹⁹⁰, Al₂O₃, TiO₂¹⁹¹, ZnO¹⁹¹⁻¹⁹³, Mn₃O₄¹⁹⁴ have also been successfully used as dopants.

If applied to polymers in a more general scope an incorporation of inorganic materials often enhances the mechanical, optical, or electronic properties of the resulting composite or hybrid material¹¹¹⁻¹¹⁴. However, most incorporation processes are commonly carried out in solution, which not only has negative influence on the polymer morphology, structure and purity, but also makes in situ testing of the physical and/or chemical properties inconvenient. The influence of solvents on the incorporation or doping process may potentially be avoided, but this requires a complete revision of the involved procedures. A promising way to realize this goal lies in gas phase processing, which may allow for a top-down synthesis of conducting polymer-inorganic hybrid materials. A very recently developed technique for infiltration of soft materials with inorganics relies on a modified version of atomic layer deposition (ALD) that takes advantage of the mobility of a vaporized precursor to diffuse into and react with synthetic and/or natural polymers⁸⁸. The use of highly reactive metal organic molecules as precursors and the absence of solvents open the doors for chemical reactions in

the subsurface area of the substrate with functional groups that a solvent would otherwise shield. In this way, a new hybrid material will be formed which exhibits physical properties different to the materials obtained with currently known routes. Our group has explored the infiltration of a number of biopolymers, including spider silk⁹⁸, egg collagen¹⁰⁷, and cellulose¹⁰⁹. Our focus until now was on the improvement of mechanical properties, which was proven to be impressive. Given that the substrate is chemically modified, not only mechanical properties, but also electronic properties of the substrate may be altered. Here, we demonstrate that the multiple pulsed infiltration (MPI) process applying the two typical ALD precursors diethylzinc (DEZ) and water (H₂O) is very well suitable for enhancing the conductivity of PANI and in this way serves as superior doping strategy for this material (Figure 5.1). The components of the resulting hybrid material will mutually dope each other with the resulting conductivities greatly outperforming those of conventionally doped PANI. This method also offers further advantages such as posterior modification of polymers already integrated into designed assemblies, avoiding a purification step, circumventing difficulties in forming the polymer after doping, etc., which makes it a very interesting alternative to established strategies even for industrial applications.



Figure 5.1 Schematic indicating the different resulting types of composites once a polymer is processed by atomic layer deposition (ALD) or multiple pulsed vapor phase infiltration (MPI). With MPI the substrate is exposed to vapors of DEZ and H₂O in a sequential manner. Extended exposure times enable the precursors to diffuse into the polymer and react with the molecular backbone in the subsurface area forming a polymer-inorganic hybrid with a concentration gradient depending on the duration of exposure.

5.2 Experimental Section

5.2.1 Preparation the the Polyaniline (PANI) nanofibers Thin Film

The synthesis of PANI nanofibers was carried out by rapid mixing polymerization as reported in the literature¹³⁵. All chemicals were of analytical grade and used as received. Typically, aniline (3.2 mmol, 0.291 ml) and ammonium peroxydisulfate (0.8 mmol, 0.183 g) were dissolved in 10 ml of 1M HCl each. The two solutions were rapidly mixed at room temperature (20 °C) and immediately shaken to ensure sufficient mixing. After 12 h, the polymerization was concluded and the resulting 1M HCl doped polyaniline was collected by filtration and repeatedly washed with 1M HCl until the filtrate became colorless. Thereafter, the polymer was dried in vacuum at 50 °C. Dedoped polyaniline was obtained by treating PANI/1M HCl with aqueous ammonium hydroxide (5%) for 1h and subsequent washing with deionized (DI) water until the filtrate became neutral. The dedoped PANI was dried in vacuum at 60 °C. PANI films were prepared by drop-casting its aqueous dispersion (200 μ l) onto glass slides (1.3 \times 1.3 cm²). The glass substrates were precleaned with acetone, deionized water (DI), and isopropanol in that sequence. The resulting samples were dried in an oven at 60 °C for 12 h.

5.2.2 Vapor Phase Infiltration Process of PANI Thin Film by ZnO Multiple Pulsed Infiltration (MPI)

Vapor-phase infiltration was done in an ALD reactor (Savannah S100, Cambridge Nanotech Inc). Dedoped PANI films on glass slides were placed into the ALD chamber and dried at 155 °C in a vacuum environment (20 mTorr) with a steady N₂ gas stream (50 sccm) for 2 h. Diethyl zinc (DEZ, Strem Chemicals, 99.99%) and purified H₂O were used as sources for Zn and oxygen, respectively. Each cycle was composed of a pulse, exposure, and purge sequence for each precursor. One cycle of the process was as follows: the precursor DEZ was pulsed into the reaction chamber for 0.08 s and held in the reaction chamber for 120 s, followed by a 60 s purge step to remove excess DEZ. In the same manner, the pulse (0.018 s)/exposure (120 s)/purge (60 s) sequence of water was applied. This DEZ/water cycle was repeated as many times as indicated in the sample assignment. As-delivered and purged gas N₂ was used. The reaction temperature was 155 °C, and the base pressure of the reactor was 50 mTorr.

5.2.3 Characterization

Fourier-transform infrared (FTIR) spectra of the samples were recorded between 750 and 1680 cm^{-1} with an FT-IR spectrometer (Frontier; PerkinElmer).

Morphology examination of the samples was done with a scanning electron microscope (SEM, Quanta 250 FEG; FEI) at 10kV. Thickness measurements were carried out on a cleaved cross-section of the sample by FEG-SEM.

Raman spectroscopy at 532 cm^{-1} excitation wavelength was performed with a Raman microscope (Alpha 300S, WITec). The laser power was kept below 0.7 mW to avoid sample degradation.

Absorption spectra of the samples were recorded between 375-960 nm using a UV-Vis spectrophotometer (V-630 BIO, JASCO).

X-ray diffraction (XRD) analysis was carried with a powder diffractometer (X'pert, with 45 kV, 40 mA; PANalytical) with Ni-filtered Cu $K\alpha$ radiation.

XPS experiments were conducted using a PHOIBOS photoelectron spectrometer equipped with an Al $K\alpha$ X-ray source (12 mA, 8.33 kV) as the incident photon radiation, and the spectra were standardized using the C1s peak at 284.6 eV.

TEM images were recorded and EDS analysis was carried out with an FEI Titan microscope using 300 kV in scanning transmission electron microscopy mode and an EDAX SDD detector. The focused ion beam (FIB) used for lamellae preparation was a dual beam Helios Nanolab 450S from FEI. FIB lamellae were prepared from a Si wafer with the PANI fibers deposited on it and after the entire wafer had undergone the ZnO MPI treatment. The block was extracted by standard methods using a Pt electron beam deposition to initially protect the sample surface before any ion beam deposition was carried out. The block was thinned to transparency on a copper "Omniprobe" grid using a 5 kV gallium ion beam at 8 pA for final surface preparation.

The conductivities of the thin films were measured applying a four-point probe technique with a source measurement unit (Keithley 2611). For each experiment four or five individual samples were tested for each MPI process cycle number. The resulting conductivity, σ , was calculated according to the formula,

$$\sigma = \ln 2(I / \pi dV)$$

where I is the current, V is the voltage, and d is the polymer film thickness.

5.3 Results and Discussion

5.3.1 Assessment of the electrical conductivity

After successful fabrication of dedoped PANI films supported on glass slides, the samples were infiltrated with ZnO. In order to be able to identify the influence of infiltration on the conductivity, a variety of processes have been applied and the results compared to undoped and HCl doped PANI. While for a routine coating of a substrate by ALD a rather short interaction of the vaporized precursor with the substrate surface is sufficient in order to chemically bind the molecule, the infiltration strategy relies on the extension of the exposure time and diffusion of the chemicals into subsurface areas. Therefore, we infiltrated samples applying short and long exposure times as well as samples coated with ZnO without infiltration. For this purpose, an initial layer of Al_2O_3 was deposited, which should act as an infiltration barrier for the DEZ. In addition, we surveyed samples with various numbers of infiltration cycles.

In Figure 5.2 (a) and (b) the room temperature I - V characteristics of the various PANI samples with similar thicknesses (7 ~ 10 μm) are displayed, showing linear, ohmic behavior. The electrical conductivity of the samples was calculated from the slopes of the I - V plots. Figure 5.2 (c) and Table 1 give an overview over the conductivities of the various investigated samples.

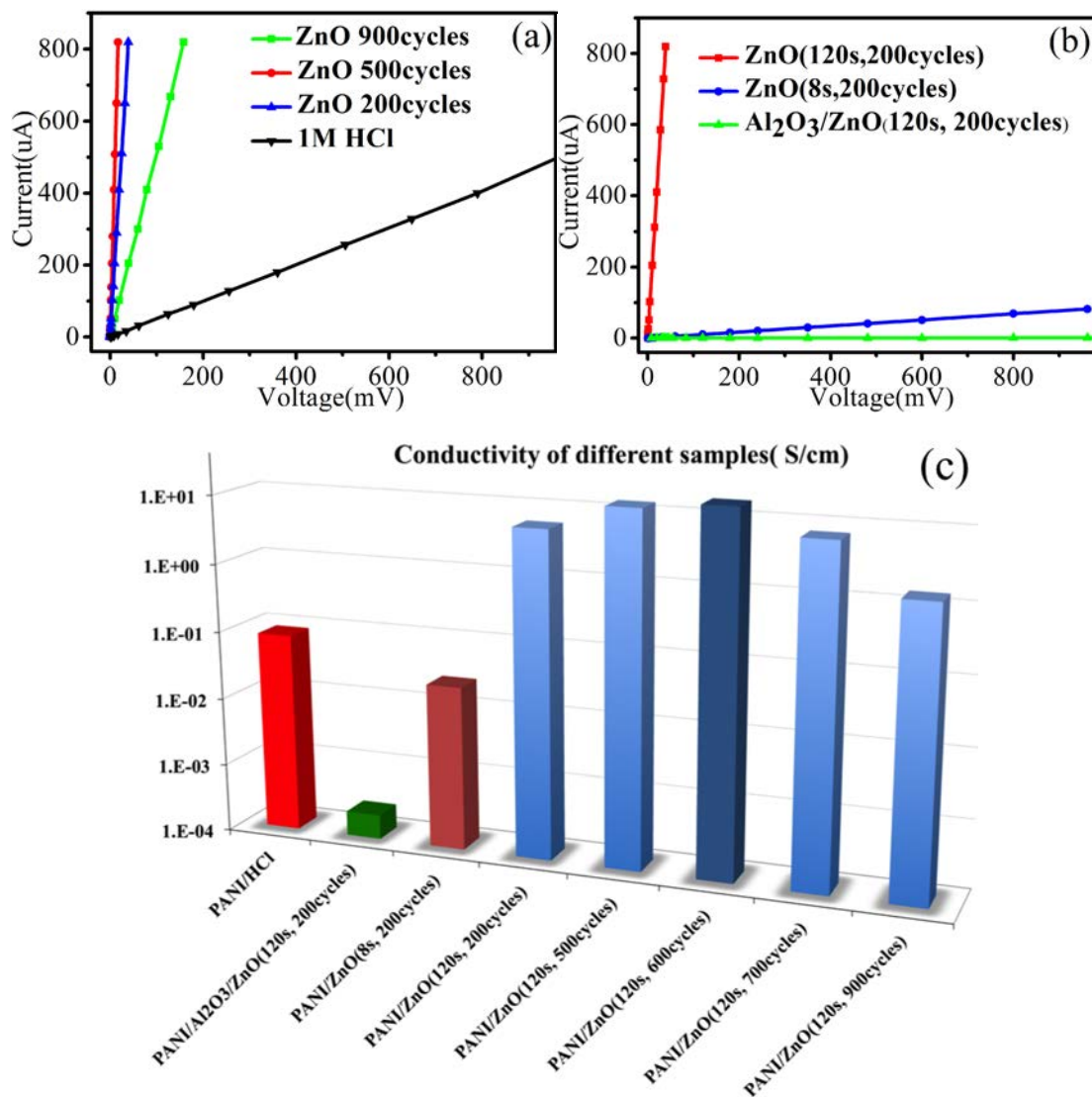


Figure 5.2 (a) *I-V* plots of PANI doped with 1M HCl (reference) and PANI doped with ZnO with variable numbers of infiltration cycles as indicated in the legend. The infiltration time for all the samples was 120 s per cycle. (b) *I-V* plots of PANI with a coating stack of Al₂O₃ (infiltration barrier)/ZnO, and PANI doped with ZnO applying short (8 s) and long (120 s) exposure times. The number of cycles in all samples was fixed to 200. (c) Comparison of conductivities of PANI after doping with HCl, coating with ZnO and infiltration with ZnO with varying exposure times and cycle numbers.

Table 1. Conductivities of the various fabricated samples (S/cm)

Sample	Exposure time (s)	Cycle number	Conductivity (S/cm)
PANI	-	-	$\leq 1 \times 10^{-10}$
PANI/1M HCl	-	-	$8.23 \times 10^{-2} \pm 1.82 \times 10^{-2}$
PANI/ZnO	8	200	$2.7 \times 10^{-2} \pm 2.93 \times 10^{-3}$
PANI/Al ₂ O ₃ /ZnO	120	200	$2.6 \times 10^{-4} \pm 3.0 \times 10^{-5}$
PANI/ZnO	120	200	6.58 ± 1.1
PANI/ZnO	120	500	15.05 ± 2.19
PANI/ZnO	120	600	18.42 ± 1.92
PANI/ZnO	120	700	7.42 ± 0.81
PANI/ZnO	120	900	1.64 ± 0.37

Untreated PANI thin films showed, as expected, no noteworthy conductivity. Also expected was the rise in conductivity observed after doping the samples with HCl from less than 10^{-10} S/cm to 8.23×10^{-2} S/cm. PANI that was coated with a double layer consisting of an Al₂O₃ infiltration barrier (thickness 1 ~ 2 nm) and a ZnO film onto showed a 2 orders of magnitude lower conductivity than observed from the HCl doped samples. The measured conductivity can be attributed to the ZnO shell on the surface of the substrate, since ALD deposited ZnO intrinsically shows conductivity¹⁹⁵. An infiltration process with rather short exposure times of 8 s resulted in conductivities similar to those of the HCl doped polymer. Considering the values obtained from the earlier described two samples, this ZnO infiltration process allows doping PANI with a similar efficiency as with HCl. With such short exposure times a rather narrow subsurface area of the polymer will be affected by the precursor vapors, which might be optimized with longer exposure times. Indeed, the conductivity increased greatly with an optimized ZnO infiltration process applying 120 s of exposure time, outperforming the film doped with 1M HCl by more than 2 orders of magnitude. Further conductivity increase up to 18.42 S/cm was achieved by altering the number of infiltration cycles with the 600 cycles process showing the strongest effect. Note that the observed conductivities are significantly higher than those observed with PANI/ZnO nanocomposites (up to 6.8×10^{-3} S/cm) produced with competing approaches^{192,193}. A further increase of the cycle numbers toward 700 and 900 lowered the conductivity, which might be due to mechanical cracking of the ZnO film as a result of internal stress that typically occurs with thicker coatings¹⁹⁵. It is worth noting that the PANI/ZnO samples were temporally very stable. Upon exposure to laboratory air for 6 months, the conductivities of PANI/ZnO (600 cycles) decreased by a factor of 3 - 4 only, that is from 18.42 S/cm to 5.67 S/cm (Figure 5.3).

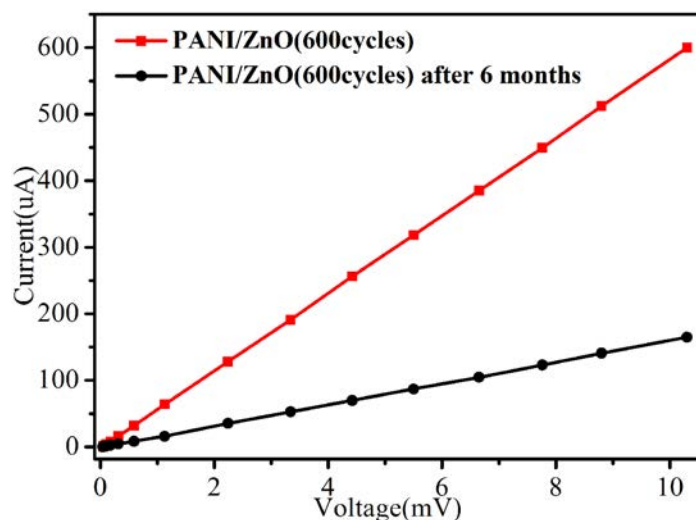


Figure 5.3 *I-V* plots of original PANI/ZnO (600 cycles) and PANI/ZnO (600 cycles) after storage in laboratory air for 6 months.

5.3.2 Electron Microscopy

The observation that both precoating PANI with an infiltration barrier or variation of the exposure times greatly affect the conductivity values implies that a strongly expressed synergistic effect is present. From the morphological point of view, the polymer did not show obvious differences after infiltration. In Figure 5.4 the scanning electron microscopy (SEM) images of PANI nanofibers before and after infiltration with ZnO (200 cycles) are shown. The structure remains preserved with slight variations in the fiber diameters, which result from unavoidable surface-deposited ZnO in such two-precursor infiltration processes. Transmission electron microscopy (TEM) and energy dispersive X-ray spectroscopy (EDS) scans of cross sections of such fibers showed a significant presence of Zn in the bulk of the material. The Zn may in form of ZnO contribute to the conductivity by allowing an electron hopping mechanism in principle, but given the large differences between the coated and infiltrated samples, it is more likely that the Zn interacts with the functional groups of the polymer in some way beneficial for the electron conduction. Such a scenario is also favored by the high resolution transmission electron microscopy (HRTEM) and selected area electron diffraction (SAED) analysis shown in the Figure 5.5. The interplanar spacings, as measured from SAED patterns, were 0.17 nm, 0.19 nm and 0.21 nm, corresponding to the (440), (431), and (332) planes of the *c*-zinc nitride structure¹⁹⁶. Further identified interplanar spacings of 0.15 nm and 0.21 nm correspond to the (103) and (101) planes of ZnO^{197,198}. The HRTEM images show the formation of crystallites within the polymers, which form a network with gaps on the nanometer or subnanometer scale between the crystallites. Thus it can be assumed

that the -Zn-N- or -N-Zn-O- bonds is an influencing factor for the conductivity of the resulting hybrid material.

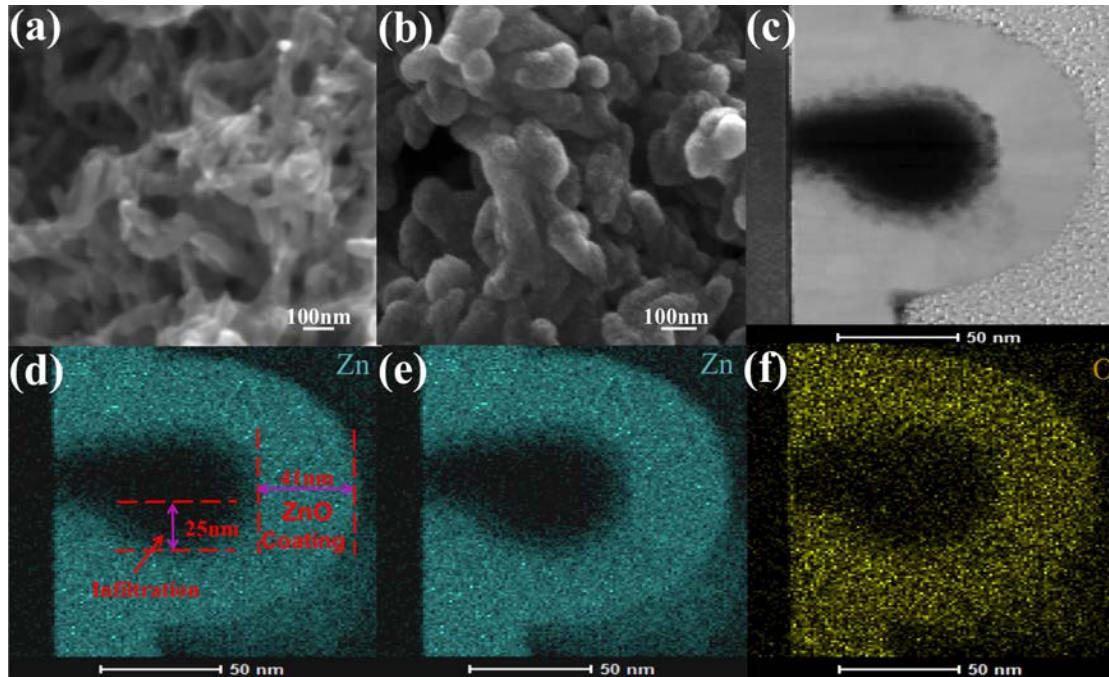


Figure 5.4 (a) and (b) SEM images of PANI and PANI/ZnO (120 s, 200 cycles). (c) TEM image of a cross-sectioned Zn infiltrated PANI fiber (PANI/ZnO, 120 s, 200 cycles), as prepared by the focused ion beam technique. (d) Zn elemental mapping of the cross-sectioned region. (e) Zn elemental mapping of the cross-sectioned region with Zn infiltration and ZnO coating label. (f) O elemental mapping of the cross-sectioned region.

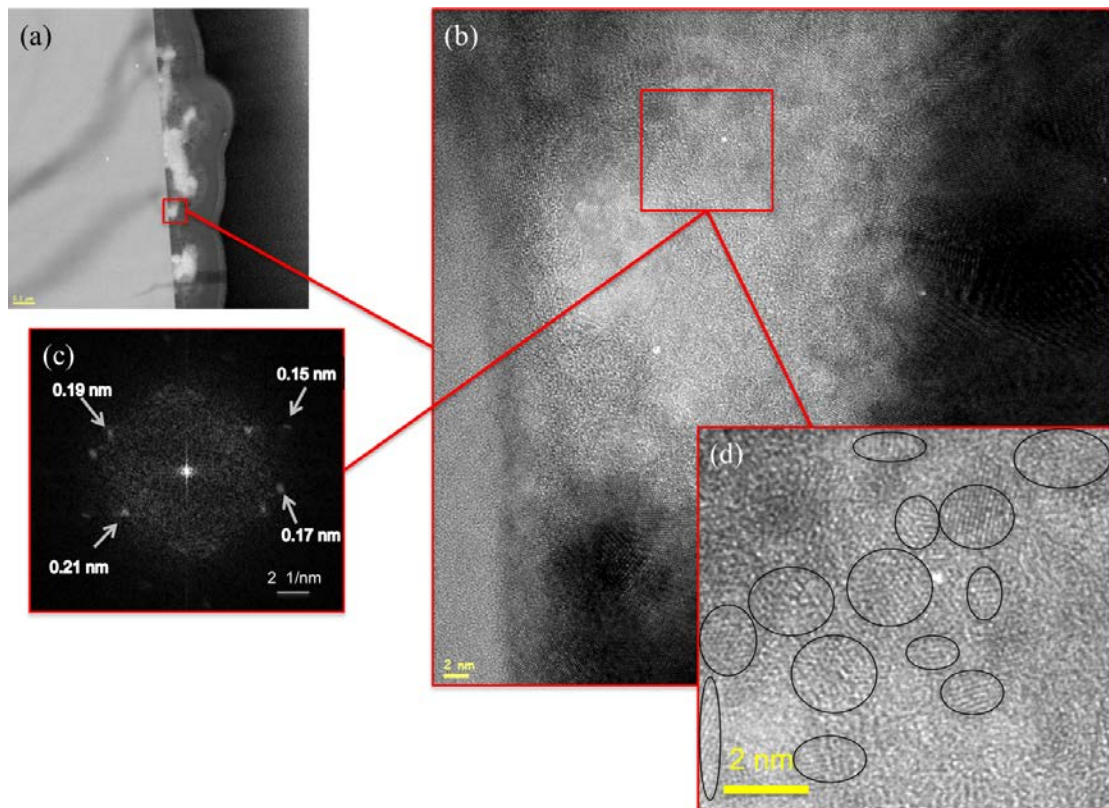


Figure 5.5 (a) and (b) TEM images of a cross-sectioned PANI/ZnO fiber (120 s, 200 cycles) with different magnification. (c) SAED patterns and (d) HRTEM image of the region marked with a red square in (b).

5.3.3 Infrared Spectra

The chemical functionalities in PANI, which allow binding with metal ions, are in the first instance the amine (-NH) and imine (-N=) groups. In typical infrared spectra, the bands at 1593 cm^{-1} (C=N stretching of quinoid units), 1300 cm^{-1} (N-H bending), 1220 cm^{-1} (C-N stretching of benzenoid units) and 829 cm^{-1} (out-of-plane C-H bending) are assigned to the emeraldine base structure. In our experiments, the infiltration process was performed with five cycles to minimize the amount of surface-deposited ZnO and in this way allow better observation of the chemical changes that occur in the polymer. Figure 5.6 shows that low temperature infiltrations ($80\text{ }^{\circ}\text{C}$ and $100\text{ }^{\circ}\text{C}$) did not result in obvious shifts of the aforementioned peaks. After increasing the temperature to $120\text{ }^{\circ}\text{C}$ and $140\text{ }^{\circ}\text{C}$ the bands at 1593 cm^{-1} and 1220 cm^{-1} shifted towards slightly higher wavenumbers. Upon further increase of the process temperature to $155\text{ }^{\circ}\text{C}$ and $180\text{ }^{\circ}\text{C}$, additionally the bands at 1300 cm^{-1} and 829 cm^{-1} shifted to 1292 cm^{-1} and 818 cm^{-1} . The band shifts at 1220 cm^{-1} and 1300 cm^{-1} can be attributed to the C-N⁺ stretching and indicate a true chemical modification of the PANI upon infiltration¹⁹⁹. This stands in contrast to previously reported PANI/ZnO composites, where the bands at 1300 cm^{-1} and 829 cm^{-1} showed opposite (blue) shift, whereas the band at 1220 cm^{-1} does not change¹⁹². The above results indicate a thermally activated chemical reaction of the polymer with the precursor vapors. At temperatures equal to or above $155\text{ }^{\circ}\text{C}$, the DEZ infiltrates the substrate and reacts with the amine and imine functional groups to form a new type of hybrid material. The effect of the infiltration on the chemical functionalities can be directly seen from the spectra in Figure 5.6 (b). With extended exposure times of 120 s (red graph), most significant peak shifts of the bands at 1593, 1300, 1220 and 829 cm^{-1} of the control sample (black) are observed. Specifically the shift of the peaks at 1300 cm^{-1} and 829 cm^{-1} is a signature for a fractional conversion of quinoid rings to benzenoid rings, which indicates an increased degree of charge delocalization in the PANI backbone. Reducing the exposure time from 120 s to 8 s (blue), results in negligible shifts of the same bands. Those minor shifts may be attributed to a reaction of DEZ with amine and imine groups positioned at the outer surface of PANI. Obviously extension of the exposure times favors an effective infiltration process. Prevention of infiltration by predeposition of an Al_2O_3 film appears to be a valid route, because neither the Al_2O_3 -coated process (cyan) nor the subsequently ZnO-processed (magenta) show significant differences to the control sample.

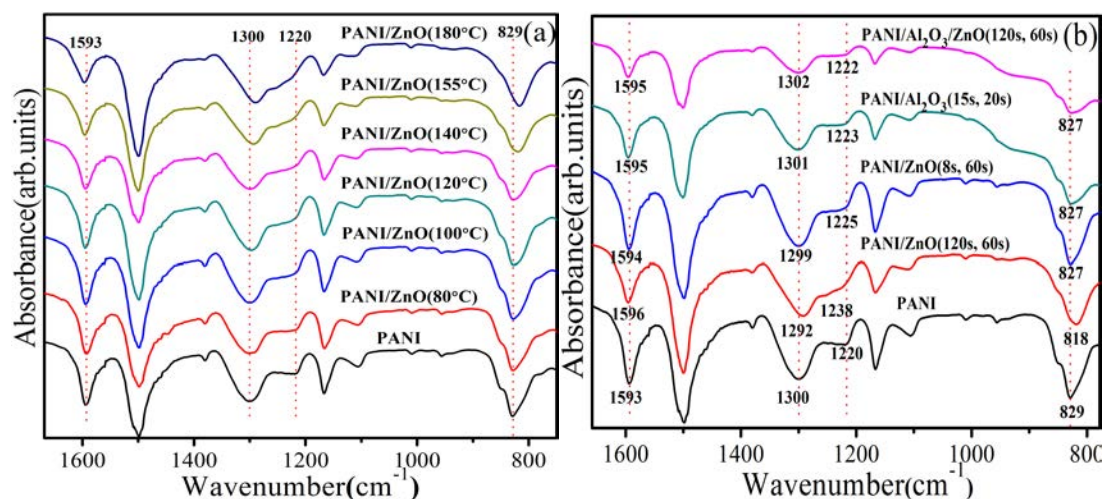


Figure 5.6 (a) FT-IR absorption spectra of PANI infiltrated with ZnO applying 120 s exposure time of PANI to DEZ and 5 infiltration cycles. PANI emeraldine base was used as reference (black) and infiltration was performed at various temperatures from 80 °C (red), 100 °C (blue), 120 °C (cyan), 140 °C (magenta), 155 °C (kaki) to 180 °C (dark-blue); (b) FT-IR absorption spectra of PANI processed at 155 °C with various process settings: PANI control sample (black), ZnO-infiltrated with 120 s exposure time and 5 processing cycles (red), ZnO-infiltrated with 8 s exposure time and 5 processing cycles (blue), PANI pre-coated with Al₂O₃ with exposure times of 15 s and 10 processing cycles (cyan) and Al₂O₃-coated PANI infiltrated with ZnO with 120 s exposure time and 5 processing cycles (magenta).

5.3.4 Raman Spectra

A similar picture can be drawn from further performed Raman spectroscopy investigations in Figure 5.7 (a), which showed the same trends as the FT-IR spectra. Additional information can be extracted from the newly appearing bands at 1354 cm⁻¹ and 1358 cm⁻¹, which are associated with the C-N vibrational A_{1g} mode. This mode was not observed in the control sample and indicates the formation of a bonding between Zn and N from PANI^{200,201}. Another remarkable change is the vanishing of the 1492 cm⁻¹ band along with the extension of the exposure time from 8 s to 120 s. This band is associated with the C=N stretching mode of the quinoid units and together with the shift of the C-C stretching band in the quinoid units at 1417 cm⁻¹ it indicates significant chemical modification of the quinoid fraction of the molecules. A blue shift of the 1168 cm⁻¹ band to 1183 cm⁻¹ after infiltration indicates a conversion of the mentioned quinoid groups to benzenoid groups, as the 1168 cm⁻¹ band is a signature of in-plane C-H bending of quinoid units, whereas the 1183 cm⁻¹ band is attributed to the same mode in benzenoid rings²⁰². A similar chemistry occurs

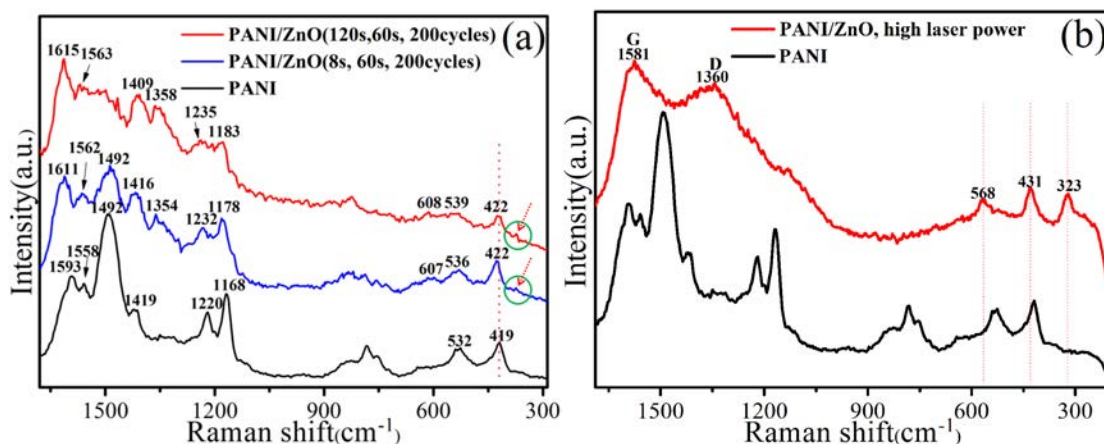


Figure 5.7 (a) Raman spectra of PANI (black), ZnO-infiltrated PANI with short exposure times (blue) and long exposure times (red) and process parameters as indicated in the figure; (b) Raman spectra of PANI control and PANI/ZnO (120 s, 60 s, 200 cycles, 155 °C) under high Raman laser power.

upon doping the insulating emeraldine base (EB) to the conductive emeraldine salt (ES). The Raman spectra further show the development of a small peak at 370 cm⁻¹, which becomes strongly pronounced with extended exposure times (red arrows in Figure 5.7 (a)), and a shift of the ring deformation peak at 419 cm⁻¹ to 422 cm⁻¹, likely due to an embedded new contribution slightly above 419 cm⁻¹. Both newly occurring peaks fall into the spectral range where Zn-N bonds are expected to be seen and also indicate the formation of Zn-N bonds²⁰³. In Figure 5.7 (b), with increasing the Raman laser power, we can detect the Raman spectra of ZnO at 568 cm⁻¹ (A₁ (LO) mode), 431 cm⁻¹ (E₂ mode) and 323 cm⁻¹ (2E₂(M))^{204,205}. The Raman bands at 1360 cm⁻¹ and 1581 cm⁻¹ are assigned to D - (disordered) and G - (graphitic) bands associated with the carbon-related defect complex, respectively. These bands are characteristic for amorphous carbon materials²⁰⁶, which demonstrates the decomposition of the PANI structure under high Raman laser power.

5.3.5 X-ray diffraction

The infiltration of PANI with DEZ obviously induces a chemical reaction of the precursor and the imine and amine groups of the polymer. In this course quinoid groups are converted into benzenoid groups, which is similar to the result of doping the insulating emeraldine base to the conductive emeraldine salt. Indeed, the characterization of the infiltrated polymer by X-ray diffraction (XRD) shows a peak at $2\theta=27.6^\circ$ (red arrow in

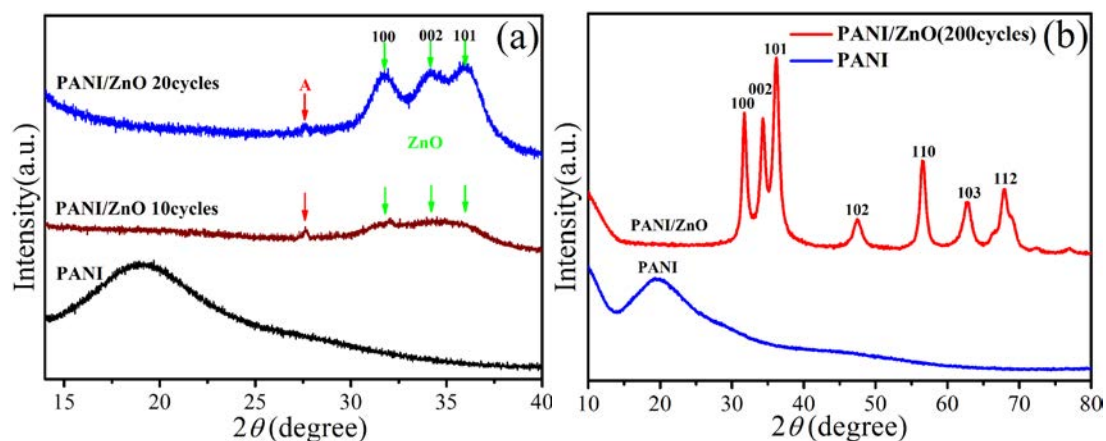


Figure 5.8 (a) XRD spectra of PANI before and after infiltration with ZnO. (b) XRD patterns of different samples, PANI control and PANI/ZnO (120 s, 60 s, 200 cycles, 155 °C).

Figure 5.8 (a), the origin of which is neither ZnO nor the emeraldine base of PANI. It can rather be assigned to the (111) reflection that is usually observed in acid doped PANI salts²⁰⁷. We chose a low number of cycles for identifying this peak, because a larger number of cycles result in more surface deposited ZnO and the resulting signal intensity increases thus losing the sensitivity for this particular signal. As shown in Figure 5.8 (b), after 200 cycles ZnO infiltration process, the characteristic peaks of PANI/ZnO appear at 31.76, 34.3, 36.21, 47.43, 56.5, 62.81 and 67.85° which can be indexed to the hexagonal wurtzite structure of ZnO²⁰⁸. No further phases or impurities are visible.

5.3.6 X-ray Photoelectron Spectra

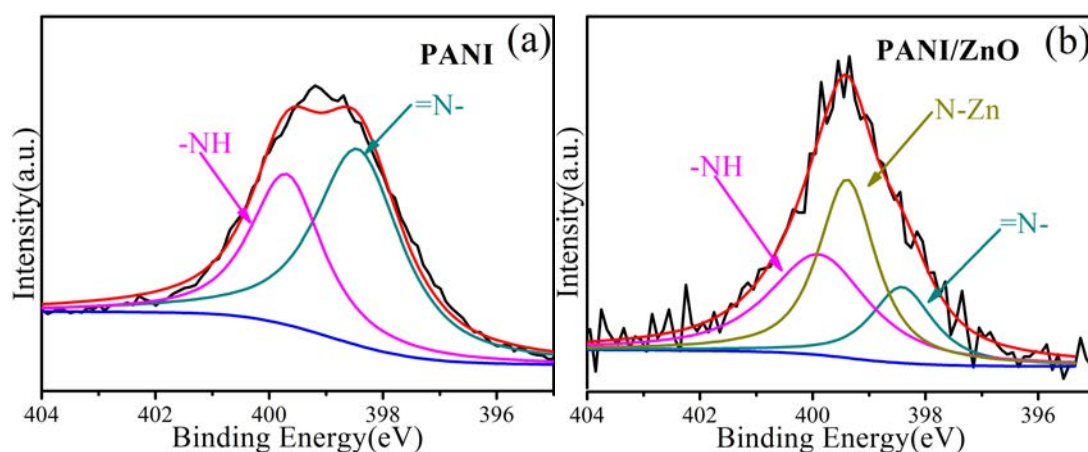


Figure 5.9 (a) N 1s XPS spectrum of PANI; (b) N 1s XPS spectrum of PANI infiltrated with ZnO with 120 s exposure time and 5 processing cycles.

To gain a better understanding of the complicated chemistry changes during the vapor phase infiltration process, X-ray photoelectron spectroscopy (XPS) was used, which is very surface sensitive. Thick ZnO shells would result in characterizing the coating instead of PANI, therefore we characterized PANI and ZnO-infiltrated PANI after 5 infiltration cycles only (120 s, five cycles), on a silicon wafer with focus on nitrogen and its bonding properties. PANI showed a nearly symmetric N 1s line centered around 399 eV (Figure 5.9 (a)). This N 1s core spectrum level of the line can be deconvoluted into two peaks with equal intensity, one centered at 398.44 eV and the other at 399.71 eV. These can be assigned to the two chemically distinct nitrogen types in imine (=N-) and amine (-NH-) present in the emeraldine base (EB) form of PANI²⁰⁹. After five ZnO infiltration cycles, two noticeable changes are seen in Figure 5.9 (b). Namely, a new component appearing at 399.39 eV (moss green curve), which can be assigned to a coordination of the type Zn-N²¹⁰, and the peak intensity of imine and amine type nitrogen significantly decreasing, indicating a consumption of a part of the imine and amine units.

The above characterization confirms that the PANI is indeed modified upon infiltration with ZnO. This chemical modification can be considered as a highly efficient alternative way of doping PANI. However, the mechanism of doping is to a great extent different to the common doping schemes. Traditionally, PANI is doped with Brønsted acids such as HCl or similar. Such acids protonate imine sites and create bipolarons that subsequently delocalize. In an alternative procedure, Lewis acids are applied that bind to the nitrogen and in this way fulfill the same task. In the present case DEZ, which is a Lewis acid, is used as one of the precursors, which implies a similar doping scheme to the common Lewis acid processes. However, upon treatment with DEZ only, that is, without the use of the counter precursor H₂O, the conductivity of the infiltrated PANI did not rise. Similarly, the use of trimethylaluminum (TMA), which is an even stronger Lewis acid than DEZ and the most common precursor for ALD depositions of Al₂O₃, did not increase the conductivity of the PANI either. Thus, the water pulses play an important role for the conductivity increase. The process setup with long exposure times and alternating pulses of DEZ and water results in the subsurface growth of ZnO. Composite materials of ZnO nanoparticles and acid doped PANI have been fabricated before, but their conductivities varied from 1.4×10^{-3} S/cm to 6.8×10^{-3} S/cm^{192,193} and were significantly lower than the conductivities achieved with the infiltration strategy. Therefore, additional factors must play a role here. It is intrinsic to the ALD process that the precursor binds covalently to the polymer backbone, which indicates that such grown ZnO adds value to the conductivities of both components, the ZnO and the PANI, beyond a simple additive value. The analysis of the spectra shows that Zn is bound to the nitrogen in the polymer chain, whereas the need of applying water pulses at the same time points towards the necessity of the formation of ZnO. While ALD deposited ZnO may not be the source for

the significant increase of the conductivity upon infiltration, the formation of a ZnON type inorganic phase that is covalently linked to Lewis acid doped PANI is proposed to be the real origin. In other words, the resulting material can be seen from two perspectives, a Lewis-acid-doped PANI and an N-doped ZnO that form an interpenetrated hybrid network. Such a network provides additional conduction paths through the cross-linking bonds between the polymer chains and the ZnO, while at the same time both components mutually lower each other component's band gap. In fact, doping of ZnO with nitrogen is reported to reduce the band gap of the material from 3.4 eV to values between 1 and 2 eV, depending on the doping level²¹¹. The dopant nitrogen in our system stems from the amine and imine groups of PANI, which upon binding to ZnO becomes oxidized and thus forms the doped units of the PANI backbone. This model is supported by the UV-vis absorption spectra shown in Figure 5.10. After infiltration, a new shoulder appears at 403 nm, which with 3.08 eV is much lower than the band gap of ZnO. The band intensity at 453 nm, which corresponds to the $\pi - \pi^*$ transitions in the benzenoid rings, increases, and the band at 625 nm, corresponding to the quinoid rings, almost disappears due to the conversion of quinoid rings into the benzenoid rings (polaron state). No obvious free-carrier tail was observed in the near-infrared region of the UV-vis spectra²¹². This indicates that PANI cannot be considered as a dominant charge promoter, but the hybrid system has to be considered as a whole. The N atoms donate electrons to the Zn atoms forming holes in the PANI main chain, which becomes a p-type semiconductor. ZnO is an n-type semiconductor, but the interfacial N-doped ZnO is known to be a p-type semiconductor, which results in a constellation similar to local p-n heterojunctions, which are dispersed over the whole system. Consequently, ZnO can drain the charge carriers from the PANI and no free-carrier tail is expected to occur. Therefore, a resulting reaction scheme, as depicted in Figure 5.11 can be proposed.

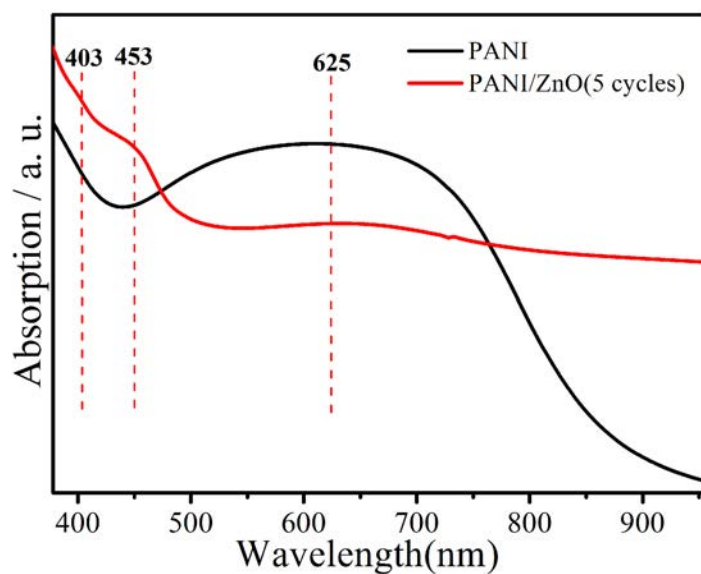


Figure 5.10 UV-Vis absorption spectra of PANI (black) and ZnO-infiltrated PANI applying 5 infiltration cycles and 120 s exposure time at 155 °C.

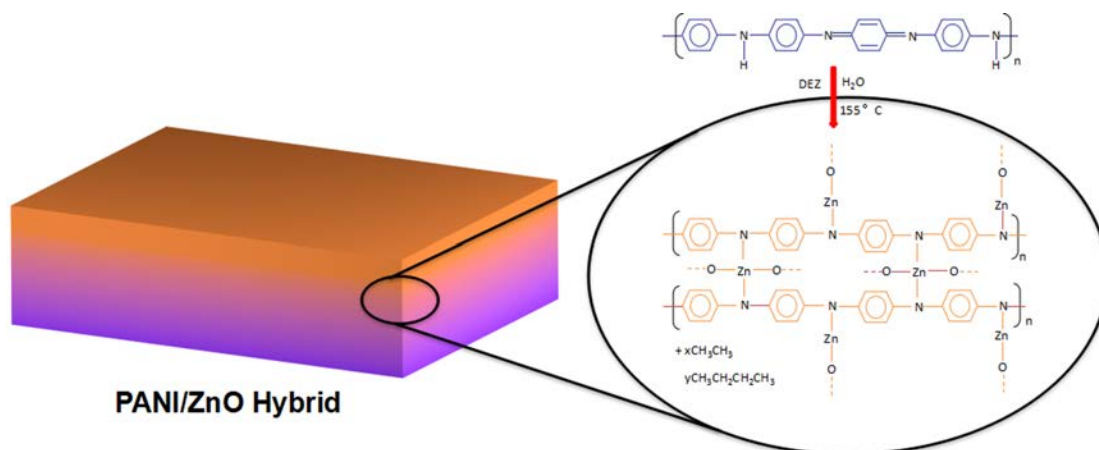


Figure 5.11 Macroscopic view on the hybrid material with covalently linked N-doped ZnO and Lewis acid doped PANI. Idealized schematic view of the chemical binding of Zn to the PANI backbone upon infiltration. The polymer chains become cross-linked with Zn-N bonds, while at the same time quinoid groups become benzenoid groups.

5.4 Conclusion

Infiltration of polyaniline with ZnO from the vapor phase is an effective novel pathway for enhancing the conductivity of the resulting hybrid material. The increase in conductivity

that is observed after successful processing goes significantly beyond the additive contribution to the conductivity provided by the individual components. The reason for such improvement is considered to lie in a synergistic mutual doping of both the inorganic and the polymeric constituent of the hybrid material. Vapor phase infiltration enforces binding of Zn to the nitrogen present in the polymer backbone, which induces Lewis acid type of doping of PANI, whereas at the same time the ZnO becomes doped with nitrogen. The interpenetrated network further provides additional conduction pathways through cross-linking of the polymer chains with the inorganic material, additionally contributing to an enhanced conductivity. Although the process was demonstrated on one particular substrate-precursor system, the principle may be extended to further material couples as well. While a large variety of semiconducting polymers, all of which contain functional chemical groups of different types, is available, the vapor phase infiltration process can easily be applied for the development of a plethora of further material combinations.

Chapter 6

Summary and Outlook

This thesis presents strategies for the ALD-derived vapor phase infiltration (VPI) and doping process of the conducting polymers polyaniline (PANI) and poly(3-hexyl)thiophene (P3HT). It can be divided into three parts: 1) single precursor (MoCl_5 or SnCl_4) vapor phase infiltration and doping of PANI; 2) single precursor (MoCl_5) vapor phase infiltration and doping of P3HT; 3) multiple pulsed (diethylzinc (DEZ) and H_2O) vapor phase infiltration and doping of PANI.

In the first part, a novel way of doping PANI by an ALD-derived single precursor VPI process was successfully demonstrated. This way not only allows to enhance the conductivity of PANI by up to 6 orders of magnitude, but also to control the conductivity through the choice and amount of the infiltrated precursor. More importantly, the conductivity of the PANI doped in our way was barely affected by the thermal treatment at 150 °C in vacuum, while the conductivity of the 1M HCl doped PANI was almost completely lost. This loss is due to a deprotonation of the doped PANI and resulting evaporation of HCl. Doping with MoCl_5 or SnCl_4 can result in an oxidation of the PANI and very likely in a complexation of the metal chlorides with the nitrogen in PANI. As a result, the electron mobility along the polymer chains was significantly enhanced and the structure was stabilized even at elevated temperatures.

In the second part, the ALD-derived single precursor VPI process was used to dope the conducting polymer P3HT. After the MoCl_5 infiltration process, the conductivity of P3HT rose up to 5 orders of magnitude. The P3HT/ MoCl_5 thin film showed exceptional stability under ambient conditions, largely outperforming the stability of the reported doped P3HT/FTS. Doping with MoCl_5 from the vapor phase results in a local oxidation of the P3HT. The lone electron pairs at the sulfur atoms of the thiophene rings in P3HT can donate negative charge to the MoCl_5 with themselves becoming rather positively charged. The results are not only significant for the novel process to dope P3HT and obtain better stability, but also for the possibility of performing top-down doping of already pre-manufactured P3HT, which allows for better shaping of the material and therefore more efficient device fabrication.

In the last part, the multiple pulsed (DEZ and H₂O) vapor phase infiltration and doping of PANI was studied. The infiltration of PANI with ZnO from the vapor phase is an effective novel pathway for increasing the conductivity of the resulting hybrid material. The increase in conductivity was up to 3 orders of magnitude higher than upon conventional doping with 1 M HCl in wet chemical ways. The reason for the conductivity improvement is likely due to a synergistic mutual doping of both the inorganic and the organic polymeric constituent of the hybrid material. Vapor phase infiltration enforces binding of Zn to the nitrogen present in the polymer backbone, which induces Lewis acid type of doping of PANI, while at the same time the ZnO becomes doped with nitrogen. The interpenetrated network further provides additional conduction pathways through crosslinking of the polymer chains with inorganic material, which results in the increased conductivity.

In conclusion, for avoiding the negative influence of the wet chemical doping approaches, the research performed in this thesis successfully demonstrated a novel way of doping conducting polymers, by applying an ALD-derived vapor phase infiltration (VPI) and doping process. The VPI process not only allows efficient control in the doping level, but also allows solvent-free processing and even top-down doping of already manufactured and shaped conducting polymers. It can be foreseen that the results presented in this work will be further improved in future work, considering the vast amount of conductive polymers known and the equally vast amount of ALD processes that are developed and can be used for an infiltration process. The present work may therefore act as seminal work for future developments of conductive polymers.

Bibliography

- (1) MacDiarmid, A. G. "Synthetic Metals": A Novel Role for Organic polymers (Nobel lecture). *Angew. Chem. Int. Ed.* **2001**, *40*, 2581–2590.
- (2) Li, Y. F. Organic Optoelectronic Materials. *Lecture Notes in Chemistry* **2015**, *91*, ISBN 978-3-319-16862-3.
- (3) Chiang, C. K.; Fincher, C. R.; Park, Y. W.; Heeger, A. J.; Shirakawa, H.; Louis, E. J.; Gau, S. C.; MacDiarmid, A. G. Electrical Conductivity in Doped Polyacetylene. *Phys. Rev. Lett.* **1977**, *39*, 1098-1101.
- (4) Chiang, C. K.; Druy, M. A.; Gau, S. C.; Heeger, A. J.; Louis, E. J.; MacDiarmid, A. G.; Park, Y. W.; Shirakawa, H. Synthesis of Highly Conducting Films of Derivatives of Polyacetylene, (CH)_x. *J. Am. Chem. Soc.*, **1978**, *100*, 1013–1015.
- (5) Handbook of Organic Conductive Materials and Polymers (Ed.: H. S. Nalwa), Wiley, New York, 1997; Handbook of Conducting Polymers (Ed.: T. A. Skotheim, R. L. Elsenbaumer, J. F. Reynolds), 2nd ed., Marcel Dekker, New York, 1998.
- (6) Yu, G.; Gao, J.; Hummelen, J. C.; Wudl, F.; Heeger, A. J. Polymer Photovoltaic Cells: Enhanced Efficiencies via a Network of Internal Donor-Acceptor Heterojunctions. *Science* **1995**, *270*, 1789-1791.
- (7) Zhao, W., Qian, D., Zhang, S., Li, S., Inganäs, O., Gao, F. and Hou, J. Fullerene-free polymer solar cells with over 11% efficiency and excellent thermal stability. *Adv. Mater.* **2016**, *28*, 4734–4739.
- (8) Vandewal, K., Widmer, J., Heumueller, T., Brabec, C. J., McGehee, M. D., Leo, K., Riede, M. and Salleo, A. Increased open-circuit voltage of organic solar cells by reduced donor-acceptor interface area. *Adv. Mater.* **2014**, *26*, 3839–3843.
- (9) Poelking, C., Tietze, M., Elschner, C., Olthof, S., Hertel, D., Baumeier, B., Wurthner, F.; Meerholz, K.; Leo, K.; Andrienko, D. Impact of mesoscale order on open-circuit voltage in organic solar cells. *Nat. Mater.* **2014**, *14*, 434–439.
- (10) Tang, C. W. Two-layer organic photovoltaic cell. *Appl. Phys. Lett.* **1986**, *48*, 183–185.
- (11) Cao, W. R.; Xue, J. G. Recent progress in organic photovoltaics: device architecture and optical design. *Energy Environ. Sci.*, **2014**, *7*, 2123-2144
- (12) Kippelen, B.; Brédas, J. L. Organic photovoltaics. *Energy Environ. Sci.*, **2009**, *2*, 251-261.
- (13) Bundgaard, E.; Krebs, F. C. Low band gap polymers for organic photovoltaics. *Solar Energy Materials and Solar Cells*, **2007**, *91*, 954-985.
- (14) Hu, L. B.; Gruner, G.; Li, D.; Kaner, R. B.; Cech, J. Patternable transparent carbon nanotube films for electrochromic devices. *J. Appl. Phys.* **2007**, *101*, 016102.

- (15) Tsai, T. S.; Pillay, V.; Choonara, Y. E.; Toit, L. C.; Modi, G.; Naidoo, D.; Kumar, P. A Polyvinyl Alcohol-Polyaniline Based Electro-Conductive Hydrogel for Controlled Stimuli-Actuable Release of Indomethacin. *Polymers* **2011**, *3*, 150-172.
- (16) Anderson, M. R.; Mattes, B. R.; Reiss, H.; Kaner, R. B. Conjugated Polymer Films for Gas Separation. *Science* **1991**, *252*, 1412-1415.
- (17) Huang, J. X.; Virji, S.; Weiller, B. H.; Kaner, R. B. Polyaniline Nanofibers: Facile Synthesis and Chemical Sensors. *J. Am. Chem. Soc.* **2003**, *125*, 314–315.
- (18) Li, D.; Mueller, M. B.; Gilje, S.; Kaner, R. B.; Wallace, G. G. Conjugated Polymer-based chemical sensors. *Chem. Rev.* **2000**, *100*, 2537-2574.
- (19) Huang, J.; Virji, S.; Weiller, B. H.; Kaner, R. B. Nanostructured Polyaniline Sensors. *Chem. - Eur. J.* **2004**, *10*, 1315–1319.
- (20) Karami, H.; Mousavi, M. F.; Shamsipur, M. A new design for dry polyaniline rechargeable batteries. *Journal of Power Sources*, **2003**, *117*, 255-259.
- (21) MacDiarmid, A. G.; Yang, L. S.; Huang, W. S.; Humphrey, B. D. Polyaniline: Electrochemistry and application to rechargeable batteries. *Synthetic Metals*, **1987**, *18*, 383-398.
- (22) Zhou, Q.; Shi, G. Conducting Polymer-Based Catalysts. *J. Am. Chem. Soc.* **2016**, *138*, 2868–2876.
- (23) Shi, Y., Peng, L.; Ding, Y.; Zhao, Y.; Yu, G. Nanostructured Conductive Polymers for Advanced Energy Storage. *Chem. Soc. Rev.*, **2015**, *44*, 6684-6696.
- (24) Das, D.; Datta, A.; Contractor, A. Q. Doping of Polyaniline with 6-Cyano-2-naphthol. *J. Phys. Chem. B* **2014**, *118*, 12993–13001.
- (25) Li, D.; Huang, J. X.; Kaner, R. B. Polyaniline Nanofibers: A Unique Polymer Nanostructure for Versatile Applications. *Accounts of Chemical Research*, **2009**, *42*, 135-145.
- (26) Groenendaal, L.; Jonas, F.; Freitag, D.; Peilartzik, H.; Reynolds, J. R. Poly(3,4-ethylenedioxythiophene) and Its Derivatives: Past, Present, and Future. *Adv. Mater.*, **2000**, *12*, 481–494.
- (27) Cao, Y.; Yu, G.; Menon, R.; Heeger, A. J. Polymer Light-emitting Diodes with Polyethylene Dioxythiophene–polystyrene Sulfonate as the Transparent Anode. *Synthetic Metals*, **1997**, *87*, 171-174.
- (28) Lang, U.; Müller, E.; Naujoks, N.; Dual, J. Microscopical Investigations of PEDOT:PSS Thin Films. *Adv. Funct. Mater.*, **2009**, *19*, 1215–1220.
- (29) Kim, J. Y.; Jung, J. H.; Lee, D. E.; Joo, J. Enhancement of Electrical Conductivity of Poly(3,4-ethylenedioxythiophene)/Poly(4-styrenesulfonate) by a Change of Solvents. *Synth. Met.* **2002**, *126*, 311-316.
- (30) Nardes, A. M.; Janssen, R. A. J.; Kemerink, M. A Morphological Model for the Solvent-Enhanced Conductivity of PEDOT:PSS Thin Films. *Adv. Funct. Mater.*, **2008**, *18*, 865–871.

- (31) Dobbelin, M.; Marcilla, R.; Salsamendi, M.; Pozo-Gonzalo, C.; Carrasco, P. M.; Pomposo, J. A.; Mecerreyes, D. Influence of Ionic Liquids on the Electrical Conductivity and Morphology of PEDOT:PSS Films. *Chem. Mater.*, **2007**, *19*, 2147–2149.
- (32) Xia, Y.; Ouyang, J. Significant Conductivity Enhancement of Conductive Poly(3,4-ethylenedioxythiophene): Poly(styrenesulfonate) Films through a Treatment with Organic Carboxylic Acids and Inorganic Acids. *ACS Appl. Mater. Interfaces*, **2010**, *2*, 474–483.
- (33) Kim, Y. H.; Sachse, C.; Machala, M. L.; May, C.; Müller-Meskamp, L.; Leo, K. Highly Conductive PEDOT:PSS Electrode with Optimized Solvent and Thermal Post-Treatment for ITO-Free Organic Solar Cells. *Adv. Funct. Mater.*, **2011**, *21*, 1076–1081.
- (34) Xia, Y.; Ouyang, J. Anion Effect on Salt-induced Conductivity Enhancement of Poly(3,4-ethylenedioxythiophene):poly(styrenesulfonate) Films. *Organic Electronics* **2010**, *11*, 1129–1135.
- (35) Xia, Y.; Sun, K.; Ouyang, J. Highly Conductive Poly(3,4-ethylenedioxythiophene):poly(styrene sulfonate) Films Treated with an Amphiphilic Fluoro Compound as the Transparent Electrode of Polymer Solar Cells. *Energy Environ. Sci.*, **2012**, *5*, 5325–5332.
- (36) Alemu, D.; Wei, H. Y.; Ho, K. C.; Chu, C. W. Highly Conductive PEDOT:PSS Electrode by Simple Film Treatment with Methanol for ITO-free Polymer Solar Cells. *Energy Environ. Sci.*, **2012**, *5*, 9662–9671.
- (37) Xia, Y.; Ouyang, J. Significant Different Conductivities of the Two Grades of Poly(3,4-ethylenedioxythiophene):Poly(styrenesulfonate), Clevios P and Clevios PH1000, Arising from Different Molecular Weights. *ACS Appl. Mater. Interfaces*, **2012**, *4*, 4131–4140.
- (38) Xia, Y.; Sun, K.; Ouyang, J. Solution-Processed Metallic Conducting Polymer Films as Transparent Electrode of Optoelectronic Devices. *Adv. Mater.*, **2012**, *24*, 2436–2440.
- (39) Wang, G. M.; Swensen, J.; Moses, D.; Heeger, A. J. Increased Mobility from Regioregular Poly(3-hexylthiophene) Field-effect Transistors. *Journal of Applied Physics* **2003**, *93*, 6137–6141.
- (40) Moreas, F.; Schaffer, H.; Kobayashi, M.; Heeger, A. J.; Wudl, F. Photoexcitations in Poly(thiophene): Photoinduced Infrared Absorption and Photoinduced Electron-spin Resonance. *Phys. Rev. B* **1984**, *30*, 2948–2950.
- (41) Sirringhaus, H.; Brown, P. J.; Friend, R. H.; Nielsen, M. M.; Bechgaard, K.; Langeveld-Voss, B. M. M.; Spiering, A. J. H.; Janssen, R. A. J.; Meijer, E. W.; Herwig, P.; de Leeuw, D. M. Two-dimensional Charge Transport in Self-organized, High-mobility Conjugated Polymers. *Nature* **1999**, *401*, 685–688.
- (42) Sterbacka, R. O.; An, C. P.; Jiang, X. M.; Vardeny, Z. V. Two-Dimensional Electronic Excitations in Self-Assembled Conjugated Polymer Nanocrystals. *Science* **2000**, *287*, 839–842.
- (43) Bredas, J. L.; Street, G. B. Polarons, Bipolarons, and Solitons in Conducting Polymers. *Acc. Chem. Res.*, **1985**, *18*, 309–315.
- (44) Roth, S.; Carroll, D. One Dimensional Metals, Second Edition. WILEY-VCH Verlag GmbH & Co. KGaA, Weinheim, 2004. ISBN: 3-527-30794-4.

- (45) Stafstrom, S.; Chao, K. A. Soliton States in Polyacetylene. *Physical Review B* **1984**, *29*, 2255-2266.
- (46) Su, W. P.; Schrieffer, J. R. Soliton Dynamics in Polyacetylene. Proceedings of the National Academy of Sciences of the United States of America **1980**, *77*, 5626-5629.
- (47) Heeger, A. J. Semiconducting and Metallic Polymers: The Fourth Generation of Polymeric Materials. *J. Phys. Chem. B*, **2001**, *105*, 8475-8491.
- (48) Sze, S. M. & Ng, K. K. Physics of Semiconductor Devices (Wiley-Interscience, 2006).
- (49) Méndez H.; Heimel G.; Winkler S.; Frisch J.; Opitz A.; Sauer K.; Wegner B.; Oehzelt M.; Röthel C.; Duhm S.; Töbrens D.; Koch N.; Salzmann I. Charge-transfer Crystallites as Molecular Electrical Dopants. *Nature Communications*, **2015**, *6*:8560.
- (50) Chiang, C. K.; Gau, S. C.; Fincher, C. R.; Park, Y. W.; MacDiarmid, A. G.; Heeger, A. J. *Appl. Phys. Lett.* **1978**, *33*, 18.
- (51) Shirakawa, H.; Louis, E. J.; MacDiarmid, A. G.; Chiang, C. K.; Heeger, A. J. Synthesis of Electrically Conducting Organic Polymers: Halogen Derivatives of Polyacetylene, (CH)_x. *J. Chem. Soc., Chem. Commun.*, **1977**, *16*, 578-580.
- (52) Ziemelis, K. E.; Hussain, A. T.; Bradley, D. D. C.; Friend, R. H.; Rühle, J.; Wegner, G. Optical Spectroscopy of Field-induced Charge in Poly(3-hexyl thienylene) Metal-insulator-semiconductor Structures: Evidence for Polarons. *Phys. Rev. Lett.* **1991**, *66*, 2231
- (53) *Handbook of Conducting Polymers, Vol 1&2* (Ed.: T. A. Skotheim) Marcel Dekker, New York, 1986.
- (54) Kanatzidis, M. G. Conductive Polymers, *Chem. Eng. News* **1990**, *68*, 36-50.
- (55) Nigrey, P. J.; MacDiarmid, A. G.; Heeger, A. J. Electrochemistry of Polyacetylene, (CH)_x: Electrochemical Doping of (CH)_x films to the Metallic State. *Chem. Commun.* **1979**, *96*, 594-595.
- (56) MacInnes, D.; Druy, M. A.; Nigrey, P. J.; Nairns, D. P.; MacDiarmid, A. G.; Heeger, A. J. Organic Batteries: Reversible *n*- and *p*- Type Electrochemical Doping of Polyacetylene, (CH)_x. *J. Chem. Soc. Chem. Commun.* **1981**, *7*, 317-319.
- (57) Salaneck, W. R.; Lundstrom, I.; Haung, W. S.; MacDiarmid, A. G. A Two-Dimensional-surface 'State Diagram' for Polyaniline. *Synth. Met.* **1986**, *13*, 291-297.
- (58) Chiang, J. C.; MacDiarmid, A. G. Polyaniline': Protonic acid doping of the emeraldine form to the metallic regime. *Synth. Met.* **1986**, *13*, 193-205.
- (59) MacDiarmid, A. G.; Epstein, A. J. Polyanilines: a novel class of conducting polymers. *Faraday Discuss. Chem. Soc.* **1989**, *88*, 317-332.
- (60) MacDiarmid, A. G.; Epstein, A. J. *Science and Applications of Conducting Polymers* (Eds.: W. R. Salaneck, D. T. Clark, E. J. Samuelsen), Adam Hilger, Bristol, **1990**, p. 117.
- (61) MacDiarmid, A. G.; Epstein, A. J. *In Conjugated Polymeric Materials: Opportunities in Electronics, Optical Electronics and Molecular Electronics*; Bredasand, J. L., Chance, R. R., Eds.; Kluwer Academic Publishers: Dordrecht, The Netherlands, **1990**, p. 53.

- (62) Wudl, F.; Angus, R. O.; Lu, F. L.; Allemand, P. M.; Vachon, D. J.; Nowak, M.; Liu, Z. X.; Heeger, A. J. Poly-p-phenyleneamineimine: Synthesis and Comparison to Polyaniline. *J. Am. Chem. Soc.* **1987**, *109*, 3677-3684.
- (63) Heeger, A. J.; Kivelson, S.; Schrieffer, J. R.; Su, W. P. Solitons in conducting polymers. *Rev. Mod. Phys.* **1988**, *60*, 781-849.
- (64) Burroughes, J. H.; Jones, C. A.; Friend, R. H. New Semiconductor Device Physics in Polymer Diodes and Transistors. *Nature* **1988**, *335*, 137-141.
- (65) Burroughes, J. H.; Bradley, D. D. C.; Brown, A. R.; Marks, R. N.; Mackay, K.; Friend, R. H.; Burns, P. L.; Holmes, A. B. Light-emitting Diodes Based on Conjugated Polymers. *Nature* **1990**, *347*, 539-541.
- (66) Adinolfi, V.; Sargent, E. H. Photovoltage Field-effect Transistors. *Nature* **2017**, *542*, 324-327.
- (67) Tsao, H. N.; Cho, D. M.; Park, I.; Hansen, M. R.; Mavrin, A. Ultrahigh Mobility in Polymer Field-Effect Transistors by Design. *J. Am. Chem. Soc.*, **2011**, *133*, 2605-2612.
- (68) Knopfmacher, O.; Hammock, M. L.; Appleton, A. L.; Schwartz, G.; Mei, J.; Lei, T.; Pei, J.; Bao, Z. Highly Stable Organic Polymer Field-effect Transistor Sensor for Selective Detection in the Marine Environment. *Nat Commun.* **2014**, *5*:2954.
- (69) Chang, M. H.; Das, D.; Varde, P.V.; Pecht, M. Light Emitting Diodes Reliability Review. *Microelectronics Reliability* **2012**, *52*, 762-782.
- (70) Kalyani, N. T.; Dhoble, S. J. Organic Light Emitting Diodes: Energy Saving Lighting Technology—A review. *Renewable and Sustainable Energy Reviews* **2012**, *16*, 2696-2723.
- (71) Jou, J. H.; Kumar, S.; Agrawal, A.; Li, T. H.; Sahoo, S. Approaches for Fabricating High Efficiency Organic Light Emitting Diodes. *J. Mater. Chem. C*, **2015**, *3*, 2974-3002.
- (72) Mazzio, K. A.; Luscombe, C. K. The Future of Organic Photovoltaics. *Chem. Soc. Rev.*, **2015**, *44*, 78-90.
- (73) Lu, L.; Kelly, M. A.; You, W.; Yu, L. Status and Prospects for Ternary Organic Photovoltaics. *Nature Photonics* **2015**, *9*, 491-500.
- (74) Yao, H.; Ye, L.; Zhang, H.; Li, S.; Zhang, S.; Hou, J. Molecular Design of Benzodithiophene-Based Organic Photovoltaic Materials. *Chem. Rev.*, **2016**, *116*, 7397-7457.
- (75) Leng, C. Z.; Losego, M. D. Vapor Phase Infiltration (VPI) for Transforming Polymers into Organic-inorganic Hybrid Materials: Current Progress and Future Challenges. *Journal of Materials Horizons*, **2017**, *4*, 747-771.
- (76) Knez, M.; Nielsch, K.; Niinistö, L. Synthesis and Surface Engineering of Complex Nanostructures by Atomic Layer Deposition. *Adv. Mater.*, **2007**, *19*, 3425-3438.
- (77) George, S. M. Atomic Layer Deposition: An Overview. *Chem. Rev.*, **2010**, *110*, 111-131.
- (78) Suntola, T.; Antson, J. Method for producing compound thin films. Google Patents; 1977.

- (79) Suntola, T. Atomic Layer Epitaxy. *Mater. Sci. Rep.* **1989**, *4*, 261-312.
- (80) Leskelä, M.; Ritala, M. Atomic Layer Deposition Chemistry: Recent Developments and Future Challenges. *Angew. Chem. Int. Ed.*, **2003**, *42*, 5548-5554.
- (81) Zaera, F. The Surface Chemistry of Thin Film Atomic Layer Deposition (ALD) Processes for Electronic Device Manufacturing. *J. Mater. Chem.*, **2008**, *18*, 3521-3526.
- (82) Yoshimura, T.; Tatsuura, S.; Sotoyama, W. Polymer Films Formed with Monolayer Growth Steps by Molecular Layer Deposition. *Appl. Phys. Lett.* **1991**, *59*, 482-484.
- (83) George, S. M.; Yoon, B.; Dameron, A. A. Surface Chemistry for Molecular Layer Deposition of Organic and Hybrid Organic-Inorganic Polymers. *Acc. Chem. Res.*, **2009**, *42*, 498-508.
- (84) George, S. M.; Yoon, B.; Hall, R. A.; Abdulagatov, A. I.; Gibbs, Z. M.; Lee, Y.; Seghete, D.; Lee, B. H. in *Atomic Layer Deposition of Nanostructured Materials*, eds. N. Pinna and M. Knez, Wiley-VCH, **2011**, pp. 83-108.
- (85) Lee, S. M.; Pippel, E.; Knez, M. Metal Infiltration into Biomaterials by ALD and CVD: A Comparative Study. *ChemPhysChem*, **2011**, *12*, 791-798.
- (86) Puurunen, R. L. Surface Chemistry of Atomic Layer Deposition: A Case Study for the Trimethylaluminum/Water Process. *J. Appl. Phys.*, **2005**, *97*, 121301-121362.
- (87) Niinistö, L.; Nieminen, M.; Päiväsaari, J.; Niinistö, J.; Putkonen, M.; Nieminen, M. Advanced Electronic and Optoelectronic Materials by Atomic Layer Deposition: An Overview with Special Emphasis on Recent Progress in Processing of High-*k* Dielectrics and Other Oxide Materials. *Phys. Stat. Sol. (a)* **2004**, *201*, 1443-1452.
- (88) Gregorczyk, K.; Knez, M. Hybrid Nanomaterials through Molecular and Atomic Layer Deposition: Top down, Bottom up, and In-between Approaches to New Materials. *Progress in Materials Science*. **2016**, *75*, 1-37.
- (89) Aizenberg, J.; Tkachenko, A.; Weiner, S.; Addadi, L.; Hendler, G. Calcitic Microlenses as Part of the Photoreceptor System in Brittlestars. *Nature* **2001**, *412*, 819-822.
- (90) Addadi, L.; Weiner, S. Biomineralization: Crystals, Asymmetry and life. *Nature* **2001**, *411*, 753-755.
- (91) Kamat, S.; Su, X.; Ballarini, R.; Heuer, A. H. Structural Basis for the Fracture Toughness of the Shell of the Conch *Strombus Gigas*. *Nature* **2000**, *405*, 1036-1040.
- (92) Lowenstam, H. A.; Weiner, S. *On Biomineralization* (Oxford Univ. Press, New York, **1989**).
- (93) Lowenstam, H. A. Lepidocrocite, an Apatite Mineral, and Magnetite in Teeth of Chitons (Polyplacophora). *Science* **1967**, *156*, 1373-1375.
- (94) Waters, N. E. in *The Mechanical Properties of Biological Materials*, J. F. V. Vincent, J. D. Currey, Eds. (Cambridge Univ. Press, London), **1980**, *34*, 99-136.
- (95) Gibbs, P. E.; Bryan, G. W. Copper-the Major Metal Component of Glycerid Polychaete Jaws. *J. Mar. Biol. Assoc. UK* **1980**, *60*, 205-214.

- (96) Lichtenegger, H. C.; Schoberl, T.; Bartl, M. H.; Waite, H.; Stucky, G. D. High Abrasion Resistance with Sparse Mineralization: Copper Biomineral in Worm Jaws. *Science* **2002**, *298*, 389-392.
- (97) Lichtenegger, H. C.; Schöberl, T.; Ruokolainen, J. T.; Cross, J. O.; Heald, S. M.; Birkedal, H.; Waite, J. H.; Stucky, G. D. Zinc and Mechanical Prowess in the Jaws of Nereis, a Marine Worm. *Proceedings of the National Academy of Sciences, USA*. **2003**, *100*, 9144-9149.
- (98) Lee, S. M.; Pippel, E.; Gösele, U.; Dresbach, C.; Qin, Y.; Chandran, C. V.; Bräuniger, T.; Hause, G.; Knez, M. Greatly Increased Toughness of Infiltrated Spider Silk. *Science* **2009**, *324*, 488-491.
- (99) Gong, B.; Peng, Q.; Jur, J. S.; Devine, C. K.; Lee, K.; Parsons, G. N. Sequential Vapor Infiltration of Metal Oxides into Sacrificial Polyester Fibers: Shape Replication and Controlled Porosity of Microporous/Mesoporous Oxide Monoliths. *Chem. Mater.* **2011**, *23*, 3476-3485.
- (100) Peng, Q.; Tseng, Y. C.; Darling, S. B.; Elam, J. W. Nanoscopic Patterned Materials with Tunable Dimensions via Atomic Layer Deposition on Block Copolymers. *Adv. Mater.* **2010**, *22*, 5129-5133.
- (101) Peng, Q.; Tseng, Y. C.; Darling, S. B.; Elam, J. W. A Route to Nanoscopic Materials via Sequential Infiltration Synthesis on Block Copolymer Templates. *ACS Nano* **2011**, *5*, 4600-4606.
- (102) Lee, S. M.; Pippel, E.; Moutanabbir, O.; Kim, J. H.; Lee, H. J.; Knez, M. In Situ Raman Spectroscopic Study of Al-Infiltrated Spider Dragline Silk under Tensile Deformation. *ACS Appl. Mater. Interfaces*, **2014**, *6*, 16827-16834.
- (103) Du, N.; Liu, X. Y.; Narayanan, J.; Li, L.; Lim, M. L. M.; Li, D. Design of Superior Spider Silk: from Nanostructure to Mechanical Properties. *Biophys. J.* **2006**, *91*, 4528-4535.
- (104) Stauffer, S. L.; Coguill, S. L.; Lewis, R. V. Comparison of Physical Properties of Three Silks from *Nephila clavipes* and *Araneus Gemmoides*. *J. Arachnol.* **1994**, *22*, 5-11.
- (105) Sirichaisit, J.; Brookes, V. L.; Young, R. J.; Vollrath, F. Analysis of Structure/Property Relationships in Silkworm (*Bombyx mori*) and Sider Dragline (*Nephila edulis*) Silks Using Raman Spectroscopy. *Biomacromolecules* **2003**, *4*, 387-394.
- (106) Edwards, H. G. M.; Farwell, D. W. Raman Spectroscopic Studies of Silk. *J. Raman Spectrosc.* **1993**, *26*, 901-909.
- (107) Lee, S. M.; Pippel, E.; Moutanabbir, O.; Gunkel, I.; Thurn-Albrecht, T.; Knez, M. Improved Mechanical Stability of Dried Collagen Membrane after Metal Infiltration. *ACS Appl. Mater. Interfaces*, **2010**, *2*, 2436-2441.
- (108) Zhang, L.; Patil, Avinash J.; Li, L.; Schierhorn, A.; Mann, S.; Gösele, U.; Knez, M. Chemical Infiltration during Atomic Layer Deposition: Metalation of Porphyrins as Model Substrates. *Angewandte Chemie International Edition*, **2009**, *48*, 4982-4985.
- (109) Gregorczyk, K. E.; Pickup, D. F.; Sanz, M. G.; Irakulis, I. A.; Rogero, C.; Knez, M. Tuning the Tensile Strength of Cellulose through Vapor-Phase Metalation. *Chem. Mater.* **2015**, *27*, 181-188.

- (110) Lee, S. M.; Ischenko, V.; Pippel, E.; Masic, A.; Moutanabbir, O.; Fratzl, P.; Knez, M. An Alternative Route Towards Metal–Polymer Hybrid Materials Prepared by Vapor-Phase Processing. *Adv. Funct. Mater.*, **2011**, *21*, 3047–3055.
- (111) Manners, I. Putting Metals into Polymers. *Science* **2001**, *294*, 1664-1666.
- (112) Sanchez, C.; Julián, B.; Belleville, P.; Popall, M. Applications of Hybrid Organic–inorganic Nanocomposites. *J. Mater. Chem.* **2005**, *15*, 3559-3592.
- (113) Houbertz, R.; Domann, G.; Schulz, J.; Olsowski, B.; Fröhlich, L.; Kim, W. S. Impact of Photoinitiators on the Photopolymerization and the Optical Properties of Inorganic–organic Hybrid Polymers. *Appl. Phys. Lett.* **2004**, *84*, 1105-1107.
- (114) MacLachlan, M. J.; Ginzburg, M.; Coombs, N.; Coyle, T. W.; Raju, N. P.; Greendan, J. E.; Ozin, G. A.; Manners, I. Shaped Ceramics with Tunable Magnetic Properties from Metal-containing Polymers. *Science* **2000**, *287*, 1460-1463.
- (115) Lee, C. F.; Leigh, D. A.; Pritchard, R. G.; Schultz, D.; Teat, S. J.; Timco, G. A.; Winpenny, R. E. P. Hybrid Organic–inorganic Rotaxanes and Molecular Shuttles. *Nature* **2009**, *458*, 314-318.
- (116) Parsons, G. N.; Atanasov, S. E.; Dandley, E. C.; Devine, C. K.; Gong, B.; Jur, J. S.; Lee, K.; Oldham, C. J.; Peng, Q.; Spagnola, J. C. Mechanisms and Reactions during Atomic Layer Deposition on Polymers. *Coordination Chemistry Reviews* **2013**, *257*, 3323-3331.
- (117) Akyildiz, H. I.; Padbury, R. P.; Parsons, G. N.; Jur, J. S. Temperature and Exposure Dependence of Hybrid Organic–Inorganic Layer Formation by Sequential Vapor Infiltration into Polymer Fibers. *Langmuir*, **2012**, *28*, 15697-15704.
- (118) Myers, H. P. Introductory Solid State Physics. *Taylor & Francis*. **2002**, ISBN 0-7484-0660-3.
- (119) Smith, B. C. Fundamentals of Fourier Transform Infrared Spectroscopy, Second Edition, *CRC Press*. **2011**, ISBN 9781420069297 - CAT# 69292.
- (120) Gardiner, D. J. Practical Raman Spectroscopy. *Springer-Verlag*. **1989**, ISBN 978-0-387-50254-0.
- (121) Skoog, D. A.; Holler, F. J.; Crouch, S. R. Principles of Instrumental Analysis (6th ed.). *Belmont, CA: Thomson Brooks/Cole*. **2007**, pp. 169–173. ISBN 9780495012016.
- (122) Binnig, G.; Quate C. F.; Gerber, C. Atomic force microscope. *Phys. Rev. Lett.* **1986**, *56*, 930-933.
- (123) Givaja, G.; Amo-Ochoa, P., Gómez-García, C. J.; Zamora, F. Electrically Conductive Coordination Polymers. *Chem. Soc. Rev.*, **2012**, *41*, 115–147 115.
- (124) Schroder, D. K. Semiconductor Material and Device Characterization, 2nd Ed., (Wiley-Interscience, New York, **1998**).
- (125) ASTM Standard F84-93, “Standard method for measuring resistivity of silicon slices with a collinear four-point probe,” **1996**, Annual Book of ASTM Standards, Am. Soc. Test. Mat., West Conshohocken, PA.

- (126) Ed. G. Chen et al. Thin Film Thermoelectric Characterization Techniques. Chapter 3 of Annual Review of Heat Transfer. **2013**, *Begell House Inc., New York*.
- (127) Van der Pauw, L. J. A method of measuring the resistivity and Hall coefficient of lamellae of arbitrary shape. *Philips Res. Rep.* **1958**, *13*, 1-9.
- (128) Klauk, H. Klauk, Organic Thin-film Transistors. *Chem. Soc. Rev.* **2010**, *39*, 2643–2666.
- (129) Yang, Y.; Westerweele, E.; Zhang, C.; Smith, P.; Heeger, A. J. Enhanced Performance of Polymer Light-emitting Diodes using High-surface Area Polyaniline Network Electrodes. *J. Appl. Phys.* **1995**, *77*, 694–698.
- (130) Kim, J. Y.; Lee, K.; Coates, N. E.; Moses, D.; Nguyen, T.; Dante, M.; Heeger, A. J. Efficient Tandem Polymer Solar Cells Fabricated by All-solution Processing. *Science* **2007**, *317*, 222–225.
- (131) Song, H. K.; Palmore, G. T. R. Redox-Active Polypyrrole: Toward Polymer-Based Batteries. *Adv. Mater.* **2006**, *18*, 1764–1768.
- (132) Wu, Q.; Xu, Y.; Yao, Z.; Liu, A.; Shi, G. Supercapacitors Based on Flexible Graphene/Polyaniline Nanofiber Composite Films. *ACS Nano* **2010**, *4*, 1963–1970.
- (133) Pan, L. J.; Yu, G. H.; Zhai, D. Y.; Lee, H. R.; Zhao, W. T.; Liu, N.; Wang, H. L.; Tee, B. C. K.; Shi, Y.; Cui, Y.; Bao, Z. N. Hierarchical Nanostructured Conducting Polymer Hydrogel with High Electrochemical Activity. *Proc. Natl. Acad. Sci. USA.* **2012**, *109*, 9287–9292.
- (134) Lee, S. H.; Lee, D. H.; Lee, K.; Lee, C. W. High-Performance Polyaniline Prepared via Polymerization in a Self-Stabilized Dispersion. *Adv. Funct. Mater.* **2005**, *15*, 1495–1500.
- (135) Huang, J. X.; Kaner, R. B. Nanofiber Formation in the Chemical Polymerization of Aniline: A Mechanistic Study. *Angew. Chem. Int. Ed.* **2004**, *43*, 5817–5821.
- (136) Das, D.; Datta, A.; Contractor, A. Q. Doping of Polyaniline with 6-Cyano-2-naphthol. *J. Phys. Chem. B* **2014**, *118*, 12993–13001.
- (137) Stejskal, J.; Sapurina, I.; Trchova, M.; Prokes, J. Protonation of Polyaniline with 3-Nitro-1,2,4-triazol-5-one. *Chem. Mater.* **2002**, *14*, 3602–3606.
- (138) Ryu, K. S.; Moon, B. W.; Joo, J.; Chang, S. H. Characterization of Highly Conducting Lithium Salt Doped Polyaniline Films Prepared from Polymer Solution. *Polymer.* **2001**, *42*, 9355–9360.
- (139) Chen, S. A.; Lin, L. C. Polyaniline Doped by the New Class of Dopant, Ionic Salt: Structure and Properties. *Macromolecules* **1995**, *28*, 1239–1245.
- (140) Bajer, I. K.; Pron, A.; Abramowicz, J.; Jeandey, C.; Oddou, J. L.; Sobczak, J. W. Lewis Acid Doped Polyaniline: Preparation and Spectroscopic Characterization. *Chem. Mater.* **1999**, *11*, 552–556.
- (141) Chaudhuri, D.; Kumar, A.; Rudra, I.; Sarma, D. D. Synthesis and Spectroscopic Characterization of Highly Conducting BF₃-Doped Polyaniline. *Adv. Mater.* **2001**, *13*, 1548–1551.

- (142) Dimitriev, O. P. Doping of Polyaniline by Transition-Metal Salts. *Macromolecules* **2004**, *37*, 3388–3395.
- (143) Izumi, C. M. S.; Ferreira, A. M. D. C.; Constantino, V. R. L.; Temperini, M. L. A. Studies on the Interaction of Emeraldine Base Polyaniline with Cu(II), Fe(III), and Zn(II) Ions in Solutions and Films. *Macromolecules* **2007**, *40*, 3204–3212.
- (144) Salaneck, W.R.; Liedberg, B.; Inganäs, O.; Erlandsson, R.; Lundström, I.; MacDiarmid, A.G.; Halpern, M.; Somasiri, N.L.D. Physical Characterization of Some Polyaniline, (øN)_x. *Mol. Cryst. Liq. Cryst.* **1985**, *121*, 191–194.
- (145) Kim, Y. H.; Foster, C.; Chiang, J.; Heeger, A. J. Photoinduced Localized Charged Excitations in Polyaniline. *Synth. Met.* **1988**, *26*, 49–59.
- (146) Fukuda, T.; Takezoe, H.; Ishikawa, K.; Fukuda, A.; Woo, H. S.; Jeong, S. K.; Oh, E. J.; Suh, J. S. Ir and Raman Studies in Three Polyanilines with Different Oxidation Level. *Synth. Met.* **1995**, *69*, 175–176.
- (147) Pereira da Silva, J. E.; Cordoba de Torresi, S. I.; De Faria, D. L. A.; Temperini, M. L. A. Raman Characterization of Polyaniline Induced Conformational Changes. *Synth. Met.* **1999**, *101*, 834–835.
- (148) Louarn, G.; Lapskowski, M.; Quillard, S.; Pron, A.; Buisson, J. P.; Lefrant, S. Vibrational Properties of Polyaniline-Isotope Effects. *J. Phys. Chem.* **1996**, *100*, 6998–7006.
- (149) Genoud, F.; Bajer, I. K.; Bedel, A.; Oddou, J. L.; Jeandey, C.; Pron, A. Lewis Acid Doped Polyaniline. Part II: Spectroscopic Studies of Emeraldine Base and Emeraldine Hydrochloride Complexation with FeCl₃. *Chem. Mater.* **2000**, *12*, 744–749.
- (150) Forrest, S. R. The Path to Ubiquitous and Low-cost Organic Electronic Appliances on Plastic. *Nature* **2004**, *428*, 911–918.
- (151) Facchetti, A. π -Conjugated Polymers for Organic Electronics and Photovoltaic Cell Applications. *Chem. Mater.* **2011**, *23*, 733–758.
- (152) Siringhaus, H.; Tessler, N.; Friend, R. H. Integrated Optoelectronic Devices Based on Conjugated Polymers. *Science* **1998**, *280*, 1741–1744.
- (153) Singh, V.; Bougher, T. L.; Weathers, A.; Cai, Y.; Bi, K.; Pettes, M. T.; McMenamin, S. A.; Lv, W.; Resler, D. P.; Gattuso, T. R.; Altman, D. H.; Sandhage, K. H.; Shi, L.; Henry, A.; Cola, B. A. High Thermal Conductivity of Chain-oriented Amorphous Polythiophene. *Nature Nanotech.* **2014**, *9*, 384–390.
- (154) Lee, J. H.; Kim, J. J. Interfacial Doping for Efficient Charge Injection in Organic Semiconductors. *Physica Status Solidi (a)* **2012**, *209*, 1399–1413.
- (155) Pfeiffer, M.; Leo, K.; Zhou, X.; Huang, J. S.; Hofmann, M.; Werner, A.; Blochwitz-Nimoth, J. Doped Organic Semiconductors: Physics and Application in Light Emitting Diodes. *Organic Electronics* **2003**, *4*, 89–103.
- (156) Gross, M.; Müller, D. C.; Nothofer, H. G.; Scherf, U.; Neher, D.; Bräuchle, C.; Meerhol, K. Improving the Performance of Doped π -conjugated Polymers for Use in Organic Light-emitting Diodes. *Nature* **2000**, *405*, 661–665.

- (157) Li, Y. F. Molecular Design of Photovoltaic Materials for Polymer Solar Cells: Toward Suitable Electronic Energy Levels and Broad Absorption. *Acc. Chem. Res.* **2012**, *45*, 723-733.
- (158) Park, S. H.; Roy, A.; Beaupre', S.; Cho, S.; Coates, N.; Moon, J. S.; Moses, D.; Leclerc, M.; Lee, K.; Heeger, A. J. Bulk Heterojunction Solar Cells with Internal Quantum Efficiency Approaching 100%. *Nature photon.* **2009**, *3*, 297-302.
- (159) Peet, J.; Kim, J. Y.; Coates, N. E.; Ma, W. L.; Moses, D.; Heeger, A. J.; Bazan, G. C. Efficiency enhancement in low-bandgap polymer solar cells by processing with alkane dithiols. *Nature Mater.* **2007**, *6*, 497-500.
- (160) He, Z. C.; Xiao, B.; Liu, F.; Wu, H. B.; Yang, Y. L.; Xiao, S.; Wang, C.; Russell, T. P.; Cao, Y. Single-junction polymer solar cells with high efficiency and photovoltage. *Nature photon.* **2015**, *9*, 174-179.
- (161) Nam, S.; Seo, J.; Han, H.; Kim, H.; Hahm, S. G.; Ree, M.; Gal, Y. S.; Anthopoulos, T. D.; Bradley, D. D. C.; Kim, Y. >10% Efficiency Polymer: Fullerene Solar Cells with Polyacetylene-Based Polyelectrolyte Interlayers. *Adv. Mater. Interfaces* **2016**, 1600415.
- (162) Li, G.; Zhu, R.; Yang, Y. Polymer Solar Cells. *Nature photon.* **2012**, *6*, 153-161.
- (163) Wei, P.; Menke, T.; Naab, B. D.; Leo, K.; Riede, M.; Bao, Z. N. 2-(2-Methoxyphenyl)-1,3-dimethyl-1*H*-benzimidazol-3-ium Iodide as a New Air-Stable n-Type Dopant for Vacuum-Processed Organic Semiconductor Thin Films. *J. Am. Chem. Soc.* **2012**, *134*, 3999-4002.
- (164) Calhoun, M. F.; Sanchez, J.; Olaya, D.; Gershenson, M. E.; Podzorov, V. Electronic Functionalization of the Surface of Organic Semiconductors with Self-assembled Monolayers. *Nature Mater.* **2008**, *7*, 84-89.
- (165) Mendez, H.; Heimel, G.; Winkler, S.; Frisch, J.; Opitz, A.; Sauer, K.; Wegner, B.; Oehzelt, M.; Rothel, C.; Duhm, S.; Tobbens, D.; Koch, N.; Salzmann, I. Charge-transfer Crystallites as Molecular Electrical Dopants. *Nat Commun.* **2015**, *6*: 8560.
- (166) Gao, C. H.; Zhu, X. Z.; Zhang, L.; Zhou, D. Y.; Wang, Z. K.; Liao, L. S. Comparative Studies on the Inorganic and Organic P-type Dopants in Organic Light-emitting Diodes with Enhanced Hole Injection. *Appl. Phys. Lett.* **2013**, *102*, 153301.
- (167) Chang, C. C.; Hsieh, M. T.; Chen, J. F.; Hwang, S. W.; Chen, C. H. Highly Power Efficient Organic Light Emitting Diodes with a *p*-doping Layer. *Appl. Phys. Lett.* **2006**, *89*, 253504.
- (168) Duong, D. T.; Wang, C. C.; Antono, E.; Toney, M. F.; Salleo, A. The Chemical and Structural Origin of Efficient P-type Doping in P3HT. *Organic Electronics* **2013**, *14*, 1330-1336.
- (169) Duong, D. T.; Phan, H.; Hanifi, D.; Jo, P. S.; Nguyen, T. Q.; Salleo, A. Direct Observation of Doping Sites in Temperature Controlled, *p*-Doped P3HT Thin Films by Conducting Atomic Force Microscopy. *Adv. Mater.* **2014**, *26*, 6069-6073.
- (170) Yang, J.; Li, Y.; Duhm, S.; Tang, J.; Kera, S.; Ueno, N. Molecular Structure-Dependent Charge Injection and Doping Efficiencies of Organic Semiconductors: Impact of Side Chain Substitution. *Adv. Mater. Interfaces* **2014**, *1*, 1300128.

- (171) Tietze, M. L.; Burtone, L.; Riede, M.; Lüssem, B.; Leo, K. Fermi Level Shift and Doping Efficiency in P-doping Small Molecule Organic Semiconductors: A Photoelectron Spectroscopy and Theoretical Study. *Phys. Rev. B* **2012**, *86*, 035320.
- (172) Cho, S. H.; Pyo, S. W.; Suh, M. C. Low Voltage Top-emitting Organic Light Emitting Devices By Using 1,4,5,8,9,11-hexaazatriphenylene-hexacarbonitrile. *Synthetic Metals* **2012**, *162*, 402-405.
- (173) Aziz, E. F.; Vollmer, A.; Eisebitt, S.; Eberhardt, W.; Pingel, P.; Neher, D.; Koch, N. Localized Charge Transfer in a Molecularly Doped Conducting Polymer. *Adv. Mater.* **2007**, *19*, 3257-3260.
- (174) Pingel, P.; Arvind, M.; Kölln, L.; Steyrlleuthner, R.; Kraffert, F.; Behrends, J.; Janietz, S.; Neher, D. P-Type Doping of Poly(3-hexylthiophene) with the Strong Lewis Acid Tris(pentafluorophenyl)-borane. *Adv. Electron. Mater.* **2016**, 1600204.
- (175) Welch, G. C.; Bazan, G. C. Lewis Acid Adducts of Narrow Band Gap Conjugated Polymers. *J. Am. Chem. Soc.* **2011**, *133*, 4632-4644.
- (176) Welch, G. C.; Coffin, R.; Peet, J.; Bazan, G. C. Band Gap Control in Conjugated Oligomers via Lewis Acids. *J. Am. Chem. Soc.* **2009**, *131*, 10802-10803.
- (177) Zalar, P.; Henson, Z. B.; Welch, G. C.; Bazan, G. C.; Nguyen, T. Q. Color Tuning in Polymer Light-Emitting Diodes with Lewis Acids. *Angew. Chem., Int. Ed.* **2012**, *51*, 7495-7498.
- (178) Zalar, P.; Kuik, M.; Henson, Z. B.; Woellner, C.; Zhang, Y.; Sharenko, A.; Bazan, G. C.; Nguyen, T. Q. Increased Mobility Induced by Addition of a Lewis Acid to a Lewis Basic Conjugated Polymer. *Adv. Mater.* **2014**, *26*, 724-727.
- (179) Yim, K. H.; Whiting, G. L.; Murphy, C. E.; Halls, J. J. M.; Burroughes, J. H.; Friend, R. H.; Kim, J. S. Controlling Electrical Properties of Conjugated Polymers via a Solution Based p-Type Doping. *Adv. Mater.* **2008**, *20*, 3319-3324.
- (180) Cui, J.; Tong, D. E. M.; Sanz, A.; Ezquerra, T. A.; Rebollar, E.; Nogales, A. Relaxation and Conductivity in P3HT/PC₇₁BM Blends As Revealed by Dielectric Spectroscopy. *Macromolecules* **2016**, *49*, 2709-2717.
- (181) Kao, C. Y.; Lee, B.; Wielunski, L. S.; Heeney, M.; McCulloch, I.; Garfunkel, E.; Feldman, L. C.; Podzorov, V. Doping of Conjugated polythiophenes with Alkyl Silanes. *Adv. Funct. Mater.* **2009**, *19*, 1906-1911.
- (182) Tsoi, W. C.; James, D. T.; Kim, J. S.; Nicholson, P. G.; Murphy, C. E.; Bradley, D. D. C.; Nelson, J.; Kim, J. S. The Nature of In-Plane Skeleton Raman Modes of P3HT and Their Correlation to the Degree of Molecular Order in P3HT: PCBM Blend Thin Films. *J. Am. Chem. Soc.* **2011**, *133*, 9834-9843.
- (183) Yamamoto, J.; Furukawa, Y. Electronic and Vibrational Spectra of Positive Polarons and Bipolarons in Regioregular Poly (3-hexylthiophene) Doped with Ferric Chloride. *J. Phys. Chem. B* **2015**, *119*, 4788-4794.
- (184) Park, Y. D.; Cho, J. H.; Kim, D. H.; Lee, W. H.; Cho, K. Energy-Level Alignment at Interfaces between Gold and Poly (3-hexylthiophene) Films with two Different Molecular Structures. *AIP Conf. Proc.* **2007**, *879*, 1623-1625.

- (185) Patel, S. N.; Glauddell, A. M.; Kiefer, D.; Chabinye, M. L. Increasing the Thermoelectric Power Factor of a Semiconducting Polymer by Doping from the Vapor Phase. *ACS Macro Lett.* **2016**, *5*, 268-272.
- (186) Noriega, R.; Rivnay, J.; Vandewal, K.; Koch, F. P. V.; Stingelin, N.; Smith, P.; Toney, M. F.; Salleo, A. A General Relationship between Disorder, Aggregation and Charge Transport in Conjugated Polymers. *Nature Mater.* **2013**, *12*, 1038-1044.
- (187) Jacobs, I. E.; Aasen, E. W.; Oliveira, J. L.; Fonseca, T. N.; Roehling, J. D.; Li, J.; Zhang, G.; Augustine, M. P.; Mascari, M.; Moulé, A. J. Comparison of Solution-mixed and Sequentially Processed P3HT: F4TCNQ Films: Effect of Doping-induced Aggregation on Film Morphology. *J. Mater. Chem. C*, **2016**, *4*, 3454-3466.
- (188) Wu, C. G.; Bein, T. Conducting Polyaniline Filaments in a Mesoporous Channel Host. *Science* **1994**, *264*, 1757-1759.
- (189) Lee, K.; Cho, S.; Park, S. H.; Heeger, A. J.; Lee, C. W.; Lee, S. H. Metallic Transport in Polyaniline. *Nature* **2006**, *441*, 65-68.
- (190) Matnishyan, A. A. Synthesis and Study of Polyaniline Nanocomposites with Metal Oxides. *Phys. Solid State* **2011**, *53*, 1727-1731.
- (191) Bairi, V. G.; Warford, B. A.; Bourdo, S. E.; Biris, A. S.; Viswanathan, T. Synthesis and Characterization of Tanninsulfonic Acid Doped Polyaniline–Metal Oxide Nanocomposites. *J. Appl. Polym. Sci.* **2012**, *124*, 3320-3328.
- (192) Mostafaei, A.; Zolriasatein, A. Synthesis and Characterization of Conducting Polyaniline Nanocomposites Containing ZnO Nanorods. *Progress in Natural Science: Materials International* **2012**, *22*, 273-280.
- (193) Mostafaei, A.; Nasirpour, F. Electrochemical Study of Epoxy Coating Containing Novel Conducting Nanocomposite Comprising Polyaniline–ZnO Nanorods on Low Carbon Steel. *Corrosion Engineering, Science and Technology* **2013**, *48*, 513-524.
- (194) Singla, M. L.; Awasthi, S.; Srivastava, A.; Jain, D. V. S. Effect of Doping of Organic and Inorganic Acids on Polyaniline/Mn₃O₄ Composite for NTC and Conductivity Behavior. *Sens. Actuators A*, **2007**, *136*, 604-612.
- (195) Jur, J. S.; Parsons, G. N. Atomic Layer Deposition of Conductive Coatings on Cotton, Paper, and Synthetic Fibers: Conductivity Analysis and Functional Chemical Sensing Using “All-Fiber” Capacitors. *Adv. Funct. Mater.* **2011**, *21*, 1993-2002.
- (196) Sinha, S.; Sarkar, S. K. Atomic Layer Deposition of Textured Zinc Nitride Thin Films. *RSC Adv.*, **2014**, *4*, 47177-47183.
- (197) Michael, R. J. V.; Sambandam, B.; Muthukumar, T.; Umopathy, M. J.; Manoharan, P. T. Spectroscopic Dimensions of Silver Nanoparticles and Clusters in ZnO Matrix and Their Role in Bioinspired Antifouling and Photocatalysis. *Phys. Chem. Chem. Phys.*, **2014**, *16*, 8541-8555.
- (198) Shin, W. H.; Hwang, T. H.; Huh, Y. S.; Choi, J. W. Electrochemically Controlled Nanopore and Crystal Structure Evolution in Zinc Oxide Nanorods. *J. Electrochem. Soc.*, **2012**, *159*, A2143-A2147.

- (199) Alvi, F.; Ram, M. K.; Gomez, H.; Joshi, R. K.; Kumar, A. Evaluating the Chemio-Physio Properties of Novel Zinc Oxide–Polyaniline Nanocomposite Polymer Films. *Polym. J.* **2010**, *42*, 935-940.
- (200) Kim, S. J. A Surface Chemical Reaction in Organic–Inorganic Materials Using a New Chemical Evaporation System. *Chem. Mater.* **2015**, *27*, 4546-4551.
- (201) Reed, R. A. Resonance Raman Characterization of the Radical Anion and Triplet States of Zinc Tetraphenylporphine. *J. Phys. Chem.* **1991**, *95*, 9720-9727.
- (202) Louarn, G.; Lapskowski, M.; Quillard, S.; Pron, A.; Buisson, J. P.; Lefrant, S. Vibrational Properties of Polyanilines Isotope Effects. *J. Phys. Chem.* **1996**, *100*, 6998-7006.
- (203) Socrates, G. *Infrared and Raman Characteristic Group Frequencies: Tables and Charts*; West Sussex: John Wiley & Sons, **2007**.
- (204) Hsu, C. H. Effect of the Cu Source on Optical Properties of CuZnO Films Deposited by Ultrasonic Spraying. *Materials* **2014**, *7*, 1261-1270.
- (205) Kaschner, A.; Haboeck, U.; Strassburg, M.; Strassburg, M.; Kaczmarczyk, G.; Hoffmann, A.; Thomsen, C. Nitrogen-related local vibrational modes in ZnO:N. *Appl. Phys. Lett.* **2002**, *80*, 1909-1911.
- (206) Artamonov, V. V.; Klyui, N. I.; Melnik, V. P.; Romanyuk, B. N.; Valakh, M. Ya.; Vasilik, O.; Semenovich, V. A.; Pérez-Rodríguez, A.; Morante, J. R. *Carbon* **1998**, *36*, 791-794.
- (207) Pouget, J. P. X-ray Structure of Polyaniline. *Macromolecules* **1991**, *24*, 779-789.
- (208) Verma, N. K. Effect of Zinc Oxide Nano Particle Concentration in the Polyaniline-Zinc Oxide Nanocomposite on the Dielectric Property. *Material science research India* **2014**, *11*, 146-152.
- (209) Mahat, M. M. Elucidating the Deprotonation of Polyaniline Films by X-ray Photoelectron Spectroscopy. *J. Mater. Chem. C*, **2015**, *3*, 7180-7186.
- (210) Sakamoto, R.; Hoshiko, K.; Liu, Q.; Yagi, T.; Nagayama, T.; Kusaka, S.; Tsuchiya, M.; Kitagawa, Y.; Wong, W.Y.; Nishihara, H. A Photofunctional Bottom-up Bis(dipyrrinato)zinc(II) Complex Nanosheet. *Nat. Commun.* **2015**, *6*, 6713.
- (211) Lee, E.; Benayad, A. Nanocrystalline ZnON; High Mobility and Low Band Gap Semiconductor Material for High Performance Switch Transistor and Image Sensor Application. *Scientific Reports* **2014**, *4*, 4948.
- (212) Xia, Y. N.; Wiesinger, J. M.; MacDiarmid, A. G. Camphorsulfonic Acid Fully Doped Polyaniline Emeraldine Salt: Conformations in Different Solvents Studied by an Ultraviolet/Visible/Near-Infrared Spectroscopic Method. *Chem. Mater.* **1995**, *7*, 443-445.

List of Publications

1. **Weike Wang**, Fan Yang, Chaoqiu Chen, Lianbing Zhang, Yong Qin, and Mato Knez, Tuning the Conductivity of Polyaniline through Doping by Means of Single Precursor Vapor Phase Infiltration. *Advanced Materials Interfaces*. 2017, 4, 201600806. (Chapter 3)

2. **Weike Wang**, Chaoqiu Chen, Christopher Tollan, Fan Yang, Yong Qin, and Mato Knez, Efficient and Controllable Vapor to Solid Doping of the Polythiophene P3HT by Low Temperature Vapor Phase Infiltration. *Journal of Materials Chemistry C*. 2017, 5, 2686-2694. (Chapter 4)

3. **Weike Wang**, Chaoqiu Chen, Christopher Tollan, Fan Yang, Mikel Beltrán, Yong Qin, and Mato Knez, Conductive Polymer-Inorganic Hybrid Materials through Synergistic Mutual Doping of the Constituents. *ACS Applied Materials & Interfaces*, 2017, 9, 27964-27971. (Chapter 5)

4. Fan Yang, Mikel Abadia, Chaoqiu Chen, **Weike Wang**, Le Li, Lianbing Zhang, Celia Rogero, Andrey Chuvilin, and Mato Knez, Design of Active and Stable Oxygen Reduction Reaction Catalysts by Embedding Co_xO_y Nanoparticles into Nitrogen-Doped Carbon, *Nano Research*. 2017, 10, 97-107.

Acknowledgements

I have too many people to whom I want to express my deep gratitude. First of all, I would like to thank my supervisor Prof. Dr. Mato Knez, for offering me the PhD position at CIC nanoGUNE. Prof. Mato Knez has always been supportive and open to all of my experiments during my three years PhD period. He usually gave me some useful advices whenever I could not handle the problems that occurred during my experiments. Let me express my deepest gratitude to Prof. Mato Knez again for his encouragement, confidence and support.

I am very grateful to Prof. Yong Qin at the Institute of Coal Chemistry, Chinese Academy of Sciences, who taught me a lot about Atomic Layer Deposition (ALD) before I came to Spain to start my PhD. During the two months of my secondment in China, he showed me how to prepare simple catalysts by ALD. Thanks to Prof. Yong Qin again for his help.

I also thank my colleague and roommate Dr. Chaoqiu Chen, who has been helping me a lot in both my life and research problems during the first two and a half years of my PhD. He gave me considerable advice and encouragement when I faced some problems during my experiments and my research paper writing process. Without his help, my experiments would not have been as successful.

I want to thank my further colleague Dr. Fan Yang. When I started to prepare my visa for Spain, he shared with me his experience. When I started my PhD project, I always bothered him a lot with my ALD-programming, the IR, the SEM set-ups and many other things.

I also want to thank our technician Mikel Beltán, who always helped me with the XRD set-up, the pump problems, etc. He trained me how to use the ALD equipment and the CVD tube in our lab. With his help, I successfully assembled my first ALD equipment. I also thank my colleague Dr. Ana Zuzuarregui, Unai Carmona, and Itxasne Azpitarte for their help in my daily life. Many thanks to all other group members: Dr. Lianbing Zhang, Dr. Le Li, Dr. Nagore Ibarra, Dr. Jaime DuMont, Sarai Garcia, Dr. Ana Beloqui, Dr. Keith Gregorczyk for the interesting and helpful discussions about science and life in the group.

Many thanks to Dr. Christopher Tollan in the Electron-Microscopy group for his great help in analyzing my samples with the electron microscope. Thanks also to all other colleagues at CIC nanoGUNE: Dr. Aitziber Eleta for her support in AFM microscopy, Dr. Andrey Chuvilin for his support with the TEM characterization, Dr. Wiwat Nuansing and David Arias for their help in Raman spectroscopy.

I also thank Dr. Celia Rogero, Dr. Jens Brede and Mikel Abadia from the Centro de Física de Materials in Donostia in Spain, for their great support with the XPS characterization.

Many thanks to all the Chinese friends here: Dr Fan Yang, Dr Chaoqiu Chen, Dr. Wenjing Yan, Dr. Xiangnan Sun, Dr. Lianbing Zhang, Dr. Le Li, Dr. Peining Li, Dr. Jingcheng Li, Jian Li, Dr. Shu Chen. Thank you very much for your help and company, and I enjoyed the time we have spent together.

Last but most importantly, I want to express my deepest gratitude to my parents, my brother, and my nephew. Without your love and encouragement during the three years, I could never have made it here. Thanks a lot for your company all the way.

Thanks a lot for the funding from the European Union FP7 Programme under the grant agreement number 607232 (Marie Curie-ITN THINFACE), and the Spanish Ministry of Economy and Competitiveness (MINECO) within grant agreement no. MAT2016-77393-R. The thesis was performed with the PCAM European doctorate.